SCANNING TUNNELING MICROSCOPY AND SPECTROSCOPY OF MOLYBDENUM DISULFIDE

Thesis by

John Adam Kramar

In Partial Fulfillment of the Requirements

for the Degree of

Doctor of Philosophy

California Institute of Technology

Pasadena, California

1990

(Submitted November 28, 1989)

Acknowledgements

This work could not have been done without the help and support of many people. My advisor, John Baldeschwieler, deserves the first thanks for pointing me in the direction of a truly interesting project and for encouragement, guidance and support along the way. Special thanks also go to Michael Weimer with whom I worked very closely during much of my graduate career. I really learned a lot from him about the nuts and bolts of research and about our projects in particular.

The entire JDB group both present and past have been friends and in many cases, scientific collaborators. Chunli Bai was involved in the early stages of the work on MoS_2 and in the last stages of debugging the STM. He also contributed a lot to the software development. Terry Coley was an invaluable source of information about the theoretical aspects of tunneling with special application to MoS_2. Much of what I understand about this subject is from discussions I had with him. Robert Driscoll was involved in some of the experimental work, notably developing our tip making procedures and taking some of the data. Shenda Baker also spent long hours taking scans of MoS_2, as well as plotting the *I-V* data in different ways and using curve fitting programs to try to figure out what was going on. Paul West was the person who actually started the STM project in the JDB group. He was also a constant encouragement to me with his optimistic, straight-forward suggestions to write-up and get out.

The most special thanks go to my wonderful and beautiful wife, Connie Jean, for her patience, love, and encouragement. We had some fun times as well as some rough times during my stay at Caltech, and I think we have both grown a lot. Thank you for your patience through the long hours spent at work on this project. Thank you for trying to understand my frustrations. Thank you for your encouragement and your faith in me. Thank you for your prayers. Thank you for Colleen Jeanette.

Abstract

Scanning tunneling microscopy (STM) is a recently developed surface analysis technique that is capable of atomic resolution imaging in real space. In STM, a sharp electrically conducting tip is brought near the sample and a tunneling current is established between the two. For topographical imaging, the tip is then raster-scanned over the surface while a feedback control system maintains constant current by adjusting the position of the tip in the surface normal. The trajectory that the tip follows is displayed as the surface topography. The unique geometry of the STM has also allowed the electronic nature of surfaces to be probed with unprecedented spatial resolution. This can be implemented, for example, by posing the probe tip over a specific surface location and examining the current-versus-voltage characteristics.

Careful consideration must be given in the design of an STM system. The crucial elements of vibration isolation and microscope rigidity must be optimized within the constraints of allowing coarse positioning of the tip and sample and permitting high-resolution scanning. A stable feedback control system must also be designed with flexibility to allow for different operating conditions.

We have built an ultrahigh vacuum (UHV) STM that is similar to the familiar pocket STM design. The UHV system includes a separate sample preparation chamber and vacuum-transfer load lock to facilitate in studies of clean, carefully prepared surfaces. The instrument is interfaced with a microprocessor for control of scanning, data acquisition, and coarse tip-sample approach and positioning. A high-resolution graphics monitor is also included for displaying the topographic images and the current-voltage spectra during acquisition and for reviewing previously stored images.

Studies of the basal cleavage plane of MoS_2 have been performed with this instrument. Large area images up to 360×360 nm reveal a high degree of variability in surface morphology, ranging from atomically smooth planes, to islands or mounds

ranging from 1 to 10 nm in diameter, to areas of complete surface roughness. Many unusual imaging phenomena were also observed in these scans, including bias-dependent images and surface modifications that were due to tip-sample interactions.

Atomic-resolution images revealing the trigonal symmetry of the surface plane were obtained in both the constant-current and current-imaging modes on the smooth areas of the surface. Two distinct sites can be seen, corresponding to the known molybdenum and sulfur atomic positions.

A simple description of the distance dependence of tunneling between the STM tip and an ideal semiconductor surface (no surface Fermi level pinning) is presented, based on conventional metal-insulator-semiconductor (MIS) theories. The current conduction mechanism involves thermionic emission over the semiconductor diffusion-potential barrier, which is a decreasing function of the tip-sample separation, followed by tunneling through the vacuum gap. The competition between the decreased vacuum-tunneling probability and the increased carrier population at the semiconductor surface for increasing separation gives rise to a predicted peak in the *I-s* curves at small separations, and a lowering of the apparent tunneling barrier height out to separations of more than 1 nm. The normally rectified current-voltage characteristics are also found to be a function of the tip-sample spacing, showing a weakening and then a reversal of rectification as the separation is increased. These predicted effects are substantiated by means of a detailed numerical calculation for the passivated *n*-type Si (111) surface.

The current-voltage spectroscopy of MoS_2, which is expected to behave as an ideal semiconductor, was examined. The surface-averaged spectra show a high degree of variability, with different data sets showing rectification in opposite polarities for the same physical tip and sample. The results are shown to be qualitatively different from known mechanisms for rectification in STM, including tip-curvature-induced field-gradient effects and effects that are due to the separation dependence of rectification in

ideal MIS structures. The results are best explained as doping inhomogeneities in our mineralogical samples.

TABLE OF CONTENTS

Chapter 2 (continued)

Chapter 3 (continued)

Chapter 1

INTRODUCTION

Introduction

Scanning tunneling microscopy (STM) is a recently introduced technique for surface analysis that has proved very powerful for elucidating surface topographies and for examining local electronic properties. Imaging with atomic-scale resolution has been demonstrated for topographical features, as well as for differences in electronic state distributions of filled and empty states. A wide variety of samples are amenable to imaging in environments ranging from ultrahigh vacuum to air and ionic solutions.[1]

The STM technique is based not on lenses and magnification in the conventional sense, but on a proximal "tactile" sensor. Its fore runner in this respect is the stylus profilometer, which measures surface topographies on a cruder scale by mapping out the trajectory of a tip as it is dragged across a surface at fixed loading force. In 1972, a major improvement was made in the capabilities for stylus imaging by Young *et al.*,[2] with the invention of the topographiner. This instrument worked on a similar principle, except that the surface was detected by means of a field-emission current from a sharp, conducting tip. This first non-contacting, non–surface-destructive, stylus-imaging method was able to resolve 400 nm features. Although Young *et al.* were able to demonstrate vacuum tunneling with the topographiner, it was left to Binnig *et al.*[3] some 10 years later to develop an instrument with improved vibrational stability, which used tunneling as the surface sensor. Their instrument, which they aptly named the scanning tunneling microscope, was soon shown to be capable of resolving individual surface atoms.[4]

Principle of Operation

The STM technique is based on the principle of quantum mechanical tunneling. When two conductors are brought within a few atomic diameters of each other, the wave nature of the electrons in the conductors permits them to penetrate the classically-forbidden, insulating barrier and to tunnel from one energetically-allowed region to the

other.[5] The tunneling current so induced is very sensitive to the nature of the barrier. For a one-dimensional, square barrier of height ϕ and width s, the tunneling current I is proportional to $\exp[-A\phi^{1/2}s]$, where A is a collection of fundamental constants equal to $10.2\ \mathrm{eV}^{-1/2}\mathrm{nm}^{-1}$. Barrier heights for metal-vacuum-metal tunneling are given by the electron work function, which for typical metals is around 5 eV. This means that a factor-of-ten change in the current is expected for every 0.1 nm change in s. It is this exquisite sensitivity of the tunneling current on the separation that makes atomic-resolution STM possible.

In STM, a sharp metal tip is brought within tunneling distance of an electrically conducting sample. A small bias voltage is applied between the two, and the tunnel current is measured. Because of the exponential dependence of the tunneling on the separation, only the portion of the tip closest to the surface on a 0.1 nm scale has any significant contribution to the current. In the extreme, the tunneling current can be due to one atom on the tip. This is what gives rise to the high lateral resolution of the STM. In the topographic-imaging mode, an electronic feedback mechanism is employed to maintain a constant current while the tip is raster-scanned across the surface. The trajectory that the tip must follow to maintain this constant tunneling resistance as it moves across the surface is the measured surface topography.

The exponential proportionality factor for the separation dependence of the tunneling current is the square root of the barrier height. If the tunneling barrier height (or equivalently the inverse decay length of the surface wave function) changes as a function of position over the surface, this will be convoluted into the measured topography. The barrier-height dependence can be quite simply extracted by modulation of the tip-surface separation with lock-in detection of the logarithm of the current. This provides a means of probing an additional degree of freedom that is related to the chemical identity and

bonding of the specific surface site. A good example of atomically-resolved, barrier-height imaging is found in the work of Villarrubia and Boland.[6]

A useful theory of STM imaging that is based on Bardeen's[7] transfer Hamiltonian formalism has been presented by Tersoff and Hamann.[8] In its simplest form, this theory predicts that a spherically symmetric tip will follow the contours of constant state density of the sample at the center of curvature of the tip. We see then that the STM does not image the topography of the surface in a traditional sense, but rather the topography of the sample's electronic state density at some distance from the surface, within an energy window defined by the tunneling bias voltage. The clearest evidence of this phenomenon is seen in the STM of certain semiconductor surfaces where major differences exist in the spatial distribution of the surface state densities for the conduction band and the valence band. This can give rise to pronounced differences in the measured surface topographies on alternating the sign of the tunneling bias voltage. A prime example of this is the work of Feenstra *et al.*[9] on GaAs (110), where topographical peaks in alternate-bias images were shown to be correlated with the locations of the Ga and As atoms, respectively.

Comparison with Other Techniques

The real strength of STM is its capability for atomic-resolution studies of a wide variety of surfaces in real space. However, there are many complementary techniques with their own unique abilities that can in certain instances provide attractive alternatives to the STM. Transmission electron microscopy (TEM), for example, is a well-established technique that can also in some cases resolve features with atomic dimensions. In most cases, this can be accomplished only by aligning the electron beam with the rows of atoms in a crystalline lattice. Also, the high electron-beam energy required to achieve this short a wavelength causes rapid deterioration of the sample. Nevertheless, the TEM is a very powerful tool, and unlike the STM, it is not limited to the surface layer, nor to electrically conducting samples. Field ion microscopy (FIM) can also be used to

determine surface-structure with atomic-resolution in real space. For FIM, however, the samples must be stable in high fields and must be sharpened into a fine point, thus limiting its general usefulness.

Diffraction techniques are also very powerful for determining atomic structure with high precision. Most notable is x-ray diffraction, which has a long and important history of crystal-structure determinations. Electron diffraction is the surface analog of this technique and has also proved very useful, although it is limited to vacuum environments and is sometimes difficult to interpret because of complicating, multiple-scattering contributions. All the diffraction techniques, however, rely on large-scale order, and can at best give averaged information about local and defect structure. Local scattering experiments such as secondary-ion mass spectrometry (SIMS) and extended x-ray–absorption fine-structure (EXAFS) can yield truly local surface structure, but are again averages over a large ensemble. Other limitations also apply such as surface destruction (SIMS), or strong reliance upon model systems for data interpretation (EXAFS).

Demonstrated Capabilities and Uses

Initial widespread interest in the STM was aroused when Binnig *et al.*[4] presented the first atomically-resolved STM images of the Si (111) 7X7 reconstruction, helping to settle a decade-old controversy as to its structure. Since then, the demonstrated abilities of the STM to provide unique atomic-scale information on a number of surfaces in a variety of environments has continued to expand. Semiconductors have continued to be an especially active area, partly because of their technological importance, but also partly because of the relatively localized nature of the semiconductor surface wave functions (especially the dangling bond states), which provide the contrast necessary for atomic-resolution imaging. The surfaces are also rich with electronic structure that can be probed by means of local (site-specific) current-voltage spectroscopy.

Highly-oriented pyrolytic graphite (HOPG) has also been extensively studied. HOPG was first imaged in ultrahigh vacuum (UHV),[10] but was then also the first surface to be imaged with atomic resolution in air[11] and water.[12] Other layered compounds have also played an important role. TaS_2 and $TaSe_2$, for example, were the first surfaces imaged with atomic resolution in cryogenic liquids.[13] The relative ease of preparation for these samples, where simple cleavage can provide an unreconstructed, inert surface, is in large part responsible for their popularity. However, interesting electronic properties have also been studied, such as charge-density waves on layered dichalcogenides.[14] Also, some unusual and controversial imaging phenomena have been observed, especially on HOPG.[15–20]

Metals have proved much more difficult to image with atomic resolution. This is because the corrugation of the local density of states near the Fermi energy in metals is typically smaller than that of semiconductors or semimetals. Also, clean single-crystal metal surfaces are relatively difficult to prepare. Recently, however, atomic-resolution images of the close-packed surfaces of Au [Ref. 21] (in UHV and in air), and of Al [Ref. 22] have been reported.

The potential for obtaining truly unique information through the imaging and spectroscopic analysis of adsorbates on surfaces has been recognized from the beginning. Initial studies were of atomic species adsorbed on metals,[23] and metals deposited on semiconductors.[24] Choosing a system for which the submolecular structure of an adsorbed molecule can be imaged is a more challenging problem. The molecule must be stable and strongly bound to the surface to avoid being disrupted by forces or fields from the scanning tip; it must be large or have a unique symmetry so that it can be distinguished from the substrate; and conductivity through or around the molecule must be sufficient to support a tunneling current.

The first system in which submolecular resolution was achieved was copper phthalocyanine (Cu-pc) adsorbed on Ag.[25] Later, the molecular orbital structure of Cu-pc was imaged with much more detail on a Cu (100) surface.[26] Another molecular adsorbate system that has been atomically resolved is the co-adsorbed benzene and CO system on Rh (111).[27] One nice, but limited, approach to submolecular imaging has been demonstrated in the study of a crystalline organic conductor, tetrathiafulvalene tetracyanoquinodimethane (TTF-TCNQ).[28] Other organic molecules have been successfully imaged as overlayers on graphite in two-dimensional crystalline form.[29] A spate of papers has also recently appeared on the imaging of DNA with the STM.[30]

Purpose of This Work

The purpose of this work is to examine the applicability of the STM to problems of chemical interest, including structure and chemical bonding. The initial goal is to find out what can be determined regarding chemical identity with the STM. The STM has great potential in this respect through utilization of the different spectroscopic modes, including current-voltage spectroscopy and measurements of the local tunneling barrier height. The major restriction in current-voltage spectroscopy is that the electronic states that are accessible to the STM are those near the Fermi level, which are involved in bonding, instead of the deeper-lying, element-specific, core electronic states, which are typically examined with such techniques as x-ray photoelectron spectroscopy. While this is not a trivial problem, good progress has been made for certain semiconductor surfaces where the spatial distribution of filled and empty electronic states near the Fermi energy is correlated with individual atomic species.[9] Additional studies are needed on different surfaces to examine the general applicability of this method.

Another method that can be used is the examination of the local tunneling barrier height. Theoretical models predict different local wave-function decay lengths, depending on the nature of a local adsorbate on a jellium surface.[31] Additional experimental evidence

is needed to verify these results and to assess the achievable specificity. So, while it is clear that the STM is sensitive to much more than just the topography of a surface, the number of other parameters involved makes the determination of chemical identity a challenging and yet potentially very rewarding problem.

These questions can best be addressed by careful investigations of simple substrates with eventual extension to more complicated systems. A large amount of uncertainty is introduced in many studies because of the use of poorly characterized samples in environments where contamination of the surface is a problem. The extremely low "tunneling" barrier heights seen on graphite in air, for example, revert to values much closer to the accepted ones after baking the graphite in UHV.[18] Also, the use of simple systems will aide in artifact rejection, and in recognition of anomalous imaging conditions and unstable or multiple tip effects.

Summary of Chapters

The remainder of the thesis is organized as follows. Chapter 2 is a summary of instrumental requirements for STM, giving special attention to those features that will aid in achieving the high stability necessary for atomic-resolution imaging. The instrument that we have built is described, and specific examples are taken from its design. Chapter 3 is a study of the surface morphology of MoS_2 as measured by STM. MoS_2 was chosen as an important two-component system on which to examine the selectivity of the STM to structurally and chemically distinct species. The atomic-scale topography is presented, as well as larger-scale images showing a variety of characteristic nanometer scale structures. The effect of imaging at different bias voltages and with different tips is examined. Chapter 4 is the presentation of a simple model for tunneling in ideal metal-insulator-semiconductor junctions such as those encountered in STM of MoS_2. For ideal semiconductor surfaces with no surface-state density in the band gap, the field from the insulator penetrates into the semiconductor, causing band-bending. Some interesting

effects on the current-separation and current-voltage spectroscopies are predicted. Chapter 5 is a study of the surface-averaged *I-V* spectroscopy of MoS_2. A high degree of variability is seen in the *I-V* character of these samples, which may be due in part to inhomogeneities in our mineralogical samples.

References

1. *For a comprehensive review of STM see:* P. K. Hansma, J. Tersoff, *J. Appl. Phys.* **61**(2), R1–23 (1987).
2. R. Young, J. Ward, F. Scire, *Rev. of Sci. Instrum.* **43**(7), 999–1011 (1972).
3. G. Binnig, H. Rohrer, Ch. Gerber, E. Weibel, *Phys. Rev. Lett.* **49**(1), 57–61 (1982).
4. G. Binnig, H. Rohrer, Ch. Gerber, E. Weibel, *Phys. Rev. Lett.* **50**(2), 120–3 (1983).
5. C. B. Duke, *Tunneling in Solids*, Academic, New York (1969) (supplement 10 of series *Solid State Physics*, edited by F. Seitz, D. Turnbull, H. Ehrenreich).
6. J. S. Villarrubia, J. J. Boland, *Phys. Rev. Lett.* **63**(3), 306–9 (1989).
7. J. Bardeen, *Phys. Rev. Lett.* **6**(2), 57–9 (1961).
8. J. Tersoff, D. R. Hamann, *Phys. Rev. Lett.* **50**(25), 1998–2001 (1983); J. Tersoff, D. R. Hamann, *Phys. Rev.* **B 31**(2), 805–13 (1985).
9. R. M. Feenstra, J. A. Stroscio, J. Tersoff, A. P. Fein, *Phys. Rev. Lett.* **58**(12), 1192–5 (1987).
10. G. Binnig, H. Fuchs, Ch. Gerber, H. Rohrer, E. Stoll, E. Tosatti, *Europhys. Lett.* **1**, 31–6 (1986).
11. S. Park, C. F. Quate, *Appl. Phys. Lett.* **48**(2), 112–4 (1986).
12. R. Sonnenfeld, P. K. Hansma, *Science* **232**, 211–3 (1986).
13. R. V. Coleman, B. Drake, P. K. Hansma, G. Slough, *Phys. Rev. Lett.* **55**(4), 394–7 (1985).
14. R. V. Coleman, B. Giambattista, P. K. Hansma, A. Johnson, W. W. McNairy, *Adv. Physics.* **37**(6), 559–644 (1988).
15. S. Morita, S. Tsukada, N. Mikoshiba, *Jap. J. Appl. Phys.* **26**(4), L306–8 (1987).
16. J. Tersoff, *Phys. Rev. Lett.* **57**(4), 440–3 (1986).

17. J. M. Soler, A. M. Baró, N. Garcia, H. Rohrer, *Phys. Rev. Lett.* **57**(4), 444–7 (1986).

18. H. J. Mamin, E. Ganz, D. W. Abraham, R. E. Thomson, J. Clarke, *Phys. Rev.* **B 34**(12), 9015–8 (1986).

19. J. B. Pethica, *Phys. Rev. Lett.* **57**(25), 3235 (1986).

20. H. A. Mizes, S. Park, W. A. Harrison, *Phys. Rev.* **B 36**(8), 4491–4 (1987).

21. V. M. Hallmark, S. Chiang, J. F. Rabolt, J. D. Swalen, R. J. Wilson, *Phys. Rev. Lett.* **59**(25), 2879–82 (1987); Ch. Wöll, S. Chiang, R. J. Wilson, P. H. Lippel, *Phys. Rev.* **B 39**(11), 7988–91 (1989).

22. J. Wintterlin, J. Wiechers, H. Brune, T. Fritsch, H. Höfer, R. J. Behm, *Phys. Rev. Lett.* **62**(1), 59–62 (1989).

23. A. M. Baró, G. Binnig, H. Rohrer, Ch. Gerber, E. Stoll, A. Baratoff, F. Salvan, *Phys. Rev. Lett.* **52**, 1304–7 (1984).

24. R. J. Wilson, S. Chiang, *Phys. Rev. Lett.* **59**(20), 2329–32 (1987); F. Salvan, H. Fuchs, A. Baratoff, G. Binnig, *Surf. Sci.* **162**, 634–9 (1985); J. Nogami, S. Park, C. F. Quate, *Phys. Rev.* **B 36**(11), 6221–4 (1987); R. J. Wilson, S. Chiang, *Phys. Rev. Lett.* **58**(24), 2575–8 (1987).

25. J. K. Gimzewski, E. Stoll, R. R. Schlittler, *Surf. Sci.* **181**(1–2), 267–77 (1987).

26. P. H. Lippel, R. J. Wilson, M. D. Miller, Ch. Wöll, S. Chiang, *Phys. Rev. Lett.* **62**(2), 171–4 (1989).

27. H. Otani, R. J. Wilson, S. Chiang, C. M. Mate, *Phys. Rev. Lett.* **60**(23), 2398–401 (1988).

28. T. Sleator, R. Tycko, *Phys. Rev. Lett.* **60**(14), 1418–21 (1988).

29. J. K. Spong, H. A. Mizes, L. J. LaComb, Jr., M. M. Dovek, J. E. Frommer, J. S. Foster, *Nature* **338**, 137–9 (1989).

30. B. Barris, U. Knipping, S. M. Lindsay, L. Nagahara, T. Thundat, *Biopolymers* **27**(10), 1691–6 (1988); T. P. Beebe, T. E. Wilson, D. F. Ogletree, J. E. Katz, R. Balhorn, *Science* **243**, 370–2 (1989); M. Amrein, R. Durr, A. Stasiak, H. Gross, *Science* **243**, 1708–11 (1989); P. G. Arscott, G. Lee,

V. A. Bloomfield, D. F. Evans, *Nature* **339**(6224), 484–6 (1989); A. Cricent, S. Selci, A. C. Felici, R. Generosi, E. Gori, *Science* **245**(4923), 1226–7 (1989).

31. N. D. Lang, *Phys. Rev. Lett.* **58**(1), 45–8 (1987).

Chapter 2

SCANNING TUNNELING MICROSCOPE DESIGN AND IMPLEMENTATION

Introduction

Scanning tunneling microscopy (STM), though simple in concept, poses a technological challenge in instrumental design. This can be seen in the evolution of instrumentation from the earliest topographiner,[1] through magnetically levitated[2] and spring-suspension[3] STM designs, to the myriad smaller and more compact systems currently in use.[4] The general trend has been toward smaller and more mechanically rigid systems that relax somewhat the need for extensive vibration isolation, while at the same time allowing larger feedback band widths and higher scan speeds. A detailed analysis of the engineering requirements for the STM has been given by Pohl,[5] and a recent review of STM instrumentation is found in the work of Kuk and Silverman.[4]

The most basic technical requirement for STM is the precise relative positioning of two macroscopic objects, the tip and the sample surface. The achievable resolution of the STM has been demonstrated down to about 100 pm in the surface plane, and at least 10 pm in the surface normal. The resolution normal to the surface is typically limited only by the stability of the STM structure and the feedback electronics. In order to take full advantage of the resolution capabilities, the quiescent relative motion of the tip and sample should therefore be limited to about 10 pm in the XY plane and 1 pm in Z. This basic requirement must be met within the constraint of a flexible, precise positioning and scanning mechanism. For high-resolution work, a scan range of 0.1 to 1 μm in the three orthogonal scan directions is typical. The desired control is therefore about 1 part in 10^5. In addition, some provision must be made for careful approach of the tip to the surface from macroscopic distances in such a way that contact between tip and surface is avoided. Some larger-scale positioning capability within the surface plane may also be desired depending on the application.

The other basic requirement for STM operation is the development of a stable electronic feedback control system to maintain the separation between the tip and sample.

In the original topographic imaging mode, it is the feedback control that keeps a constant tunnel gap and causes the tip to follow the surface contours as it is raster-scanned across the sample. In the more recent current-imaging (fast scan) mode, the feedback band width is limited such that only the average tip-sample separation is maintained as the tip is scanned across regions with small-scale corrugation. In this case the topography is inferred from the measured fluctuations in the tunneling current. In either case, the response of the feedback control electronics is crucial in defining the sample topography and in avoiding tip-sample contact.

Other features are often incorporated in STM designs in order to allow specific experiments. One very useful and prevalent addition is the ability to interrupt the feedback control briefly while leaving the tip and sample in place. This permits a form of spectroscopy by allowing the current-voltage characteristics to be measured at a constant separation. Other forms of spectroscopy are achieved by adding a modulation to either the tunneling bias or the tip-displacement control voltages and then detecting that frequency component in the current by lock-in detection.

For many studies, the operating environment or temperature may also be critical. Our STM operates within an ultrahigh vacuum (UHV) environment so that surfaces free from atmospheric contaminants can be prepared and observed. Additionally, our instrument has been interfaced with a microprocessor for control of the STM and for data acquisition and display.

Vibration Control

One of the most obvious and most crucial requirement for practicing STM is the suppression of any uncontrolled relative motion between the tunneling electrodes to a level below the design objectives stated above. It was a failure in this requirement that limited the earliest attempts at tunneling microscopy,[1] and which continues to limit certain experiments such as attempts to perform inelastic electron-tunneling spectroscopy with

the STM. The relative motion between the tip and sample can be excited by the motion of the STM supporting structure (*i. e.*, the floor), by acoustic coupling, or by the act of scanning the STM tip or of making an approach to the sample. Since our STM is a vacuum instrument, the only external excitations we will be concerned with are those from floor motion, or those from acoustical coupling through the supporting structures. Typical building vibrations are largely concentrated in the low-frequency ranges, with the amplitude dropping with the inverse of frequency, but with spikes at special frequencies corresponding to the flexure modes of the building, and at 60 Hz and subharmonics due to electrical machinery. The amplitude of these excitations is typically of order 1 μm. The signal of interest in the STM experiment will usually lie in the 20 to 1000 Hz range, depending on the scan rate and the size of the features to be examined. Therefore, careful consideration into the suppression of these building vibrations is necessary.

There are two basic factors that can be optimized to limit the relative motion between the tip and the sample—the degree of decoupling of the tip-sample system from the disturbing influences, and the rigidity of the tip-sample coupling. Both of these factors are always present whether they are explicitly designed or are simply due to the properties of the structural materials, and any analysis of the performance of an STM design must take both into account.

Vibration Isolation

Figure 1 is a diagram of an idealized model for an STM and its support system assuming point masses and discrete structural elements. The diagram is limited to one degree of freedom, but the general principles can be extended in a straightforward way. The STM is vibrationally isolated from its support by means of a spring of force constant k_s, whose motion is damped by a viscous damping factor b_s. Within our model, the equation of motion for the STM system relative to its support is[6]

$$\ddot{x}_s + \gamma_s(\dot{x}_s - \dot{x}_0) + (2\pi\nu_s)^2(x_s - x_0) = 0, \qquad (1)$$

where x_0 and x_s describe the motion of the support and the STM, respectively, in an inertial frame, $\gamma_s = (b_s/m_s)$ is the normalized damping factor, $\nu_s = (1/2\pi)\sqrt{k_s/m_s}$ is the natural resonance, and m_s is the mass of the total STM assembly. The frequency dependence of the transmitted vibration amplitudes can be extracted by considering the response of the STM assembly to a sinusoidal excitation of the support at frequency ν. The transfer function, which is the ratio of the transmitted to the exciting vibrational amplitudes, is then given by

$$T = \left|\frac{x_s}{x_0}\right| = \left[\frac{1 + (\nu/\nu_s)^2/Q_s^2}{(1 - (\nu/\nu_s)^2)^2 + (\nu/\nu_s)^2/Q_s^2}\right]^{1/2}, \qquad (2)$$

where Q_s is the dimensionless oscillator quality factor $(2\pi\nu_s/\gamma_s)$. Figure 2 shows a plot of this transfer function T for several values of Q_s. We see from the figure that the attenuation of the external vibrations which we desire happens only above a critical frequency $\Omega_c = (\nu/\nu_s)\sqrt{2}$. Below Ω_c, the support motion is actually amplified by the isolation system. As $\nu \to \infty$ in this idealized model, the ratio of transmitted to incident vibrational amplitudes drops like $(1/\nu)$. However, in the range of frequencies between Ω_c and $(\nu/\nu_s)Q_s$, the transmissibility factor falls off like $1/\nu^2$.

It is clear from Fig. 2 that the best vibration isolation properties at any particular frequency above resonance will be obtained by minimizing ν_s. The limit as to how small ν_s can be made is given by the extension limit of the spring. We have assumed a spring that obeys Hooke's law, $F = -k_s\delta x$. Combining this with the definition of ν_s yields

$$\nu_s = (1/2\pi)\sqrt{g/\delta x}\,, \qquad (3)$$

since $F = m_s g$, where g is the gravitational acceleration constant. To obtain a resonance for the system of 1 Hz therefore requires a spring extension (or compression) length of 25 cm.

The other obvious criterion in Fig. 2 is that the vibration isolation efficiency is strongly dependent on the mechanical quality factor. As Q_s decreases, the peak at resonance decreases almost proportionately; however, this is accompanied by a concomitant decrease in the the attenuation at frequencies above Ω_c. Therefore, to maximize the vibration isolation properties of a system, the damping should be minimized within the constraint that too large a peak at resonance is not created. This is, of course, dependent on the individual application. For STM vibration-isolation systems, the typical value of Q_s is about 5.

The vibration-isolation efficiency can be enhanced by staging more than one spring and mass combination. A comparison between single and double stages of vibration isolation with specific application to STM has been presented by Park and Quate.[7] In the limit of non-interacting stages, which can be approached in practice by means of a large mass mismatch from one stage to the next, the transfer function for a multiple stage system is simply the product of that of the individual stages. However, in order to add a second stage of the same resonant frequency, the overall spring extension length must be doubled. Because of space constraints, this often requires overlapping the stages, which can be difficult in practice since overlapped stages are often laterally unstable. Alternatively, a single stage could be converted to a dual stage by halving the extension of each stage. This would increase the resonant frequency by a factor of $\sqrt{2}$, which in some cases could be a serious disadvantage. However, above Ω_c, the rate of fall-off would be doubled so that at higher frequencies, the double stage would again outperform the single stage. In Fig. 3, the transfer function of a one-stage vibration-

isolation system is compared to that of a two-stage system where both have the same overall spring-extension length and where a mechanical Q of 5 is used for all stages.

Microscope Rigidity

The rigidity of the tip-sample coupling is the other major mechanical factor for improving vibrational immunity. Though the mechanical loop between the tip and the sample is usually some combination of piezoelectric ceramics and metal slabs, small amplitude motions between tip and sample will still have a definite resonant frequency ν_t and quality factor Q_t, and the system can be modeled as a damped harmonic oscillator with force constant $k_t = m_t(2\pi\nu_t)^2$ and damping factor $\gamma_t = b_t/m_t = 2\pi\nu_t/Q_t$, where m_t is the mass of the tip assembly. The equation of motion is

$$\ddot{x}_t + \gamma_t(\dot{x}_t - \dot{x}_s) + (2\pi\nu_t)^2(x_t - x_s) = 0, \tag{4}$$

where the displacements are defined in Fig. 1. Following the same single-frequency approach as before, the motion of the STM sample support and the tip as a function of frequency can be obtained. The quantity of interest in this case is the relative displacement S between tip and sample, which is given by

$$S = \left|\frac{x_t - x_s}{x_s}\right| = \frac{(\nu/\nu_t)^2}{\left[(1 - (\nu/\nu_t)^2)^2 + (\nu/\nu_t)^2/Q_t^2\right]^{1/2}} . \tag{5}$$

This function is plotted in Fig. 4 for several values of Q_t. Above resonance in this one-dimensional, simple harmonic oscillator model, $S = 1$, which means that any motion of the tip or sample is directly translated into a relative motion between the two. In real systems, above the first resonance, there are typically other resonances that may be of greater amplitude. Below resonance, as ν decreases, the relative motion between tip and surface decreases with a ν^2 dependence, independent of the parameter Q_t. In this case, then, there is no advantage in maintaining high Q_t, and critical damping (Q_t=1) is ideal.

DiLella *et al.*[8] have taken advantage of this fact and have demonstrated increased stability of the feedback control system by potting their piezoceramic scanner tubes in an elastomer, thus decreasing the normally high mechanical Q. The quadratic behavior of S in frequency points to the importance of maintaining a rigid STM structure for increased vibrational immunity, even for low-frequency excitations. For example, doubling the first resonance will result in a factor of 4 reduction of the relative tip-sample motion for frequencies below resonance. For typical STM's, the stiffness and mass of the tip and scanner assembly result in a resonant frequency ranging from 1 to 20 kHz.

Since $\nu_t = (1/2\pi)\sqrt{k_t/m_t}$, to obtain a high first resonance for the STM, the mass of the scanner must be minimized, and the effective spring constant k_t must be maximized. Miniaturization is the most elegant and effective solution to this requirement. The resonant frequency of a beam, for example, is proportional to its thickness divided by its length squared.[5] Halving all dimensions will therefore approximately half the resonant frequency. Also, all the connections around the mechanical loop need to be as rigid as possible. The limitations on how small and rigid the STM can be made come from the minimum length of the piezoceramics necessary to achieve the desired scan range, and from the necessity for a coarse approach mechanism. The resonant frequency of the piezoelectric scanner itself is oftentimes the most critical, since it is the scanner that is directly excited by the electronic feedback control, and by scanning. The scanner is typically lighter than the rest of the STM; therefore, coupling to its motion is somewhat attenuated by the mass differences. Increasing the resonant frequency of the scanner has an added attraction, since this permits a faster feedback response in the electronics and a more accurate tracking of the surface.

Composite Transfer Function

The effect of external vibrations on the tip-sample separation is attenuated by both the vibration-isolation system and by the stiffness or rigidity of the STM structure. Plot-

ted in Fig. 5 is the vibrational filtering function, which is the transmissibility ratio times the stiffness factor. For this plot, the vibration isolation consists of a single stage with a 1 Hz resonant frequency and a Q_s of 5, and the tip-sample coupling is assumed to have a first resonance at 10 kHz and a Q_t of 100. In the range of frequencies of interest, the vibration attenuation is better than 10^{-7}, meaning that a 1 μm floor vibration translates to a 10 pm motion between the tip and sample. This is adequate for most STM topographical experiments. Because of the ν^2 behavior of S below resonance, and the $1/\nu$ behavior of T at frequencies well above resonance, about a factor of two more vibration immunity can be gained by doubling ν_t than would be achieved by halving ν_s. This emphasizes that although the design of the vibration isolation system is fundamental in STM operation, more is to be gained in principle by designing a rigid STM structure with a high first mechanical resonance. Of course, if an additional stage of vibration isolation is included, the attenuation that is due to T above resonance becomes proportional to $1/\nu^2$, meaning that between the resonance of T and S, the amplitude of the composite transfer function is independent of frequency instead of increasing as ν. This probably isn't as advantageous as it might at first seem, since the floor excitations decrease as $1/\nu$.

Besides external vibrations coming through the STM supports that are due either to floor motion or to acoustic coupling, the other major source of vibrations in an operating STM are the motions of the high-resolution XYZ translator necessary for scanning and for maintaining feedback. In this case, the vibrations are attenuated only by the stiffness and damping factors of the STM scanner and tip-sample coupling. Well below resonance, the piezoceramic displacement is approximately proportional to the applied voltage. If electrical signals with frequency components at or above resonance are applied either to the X and Y ceramics for scanning (for example, from unfiltered digitally ramped voltages, or from triangle or sawtooth analog ramps) or to the Z ceramic (from too wide a feedback band width), instabilities can result. In the simple harmonic oscillator

model, not only is there a peak in the amplitude at resonance which is equal to Q_t, meaning that the scan motion would be amplified, there is also a 180° phase shift in the response as the frequency is increased through resonance, meaning that at these frequencies, the tip is actually moving opposite to the direction of the applied voltage. For the feedback control loop on the Z piezoceramic, this means that positive feedback, and a driven oscillator would result if the loop gain at that frequency were greater than one. In practice, then, the stiffness of the STM assembly not only influences the external vibration immunity; it also limits the achievable feedback band width and scan speed.

The principles arrived at in the preceding sections, while strictly true only for the model systems presented, provide a qualitative understanding of the important parameters in vibration control. A more rigorous treatment of vibration-isolation systems is found in the classic work of den Hartog.[9] In particular, although the ν^2 dependence of the stiffness function below the first resonance is fairly certain, the attenuations that are due to vibration isolation systems do not decrease indefinitely with increasing frequency. Also, if springs are used, for example, resonance peaks are often found above the fundamental because of other spring vibrational modes. In practice, spectrum analysis of the current signal and of the Z piezoceramic voltage from an STM in feedback gives a very good indication of problem frequencies. Depending on the frequency range of the interference, the vibration isolation system or the STM itself can be modified to alleviate the problem.

Implementation

The vibration-isolation system we have built for our STM is shown schematically in Fig. 6. We have combined two stages of spring-suspension vibration isolation with a stack of stainless steel plates and Viton rubber spacers. The inner springs have an extension δx of about 25 cm and a first resonance of 1 Hz or less in all six fundamental modes. Because of space constraints, the two stages had to be overlapped. We first attempted to overlap the stages with equal extension lengths. This proved impossible

because of lateral instabilities. What we find is that any lateral motion of the inner stage causes a shift in the center of mass for the outer spring supports. This causes the outer stage to tilt in a direction that increases the lateral displacement of the inner spring mass, thus causing positive feedback. In principle this problem could be alleviated by adding mass to the outer stage below the suspension point and stiffening the outer springs. Instead, we shortened the outer springs, leaving an extension length of 4 cm and resonances in the vertical, rotational, horizontal, and rocking modes ranging from 3 to 20 Hz. The motion of the stages is damped by magnetic eddy currents in copper blocks. The magnets are on the first stage of suspension, and the copper blocks are on the inner stage and on the outer support, so that the damping for both stages is proportional to the motion of that stage relative to its support. The mechanical Q for both stages is about 5. In addition to this damping, a thin Viton thread is woven through each of the inner stage springs, and all of the springs are suspended by means of Viton O-ring links. This Viton helps to damp the spring surge modes (vibrations of the individual spring coils relative to each other) and the acoustic modes through the spring material.

The innermost vibration-isolation platform consists of 5 stages of stainless steel plates separated by Viton rubber spacers. The STM fine XYZ scanner is built into the top stage. This stainless steel stack is similar to the vibration isolation in the "pocket" STM design of Gerber *et al.*[10] The cross section of the Viton spacers is minimized to give the smallest possible effective spring constant between stages. An optimized vibration isolation stage of this type has been analyzed by Okano *et al.*[11] At 100 Hz, less than a factor of 10 attenuation of incident excitations was found. A direct comparison of the vibrational stability with and without the stainless steel stack has not been done for our instrument. Given the short static deflection of the elastomer and the work of Okano *et al.*, we suspect that the stainless-steel-stack isolation stage adds little to the overall vibrational stability; however, it probably doesn't hurt, and it may help with acoustic decoupling.

In addition to these components inside the vacuum system, there are rubber pads under the UHV chamber supports. The vertical first resonance for the rubber-pad vacuum-chamber system seems to be about 20 Hz. This is unfortunate, because it means that the 20 Hz peak in our floor spectrum is probably amplified by this stage. Nevertheless, we have compared the vibrational noise with and without the rubber feet, and the STM appears to work better with the rubber pads. The horizontal rocking mode is about 2 Hz because of the high center of mass of our UHV chamber.

Microscope Design

Requirements

The STM stage itself is the next conceptual piece in the design. Herein lies the real heart of the microscope—the coarse approach mechanism and the high-resolution XYZ scanner. The coarse approach must be able to bring the sample and tip from macroscopic distances into the range of the XYZ scanner. The total travel of the coarse approach must therefore be at least around 1 mm. The sensitivity necessary for the coarse approach is set by the maximum range of the scanner. The minimum coarse approach increment should be no more than about one-fourth of the total XYZ scanner range so that the sample can be placed near the center of the XYZ scanner range. The coarse approach mechanism should also be as rigid as possible for attenuation of incident vibrations.

The XYZ scanner range is a product of the range of the supply voltages and the expansion coefficient, E, of the piezoceramic elements. A large Z scanner range is desirable for ease of approach, and a large X, Y, and Z range is necessary for performing large area scans or for choosing widely separated regions for small area scans. However, this must be balanced against the high-resolution requirements. The noise motion of the scanner is the product of E and the ceramic high-voltage amplifier noise voltage. For high-voltage piezoceramic drivers with a 10 kHz band width, 5 mV of

noise peak to peak is typical. This means that to meet a design objective of 1 pm normal to the surface, an expansion coefficient of no more than about 1 nm/V must be used. This will limit the total scan range to about 1 μm, depending on the maximum voltage output of the drivers. Also, E is the product of the intrinsic expansion coefficient for the material and the size of the piezoceramic element. Therefore, in order to increase E, the size of the scanner must be increased. This in turn limits the vibrational stability as discussed above.

The stability of the tip-sample separation in the presence of temperature fluctuations is another design consideration. Because of the different thermal expansion coefficients of the materials that comprise the mechanical loop connecting tip and sample, changes in the temperature will cause a change in the separation between tip and sample. Typical thermal expansion coefficients are ~ 10^{-5} °C^{-1}. For a 1 cm path length, and differences in thermal expansion coefficients of even as low as 10^{-6} °C^{-1}, a separation change of about 10 nm/°C is expected. Careful matching of thermal expansion coefficients and miniaturization of the mechanical loop can reduce this by as much as a factor of 100. Maintaining a fairly constant temperature during an STM scan will still be necessary, however.

Implementation

The STM stage that we have built is designed after the "pocket" STM.[10] Figure 7 shows a top and side view of the XYZ translator and coarse approach mechanism. Coarse positioning is done using a piezoceramic louse. The louse walks over the surface of the stage in an inchworm fashion by expanding and contracting the piezoceramic body while alternately applying voltages to clamp and release the aluminum feet electrostatically. The dielectric for the electrostatic clamping is provided both by anodization of the aluminum and by a thick thermal oxide on the silicon wafer on which the louse walks. This dual dielectric eliminates much of the unreliability that other researchers have found using louse walkers. Clamping of the feet requires about 200 V, and with our geometric

arrangement and louse size, a step of about 50 nm can be obtained with a 200 V pulse. For very large-scale adjustments, step sizes up to 1000 V are often used. Smaller steps can be readily obtained by lowering the louse ceramic voltage; however, the steps are not as reproducible, and the rate of walking for forward *versus* reverse motion is sometimes very different. In practice, coarse approach is usually done with the more reliable 50 to 100 nm steps. Once in range of the fine positioning XYZ translator, smaller steps may be taken to adjust the position of the sample to near the center of the XYZ translator range.

Using a louse for the coarse positioning mechanism has some intrinsic advantages and disadvantages over other methods. The other most commonly used method involves micrometers or screws with either lever or differential-spring motion reduction. Within these other designs, lateral coarse positioning can be inconvenient. With the louse, on the other hand, sideways motion is very easily included in at least one dimension. For most high-resolution work, this is all that is necessary since the lateral positioning is mostly used to move to a different area of a macroscopically homogeneous surface rather than to locate a specific surface feature for study. However, the disadvantages of using a louse can be rather serious. The louse design is intrinsically less rigid and thermally stable than most of the other methods of coarse approach. This is due to the relatively long mechanical loop between the tip and the sample, and to the inherently non-rigid coupling between the sliding feet and the walking surface. In our STM, for example, we see a definite frequency component of the tunneling current at about 1 kHz, which we have attributed to the louse.

The voltage pulses for the louse are under computer control. Digital input and output (DIO) lines are interfaced through optical couplers and transistors to high-voltage relays that switch the voltage from adjustable-output high-voltage supplies. The computer control increases the flexibility in allowing different pulse sequences for walking in different directions or for causing the louse to rotate. Also, the rate of stepping is easily

varied. The size of the steps and the magnitude of the clamping voltage is conveniently adjustable through the variable output power supplies.

The XYZ translator is made up of three orthogonal piezoceramic beams, each with an overall length of about 25 mm, and a 2×3 mm cross section. These ceramics, as well as those on the louse, are fashioned from slabs of PZT–5A, which has a relatively low piezoelectric expansion coefficient, but a high depoling temperature of 365 °C, which is important to allow baking of the UHV system. The expansion coefficients for the X, Y, and Z ceramics for the dimensions used are about 1 nm/V. The lowest frequency cross resonance, measured as the voltage induced on one of the X, Y, or Z ceramics when another is driven, is at about 4.5 kHz for this scanner. Since this STM was designed, a different kind of scanner has been described for use in STM.[12] This new scanner consists of a single piezoceramic tube oriented with the tip sticking out the end. The outer electrode surface of the tube is cut in quarters so that a voltage on any one quarter will provide a motion in the XY plane by bending the tube. The Z motion is provided in the usual way by a field between the inner and outer tube surfaces. This type of scanner is in general preferable, since first resonances as high as 30 kHz can be obtained for a tube 6 mm long with a 3 mm outside diameter. A tube of these dimensions would still have a similar expansion coefficient in X, Y and Z to the scanner we have used. Also, the smaller mass would result in less coupling of the scanner excitations to the rest of the STM system.

We have chosen to use ±150 V operational amplifiers to drive the X, Y, and Z piezoceramics. With this voltage range and our expansion coefficient of 1 nm/V, the total range of motion in the three orthogonal directions is about 0.3 μm. Thermal drift in vacuum is as low as 0.2 nm/min, once the temperature has stabilized. The act of scanning may cause a certain amount of thermal drift because of the slight heating of the ceramics that is due to internal friction.

Feedback

The electronic feedback and control system is the other essential requirement for STM. Once the tip and surface are brought to within the Z piezoceramic range using the coarse approach mechanism, the feedback system takes over the control of the Z piezoceramic voltage. The Z piezoceramic voltage is constantly adjusted to maintain a constant tip-sample separation in the presence of thermal drift, vibrational noise, and differences in surface topographic height encountered in scanning. The feedback system must be fast in order to track the surface accurately at high scan speeds, and must have a high gain to minimize sag from the control set point at the extremes of the Z range. These band width and gain objectives must be met within the constraint that they not be so large as to cause positive-feedback oscillations.

The design of control systems is a very mature field; nevertheless, despite the importance of this part of an STM system, the feedback control system is rarely analyzed in depth in designing STM electronics. This may be due in part to the highly variable nature of the tip-sample interaction. Ideally, the current-separation dependence of the tunneling junction should be exponential. This is, in fact, the observation for some of the clean tip-sample combinations that can be prepared in vacuum.[2] In air, and for dirty surfaces in vacuum, a different current-separation dependence is found. Jahanmir *et al.*[13] have fit their current-voltage curves acquired in air to a Schottky emission equation. Quasi-linear current-separation curves have also been seen. What is needed in practice then is a feedback loop with adjustable gain and band width that can be optimized for the particular operating conditions encountered.

The general form of most STM feedback control systems is similar. A stable voltage supply feeds the current through the tunnel gap into a high-gain electrometer. In some installations, the electrometer output voltage is fed through a logarithmic amplifier in an attempt to linearize the presumed exponential dependence of current on the

separation, and to increase the dynamic range. Next, the output of the logarithmic amplifier is compared to a feedback set point. Then there is an adjustable band-width limit followed by a high voltage amplifier for driving the Z piezoceramic. The current *versus* separation characteristic of the tunnel junction completes the feedback loop.

Design Criteria

The most important issue from the point of view of STM feedback design is the maximization of the response while avoiding oscillations. This is achieved be setting the unity gain crossover of the loop gain below the first mechanical resonance, and by avoiding more than 135° phase shift in the electronics before this unity gain crossover. The second requirement is met by having a dominant pole in the feedback system at a low frequency, which introduces a 90° phase shift but is necessary for setting the band width, and then insuring that all the other components in the feedback loop introduce a cumulative of less than 45° phase shift . This is approximately equivalent to requiring that all the components besides the dominant pole have a flat amplitude response out beyond the unity gain crossover of the loop gain.

The loop gain for the system is just the product of all the gains of the individual components around the feedback loop. For a system without a logarithmic amplifier, this would include G_e, the electrometer gain, G_i, the integrator or RC filter gain, G_{hv}, the high-voltage amplifier gain, E_Z, the Z piezoceramic gain, and the quantity (dI/dz), which is the change in the current as a function of the tip motion in the Z direction. The first mechanical resonance will typically be 10 kHz or less, so it is relatively easy to ensure that all the electronic components have at least this large a band pass. The frequency-dependent gain of an ideal integrator is given by $G_i = \frac{1}{\omega R C}$. Assuming the form of the tunneling current, $I \propto (V/s)\exp(-A\phi^{1/2}s)$, where s is the separation between tip and sample, ϕ is the barrier height, and $A = \frac{2\sqrt{2m}}{\hbar} = 10.3\ \mathrm{eV}^{-1/2}\mathrm{nm}^{-1}$, we find that $(dI/dz) = I\,[\frac{1}{s} + A\phi^{1/2}]$. For small variations in z, this yields an overall loop gain of

$$H = \frac{G_e G_{hv} E_Z I}{\omega RC}\left[\frac{1}{s} + A\phi^{1/2}\right]. \tag{6}$$

The unity gain crossover is evidently given by

$$\omega_1 = \frac{G_e G_{hv} E_Z I}{RC}\left[\frac{1}{s} + A\phi^{1/2}\right]. \tag{7}$$

For this feedback scheme that does not use a log amp, if we assume an exponential dependence of the current on the separation, we find that ω_1 is proportional to the tunneling current. This means that increasing the feedback set point by a factor of ten will increase the effective feedback band width by a factor of ten. This could easily lead to oscillations unless compensated either by lowering the loop gain or by increasing the RC time constant. Also, deviations from the current set point are subject to a different rate of correction, depending on whether the current is too high or too low. With clean surfaces in UHV, the quantity $A\phi^{1/2}$ is expected to be about 20 nm^{-1}. The quantity $(1/s)$, which is approximately equal to 1 nm^{-1}, is therefore negligible by comparison, and we find that the feedback band width is proportional to $\phi^{1/2}$.

When a logarithmic amplifier is included in the loop, the dependence of the loop gain and the unity gain crossover point on the magnitude of the tunneling current is removed. In our control circuit, the logarithmic amplifier is placed after the electrometer. This has the effect of changing the loop gain to

$$H = \frac{G_{hv} E_Z k}{\omega RC}\left[\frac{1}{s} + A\phi^{1/2}\right], \tag{8}$$

where k is the gain of the log amp $[G_{log\ amp} = k \ln(V_{in}/V_{ref})]$. The unity gain crossover is given by

$$\omega_1 = \frac{G_{hv} E_Z k}{RC}\left[\frac{1}{s} + A\phi^{1/2}\right]. \tag{9}$$

In this case, it is clear that the feedback band width and unity gain crossover point are dependent neither on the magnitude of the tunneling current nor on the electrometer gain.

This means that a smaller range of RC will suffice to provide stability for a greater range of operating conditions. Also, the rate of response to a separation error becomes the same for the separation's being too large as for the separation's being too small. That is, the effective loop gain no longer changes depending on which side of (and how far from) the current set point you deviate. This supposed linearization of response depends on the exponential current-separation relationship. For contaminated surfaces, a much weaker dependence is often found,[13,14] and the feedback loop without the logarithmic amplifier may be found to be superior.

Other elements that must be considered in the design of the control electronics are the overall noise and the maximum gain and voltage amplitude. For achieving a noise level in the tunnel gap width of less than 1 pm with a Z piezoceramic expansion factor of 1 nm/V requires limiting the output noise on the high-voltage piezo amplifier to 1 mV within the measurement band width of ~ 1 kHz. Techniques for limiting noise include putting the electrometer as close to the tunnel junction as possible. This also increases the measurement band width for the current because one of the major limitations is the RC time constant that is due to the high tunnel resistance and the stray capacitance on the current lead. Other common sources of noise are improperly filtered power supplies and ground loops. The maximum voltage provided by the high-voltage amplifier should be sufficient to achieve the desired scan range given the expansion coefficients of the piezoceramic drivers. Also, the low-frequency gain should be great enough to avoid significant deviations from the current set point for the maximum extension of the Z piezoceramic.

Electronic Hardware

A block diagram of the electronics we use for the feedback control is given in Fig. 8. The feedback bias voltage V_b is supplied either from a digital-to-analog converter (DAC) in the computer back plane, or from a battery with a voltage divider. The computer-controlled V_b is advantageous for flexibility and convenience, especially when

performing computer-controlled I-V or s-V measurements. The battery supply, on the other hand, is necessary for low V_b work because of the noise on the DAC.

The virtual-ground current amplifier we have used is a commercial electrometer (Kiethley model 427) located outside the UHV system. The relatively long lead from inside the UHV bell jar to the input of the electrometer is the biggest disadvantage of this method. Our stray capacitance is about 500 pF, which means that at a typical tunnel resistance of 10 MΩ, our current measurement band width is limited to 1 kHz. Offsetting this drawback is the convenience of an easily selectable gain and filtering function, as well as a built-in offset current. Also, the electrometer can be removed for baking the UHV chamber, for repairs, and for its own protection when applying higher voltages or currents to the tunnel junction (e. g., for tip cleaning), which might damage the sensitive circuitry in the electrometer.

Next in the feedback loop is an absolute value circuit, which is a packaged modulator/demodulator (Analog Devices model AD630). Then there is a logarithmic amplifier (Burr Brown model LOG100), which we have configured for a transfer function of $G_{log\ amp} = 2.3\ \log(V_{in}/\ 0.1\ \text{V})$. The factor of 2.3 converts the base 10 log to a natural log, and the 0.1 V provides a built-in reference against which the output of the electrometer is compared, and which serves as the feedback set point. The 0.1 V reference is front-panel adjustable (separately from the prefactor) for changing the feedback current levels. Feedback current levels can also be changed by factors of 10 by changing the electrometer gain.

The feedback band width is set by a gated integrator, which is a circuit board level module from Evans Electronics. The supplied resistor was changed to a 100 kΩ ten-turn potentiometer in series with a 2 kΩ resistor, and the on board capacitor was changed for switch-selectable 10, 1, 0.1, and 0.01 μF capacitors. Also available with the capacitor switch is a 10 Ω resistor for hardware zeroing of the output. A gain of ×2 was inserted

in the integrator output line to increase the output range to ±10 V. The gating and reset functions of the integrator are controlled from the microprocessor using DIO lines. This capability is used in the automatic approach mode, and for breaking the feedback loop without resetting the integrator, which is used in constant s current-voltage spectroscopy. The gated integrator is the equivalent of a high DC gain amplifier, combined with a low band pass RC filter, and a sample and hold circuit which, because of the large capacitance values, has extremely low sag. With these components, the available RC time constants range from 2×10^{-5} sec to 1 sec. Also available on the front panel are other inputs with resistances of 1 and 10 MΩ for extremely low band width operation. The typical operating condition is about 0.1 sec.

Next in the loop is the high-voltage amplifier that drives the Z piezoceramic. For this driver we have used ±150 V operational amplifiers (Burr Brown model 3584) and a gain of ×15 for the input line from the integrator so that the ±10 V integrator output controls the full range. Other input lines are summed into the output: an internal potentiometer controllable offset bias, an external offset bias input, and a unity gain input to the summing node, which can be used for modulating the Z piezoceramic voltage (and hence the tip-sample separation) for extraction of the tunneling barrier height. The internal offset bias is used to bring the integrator output voltage near zero. The adjusted low-voltage output from the integrator can then be amplified to increase the sensitivity when digitizing the Z ceramic voltage. This same high-voltage amplifier module has separate drivers for the X and the Y piezoceramics. These are each equipped with two inputs, one with a gain of ×15 and the other with a gain of ×1.

The piezoceramics have been discussed in a previous section. Their expansion coefficient is about 1 nm/V. From Eq. (9), the unity gain crossover of the loop gain for our feedback control system is then about 3 kHz for an RC time constant of 0.1 sec and an assumed tunneling barrier height of 1 eV. The DC gain is given by the same

formula except that the factor of $\frac{1}{RC}$ for the integrator is replaced by the integrator open-loop gain which is about 10^5. This gives a DC gain of about 10^7.

Computer Control of Operational Modes

The operation of the STM is largely under microprocessor control. The microprocessor is a Sperry PC/IT with an Intel 80286 processor, a 1.2 Mbyte floppy drive and a 40 MB hard drive. In the back plane we have also included an 8 port differential ended 12 bit analog-to-digital converter (ADC), which also has two 12 bit DAC's (Data Translation model 2821), a 4 channel 12 bit DAC with 24 parallel DIO lines (Scientific Solutions model DADIO), an additional 2 MB of random access memory, and a 1024×1024 bit resolution 256 color graphics board (Vectrix model PEPE). The graphics board has its own monitor, a 19" color monitor with a 60 Hz refresh rate (Mitsubishi). This configuration is schematically pictured in Fig. 9.

Coarse Approach

The first operational procedure to be performed on any sample loaded into the STM is a careful approach of the sample and tip. This approach must be done in such a way as to avoid tip-sample contact. Two basic schemes have been used for accomplishing this in the various STM instruments. One method is to keep the Z piezoceramic fully extended as the coarse approach mechanism is advanced. Then, as soon as any tunneling current is sensed, the approach is immediately stopped and a comparator quickly causes the Z piezoceramic to contract fully. There are two necessary conditions for this scheme to work. One is that the coarse approach must be moving slowly and accurately enough to be able to stop within the Z piezoceramic range after the tunneling current is sensed. The other requirement is that the current be sensed quickly enough and the Z piezoceramic be retracted fast enough to exceed the rate of approach of the coarse positioning mechanism. Some margin of safety can be added by using a large tip-sample bias voltage for the

approach, and a low current-comparator threshold so that the tip and sample are farther apart when the tunnel current is sensed.

The other method of coarse approach is sometimes called the woodpecker mode. In this method, the coarse approach mechanism is advanced in a stepwise fashion. During each step, the Z piezoceramic is in its fully retracted position, and after each step is completed, the Z piezoceramic is slowly extended to its full length, all the while checking for a tunneling current. No requirement is made of the rate of the coarse approach using this method, only that its minimum achievable step size be smaller than the Z piezoceramic range. Also, the demands of the current sensing are only those normally encountered in feedback. The only disadvantage of this method is that it can be much slower.

We have used the woodpecker approach in our STM. The Z piezoceramic is retracted by resetting the integrator and by applying an additional offset bias from one of the computer DAC's through the summing node of the HV piezoceramic driver. The louse is then stepped under computer control, after which the integrator gate is opened, allowing the Z piezoceramic voltage to increase at a rate set by the feedback RC time constant. If the louse has brought the sample within range, feedback will be established, if not, the Z ceramic is retracted, and another step is taken with the louse. Once the sample is within range of the Z piezoceramic, its position relative to the Z piezoceramic zero can be adjusted by retracting the Z piezoceramic either under computer or manual control, taking small steps either forward or backward with the louse (under computer control), and then again closing the integrator gate.

Topographic Imaging Mode

Once the sample has been brought within the range of the fine XYZ positioner, topographical or spectroscopic scans can be performed. Our topographical scans are typically done under microprocessor control. The X and Y raster-scan pattern is generated by the computer and output on two of the 12 bit DAC's. This scan voltage is then fed into

the piezo driver circuit, either through the ×1 input for a maximum scan range of about 20 nm in X and Y with a 5 pm minimum step size, or through the ×15 input for a maximum scan range of 300 nm, but with a resolution limited to 75 pm. At each pixel location in the scan, the Z ceramic voltage is digitized through one of the 12 bit ADC's. For low resolution, larger Z range scans, the output of the integrator can be digitized directly. For high-resolution work, the internal offset bias of the Z piezo driver is manually adjusted to provide most of the offset voltage to the Z piezoceramic, thus bringing the output of the integrator close to ground. This integrator output is then amplified by a factor of 15 before digitization so that changes in the digitized voltage correspond one to one with the changes in the actual output voltage. With this method, the Z digitization resolution is 5 pm and the maximum variation that can be measured within a scan is 20 nm. To achieve a higher resolution, the digitization gain can be increased under software control by a factor of 2, 4, or 8, with a proportionate decrease in maximum Z range.

As each data point is acquired, a representation of the trajectory followed by the tip is plotted on the high-resolution graphics monitor. Basically, the graphics capability is used as a high-speed XY recorder, plotting the X coordinate of the scan *versus* the sum of the Y coordinate and the Z variation. The screen can also be split so that the forward scan is plotted on one-half and the reverse scan on the other. Forward and reverse scans are not included in the same image because there is usually a shift between the two, which is normally attributed to piezoceramic hysteresis, but in severe cases may actually be due to a bending motion of the microscopic tip as it scans across the surface in light contact. Friction between the tip and sample could provide a scan-direction dependent force, which would tend to shift the images relative to each other. Evidence for frictional force is sometimes seen in current-imaging, where decreasing the tunnel gap resistance can increase the amount of shift between scans or increase the smearing or apparent stretching of features at the beginning of a scan line.

At the end of each scan line, the data for that scan line are stored to a virtual disk in the auxiliary memory. After the scan, this virtual disk file can be renamed and stored on a floppy disk or on the hard-disk drive. The scan speed can be adjusted by inserting a delay between steps in the XY raster pattern, by stepping in smaller increments than the increments at which you are storing the data (this is often a prudent thing to do anyway to avoid tip-surface contact at a large vertical feature), or by multiple digitizations and averages of the Z ceramic voltage at each XY location, which not only slows down the scan, but also increases the signal-to-noise ratio for higher-frequency interferences.

Other options are available in the topographic scan mode. The most notable is the ability to digitize an additional channel at each XY location, which is typically used to record a simultaneous barrier-height image. This is done by modulating the tip at a small amplitude in Z at a frequency above the feedback band width. The modulations induced on the current (or on the log of the current) are then detected at that frequency using a lock-in amplifier. The output of the lock-in is proportional to the barrier height and can be conveniently digitized through the other ADC.

Current-Imaging Mode

The other method for extracting topographical information from an STM is by using the current-imaging or "fast-scan" mode. In this method, the tip is scanned across the sample at a high enough rate relative to the feedback band width that only the average tip-sample separation can be maintained. Higher-frequency variations in the surface topography are manifest as fluctuations in the tunneling current. The advantages of this form of imaging are related to the speed. The data in this case are coming in at a higher frequency and are therefore less affected by the vibrational noise spectrum, which tends to fall off as the inverse of frequency. Also, thermal drift effects are mitigated. The reason that this higher scan speed and data rate cannot in general be supported in the constant

current mode is that the feedback band width that would be required would send the system into oscillation.

Our fast-scan images are performed under computer control in much the same way as the constant-current imaging. The major difference is that instead of digitizing the Z ceramic voltage at each XY coordinate, the tunneling current is digitized. Several other differences also exist. In order to speed up the scan rate, the program was written as an assembly language subroutine which is called from a FORTRAN shell for ease of input and output. We have written two different versions—one plots the image on the high resolution graphics monitor as it is being acquired, while the other acquires an entire image before plotting. In either case, the achievable refresh rate for continuous scanning of a 128×128 point image is about 0.3 Hz, with the time almost equally divided between scanning and plotting. The plotting for fast scans is done using a gray scale representation where the gray tone is related linearly to the current amplitude at that XY position. This program is used in an iterative mode where the user watches the continually repeating scans and can then choose a scan to save by using a keyboard interrupt. Storing to disk takes about 5 seconds, after which the scanning can be automatically resumed.

Current-Voltage Spectroscopy

The other STM operating mode often used is for taking current-voltage spectra at a constant tip-sample separation. In order to do this, the feedback loop is interrupted for a few milliseconds by closing the integrator gate without resetting the integrator. Then the tunneling bias voltage is ramped under computer control on one of the DAC's while the tunneling current is digitized. The tunnel bias voltage is then reset to its feedback value and the integrator gate is opened, reestablishing feedback. Typically, a few hundred such current-voltage spectra are averaged to increase the signal to noise. The duty cycle is usually around 100 ms, so each averaged I-V scan takes about one minute. During this time the tip will typically have drifted 0.2 to 0.5 nm across the surface, which is enough

so that the *I-V* spectra are not expected to be site-specific on an atomic level. It is also possible to measure individual *I-V* spectra at regular intervals during a scan and correlate the *I-V* characteristics with the scan in that way. This has only recently been implemented in our instrument, and none of that kind of data is presented here.

Other types of experiments are conveniently implemented, often with additions only to the microprocessor software. For example, separation *versus* voltage spectra can be recorded by changing the voltage under computer control while maintaining feedback and a constant current. The Z ceramic voltage is digitized and stored as a function of feedback voltage. We have also implemented an alternate bias fast scan, which allows scanning the surface in the current imaging mode sequentially at four different bias voltages. This is used for comparing bias-dependent topographies of the same area. The microprocessor control of the STM allows great flexibility in the possible combinations of scans and spectroscopy along with convenience and efficiency of operation.

Image Production

In addition to the real-time graphics displays incorporated in the topographic and spectroscopic scan routines, we have developed a versatile plotting package for data processing and display on the graphics monitor. Line plots of X *versus* Y+Z or gray scale plots of Z color intensity *versus* X and Y can be produced for either type of topographic scan. Constant-slope background subtraction and weighted iterative smoothing of the data provide limited image processing. A two-dimensional Fourier transform routine is also available. For examining specific features in the data, a line-cut routine is provided, which extracts the magnitude of the Z variable along a line of any orientation in the XY plane.

Sample Preparation Facilities

As mentioned previously, the STM we have built is housed in a UHV chamber. This is not a fundamental requirement for the practice of STM itself, as STM imaging has been demonstrated with the tip and sample in air, as well as submersed in hydrocarbon liquids and gels, cryogenic liquids, water, and even ionic solutions. Rather, the UHV environment is required for the preparation and maintenance of samples free from contaminants that can complicate the data interpretation. For versatility, we have designed an STM with sample and tip transfer capabilities. The entire vacuum system is schematically illustrated in Fig. 10. The system is comprised of two individually pumped UHV chambers separated by a gate valve. One chamber houses the STM itself; the other is for UHV sample preparation. On the opposite side of the sample preparation chamber from the STM chamber, there is another gate valve that is connected to a separately pumped high-vacuum load lock. Samples and tips can be introduced into the load lock, pumped down to 10^{-7} torr in a couple of hours, and then introduced to the sample preparation chamber or on through to the STM chamber. This is done using a long-stroke translator which extends from the load lock through the sample preparation chamber and on into the STM chamber. The samples or tips are removed from this long-stroke translator in the STM or sample preparation chambers (using bellows-sealed wobble sticks), and placed on auxiliary manipulators, sample preparation stations, sample or tip holder racks, or onto the STM itself. Thus, new samples and tips can be introduced into the UHV STM environment in a matter of a few hours. The sample preparation chamber currently houses a heating stage and an ion sputter gun for sample cleaning, as well as a small residual gas analyzer, but has room for expansion for a gas-dosing system and other standard surface analytical tools such as low-energy electron diffraction and Auger electron spectroscopy.

Tips

One of the most important parameters in the definition of surface features is the nature of the tunneling tip. Unfortunately, this is still a very poorly understood aspect of STM. The earliest STM tips were prepared by mechanically sharpening a point on the end of a wire.[3] Tips prepared in this fashion are capable of achieving atomic-scale resolution. Clearly, the macroscopically prepared tip is not smoothly tapered down to a single atom. Instead, it is postulated that microtips are formed in the grinding process that extend out from the rather large overall tip radius. Since tunneling is so exquisitely sensitive to separation, only the longest microtip contributes to the measured current.

More recently, it has become common to prepare tips by electrochemical-etching processes as is typically done for field ion microscopy. The best overall tip radius that can be achieved by electrochemical etching is in the 10 nm to 100 nm range. This is still not sufficient for atomically resolved imaging, so again a microtip mechanism is presumed. Some investigators have attempted to correlate the microstructure of the tip as measured by field ion microscopy with the achievable resolution in STM.[15] For measurements of larger-scale features, the macroscopic tip radius becomes much more important since this will define the minimum local concave radius that can be measured. The electronic band structure or density of states of the tip is also important, especially in spectroscopy, where any electronic effect seen is a convolution of tip and sample density of states. The wave function symmetry at the very apex of the tip may also have the effect of selecting which symmetry states are more favored for tunneling.

We have typically made our tips by electrochemical etching of tungsten wire. The etching solution is 2 M NaOH. For the AC etch method, the wire is partially submerged in the solution, and a 6.3 V, 60 Hz AC bias is applied. Etching is allowed to continue until the wire beneath the surface is gone and you are left with a tip poised over the surface of the electrolyte. Tip radii of ~ 300 nm can be obtained in this way. The other etching method uses a DC potential of 10 to 15 V on the tip. In this method, the height of

the wire in the solution must be continuously adjusted to keep the meniscus at a constant position on the wire as the wire etches away. The wire will be observed to thin just below the surface of the solution as the etching proceeds. Eventually, this thin section of wire will break and the rest will drop away. This break causes a sudden decrease in electrochemical current (because of the smaller remaining electrode size), which is detected and used to quickly turn off the etching voltage in a few milliseconds or less to avoid blunting the remaining tip. Tips formed in this more tedious fashion have a smaller cone angle and can have tip diameters as small as 10 nm.

These electrochemical etching methods are known to leave a rather thick surface oxide layer on the tip, which is thought to interfere with the tunneling process. Although the electrochemically etched tips have often been used successfully for atomic-resolution imaging without further preparation, it has been found that a higher imaging success rate can be achieved by heating the tips to about 800° C in vacuum, which is enough to remove most of the surface oxide. After this vacuum bake, the tips can be transferred in air to the STM without reforming a significant oxide layer. Unbaked tips have been used in all our studies, but other *in situ* tip cleaning procedures have been attempted. One such method is to touch the tip to the surface lightly, to try to break the surface oxide or reform the tip. Another is to field-emit from or to the tip at high currents, thereby bombarding the tip with high energy particles, providing a strong field for field desorption, and perhaps also increasing the temperature of the tip through *IR* heating.

For some of our studies we have also used electrochemically etched gold tips. This was done in an effort to circumvent the oxide problems as well as to provide an opportunity for comparison between the topographic images and especially the spectroscopic results obtained with a different tip material. The gold tips were made in the same way as the tungsten tips except that the electrolyte was 50% concentrated HCl, 25% ethanol, and 25% glycerin.

Conclusion

The instrumental challenges in scanning tunneling microscopy are great. Careful thought to the design of the vibration-isolation system, and the rigidity of the tip scanner and coarse-approach mechanism is essential to ensure the necessary attenuation of environmental vibrational excitations. Increasing the rigidity of the microscope structure is especially important, since this gives the most reliable and effective noise rejection. In addition, a rigid microscope structure can support a higher feedback band width and a faster scan speed. Including the required stiffness in the design of the scanning and coarse approach mechanisms can be complicated by other constraints such as, in our case, *in vacuo* tip and sample transfer and lateral sample translation. Miniaturization is usually the best approach to increasing the microscope stability; however, often this has to be traded off against larger scan ranges.

The electronic feedback control system is the other important factor for reliable microscope operation. Adequate gain and band width for accurate surface tracking should be designed within the constraint of avoiding oscillations and tip-sample contact. Also, for versatility and convenience in operation, microprocessor control of scanning and of data acquisition with real-time graphics display is invaluable. Taking these design issues into consideration, a reliable and versatile STM can be constructed, which will very effectively meet the needs of most applications.

References

1. R. Young, J. Ward, F. Scire, *Rev. of Sci. Instrum.* **43**(7), 999–1011 (1972).
2. G. Binnig, H. Rohrer, Ch. Gerber, *Appl. Phys. Lett.* **40**(2), 178–80 (1982).
3. G. Binnig, H. Rohrer, *Surf. Sci.* **126**, 236–44 (1983).
4. Y. Kuk, P. J. Silverman, *Rev. Sci. Instr.* **60**(2), 165–180 (1989).
5. D. W. Pohl. *IBM J. Res. Develop.* **30**(4), 417–27 (1986).
6. D. Kleppner, R. J. Kolenkow, *An Introduction to Mechanics*, McGraw Hill, New York (1973), *p.* 409*ff.*
7. S. Park, C. F. Quate, *Rev. of Sci. Instrum.* **58**(11), 2004–9 (1987).
8. D. P. DiLella, J. H. Wandass, R. J. Colton, C. R. K. Marrian, *Rev. of Sci. Instrum.* **60**(6), 997–1002 (1989).
9. J. P. den Hartog, *Mechanical Vibrations*, Dover, NY (1934).
10. Ch. Gerber, G. Binnig, H. Fuchs, O. Marti, H. Rohrer, *Rev. of Sci. Instrum.* **57**(2), 221–4 (1986).
11. M. Okano, K. Kajimura, S. Wakiyama, F. Sakai, W. Mizutani, M. Ono, *J. Vac. Sci. Technol.* **A 5**(6), 3313–20 (1987).
12. G. Binnig, D. P. E. Smith, *Rev. of Sci. Instrum.* **57**(8), 1688–9 (1986).
13. J. Jahanmir, P. E. West, T. N. Rhodin, *Appl. Phys. Lett.* **52**(24), 2086–8 (1988).
14. H. J. Mamin, E. Ganz, D. W. Abraham, R. E. Thomson, J. Clarke, *Phys. Rev.* **B 34**(12), 9015–8 (1986).
15. Y. Kuk, P. J. Silverman, *Appl. Phys. Lett.* **48**(23), 1597–9 (1986)

Figure 1

A simplified one-dimensional model of the vibration response of a scanning tunneling microscope to its support system. For small-scale excursions, both the tip-sample coupling and the motion of the STM relative to its support can be modeled as damped harmonic oscillators, here illustrated with spring constants k_t and k_s, and viscous damping factors b_t and b_s, respectively. The motion of the tip-structure, STM body, and supporting structure in an inertial frame are given by x_t, x_s, and x_0, respectively.

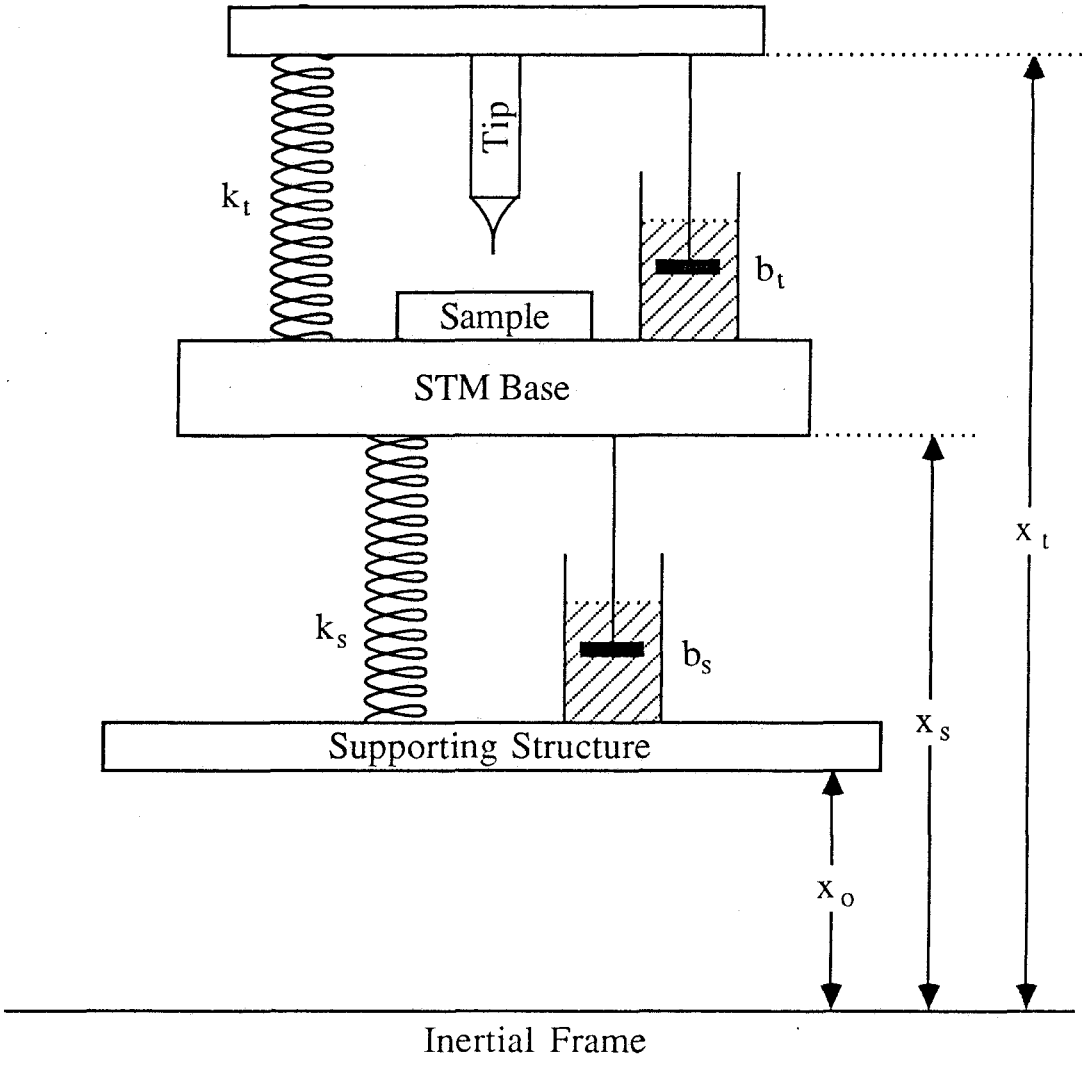
Tip
k_t
b_t
Sample
STM Base
k_s
b_s
Supporting Structure
x_t
x_s
x_o
Inertial Frame

Figure 2

Transfer function for a damped harmonic oscillator with various mechanical quality factors, Q, plotted as the ratio of the transmitted to external amplitudes. The frequency axis is scaled by the oscillator resonant frequency. Q is inversely proportional to the damping factor b, $Q = \frac{\sqrt{km}}{b}$.

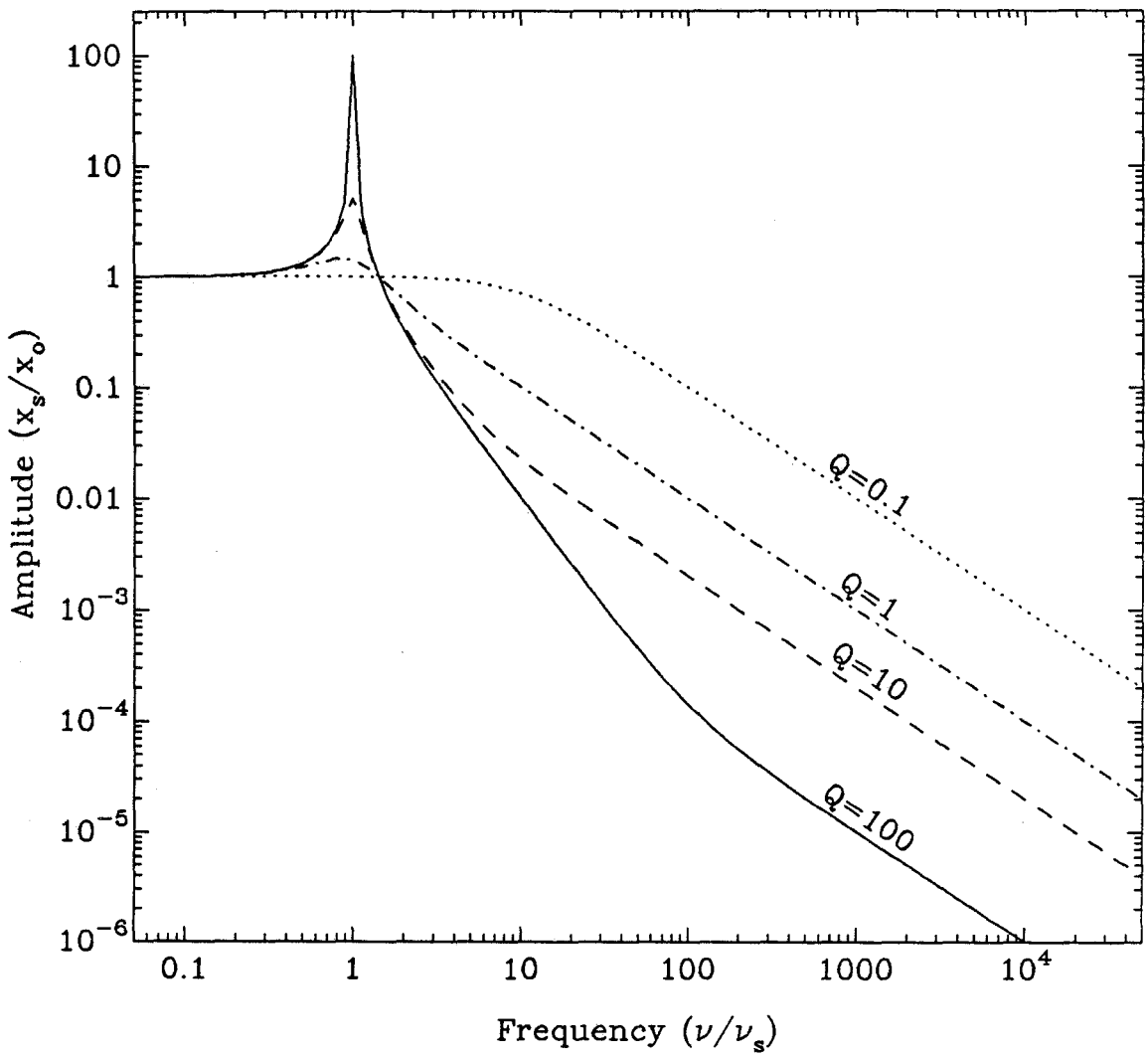
100
10
1
0.1
0.01
10^{-3}
10^{-4}
10^{-5}
10^{-6}
Amplitude (x_s/x_o)
0.1
1
10
100
1000
10^4
Frequency (ν/ν_s)
Q=0.1
Q=1
Q=10
Q=100

Figure 3

Comparison of a single stage and a dual stage vibration isolation system where the total extension length is fixed. The frequency axis is normalized to the resonant frequency of the single stage system. The dual stages are assumed to be decoupled, and a mechanical Q of 5 is used for all stages.

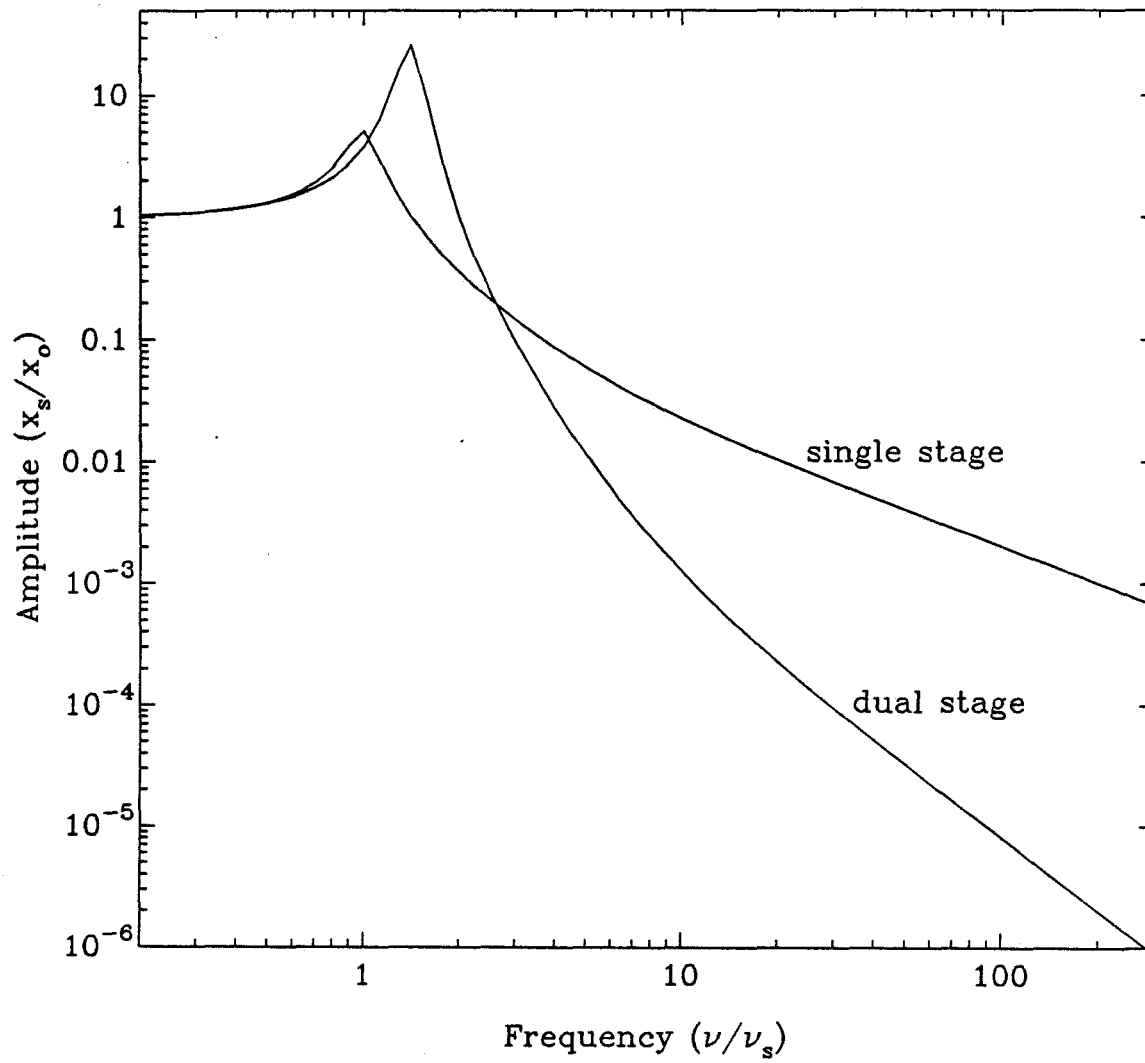
10
1
0.1
0.01
10^{-3}
10^{-4}
10^{-5}
10^{-6}
Amplitude (x_s/x_o)
1
10
100
Frequency (ν/ν_s)
single stage
dual stage

Figure 4

Stiffness function for a simple harmonic oscillator with varying quality factors. The frequency axis is scaled by the oscillator resonance frequency. The amplitude function is the relative motion between the mass and the support relative to the absolute motion of the support in an inertial frame.

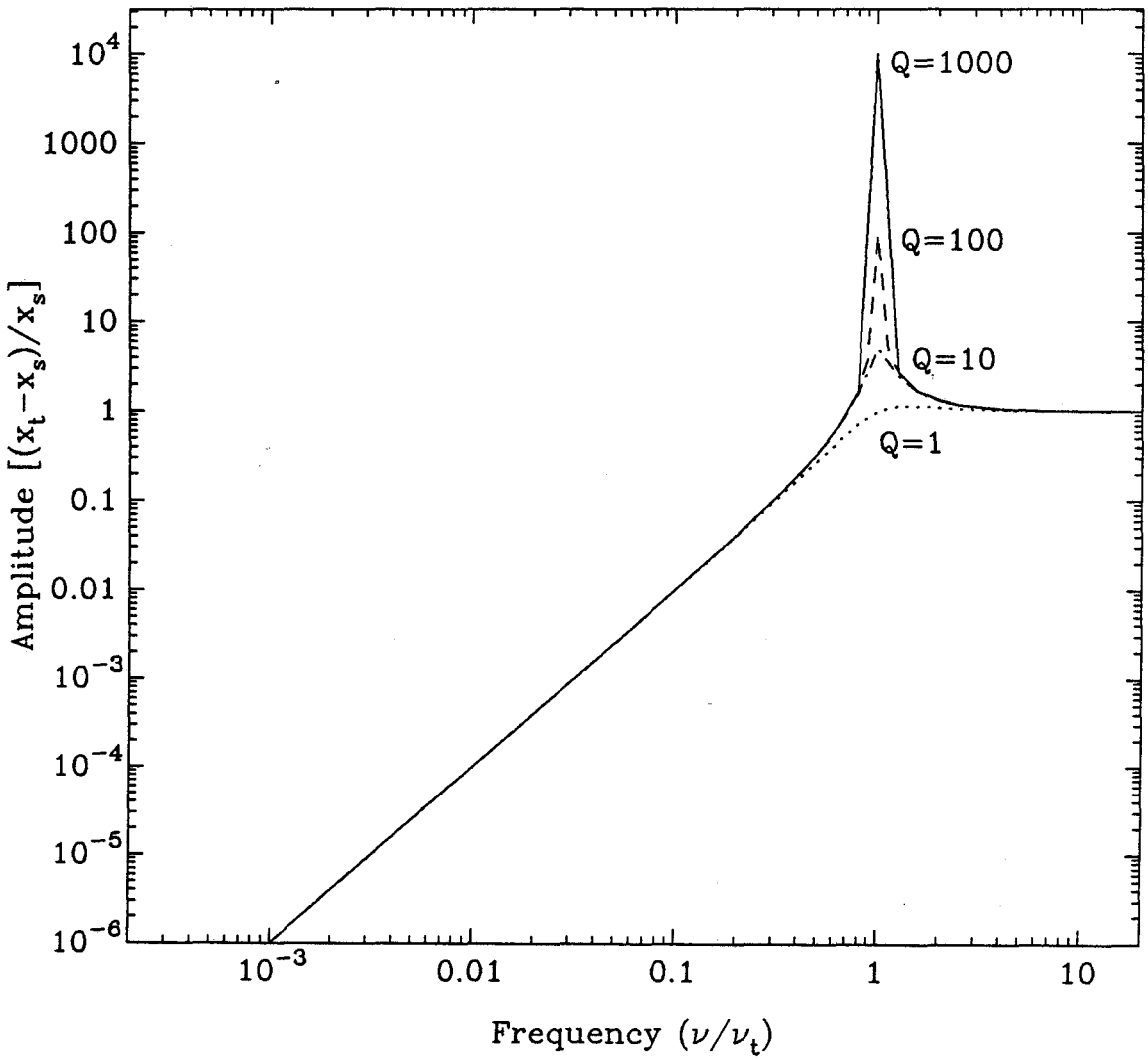
Amplitude $[(x_t - x_s)/x_s]$
10^4
1000
100
10
1
0.1
0.01
10^{-3}
10^{-4}
10^{-5}
10^{-6}
Q=1000
Q=100
Q=10
Q=1
10^{-3}
0.01
0.1
1
10
Frequency (ν/ν_t)

Figure 5

Vibrational filtering function $T \times S$ for an STM system. Also plotted are the individual T and S from which the composite is derived. The vibration-isolation system has a single stage with a 1 Hz resonance and a Q_s of 5, and the first resonance of the mechanical coupling between tip and sample is at 10 kHz with a Q_t of 100.

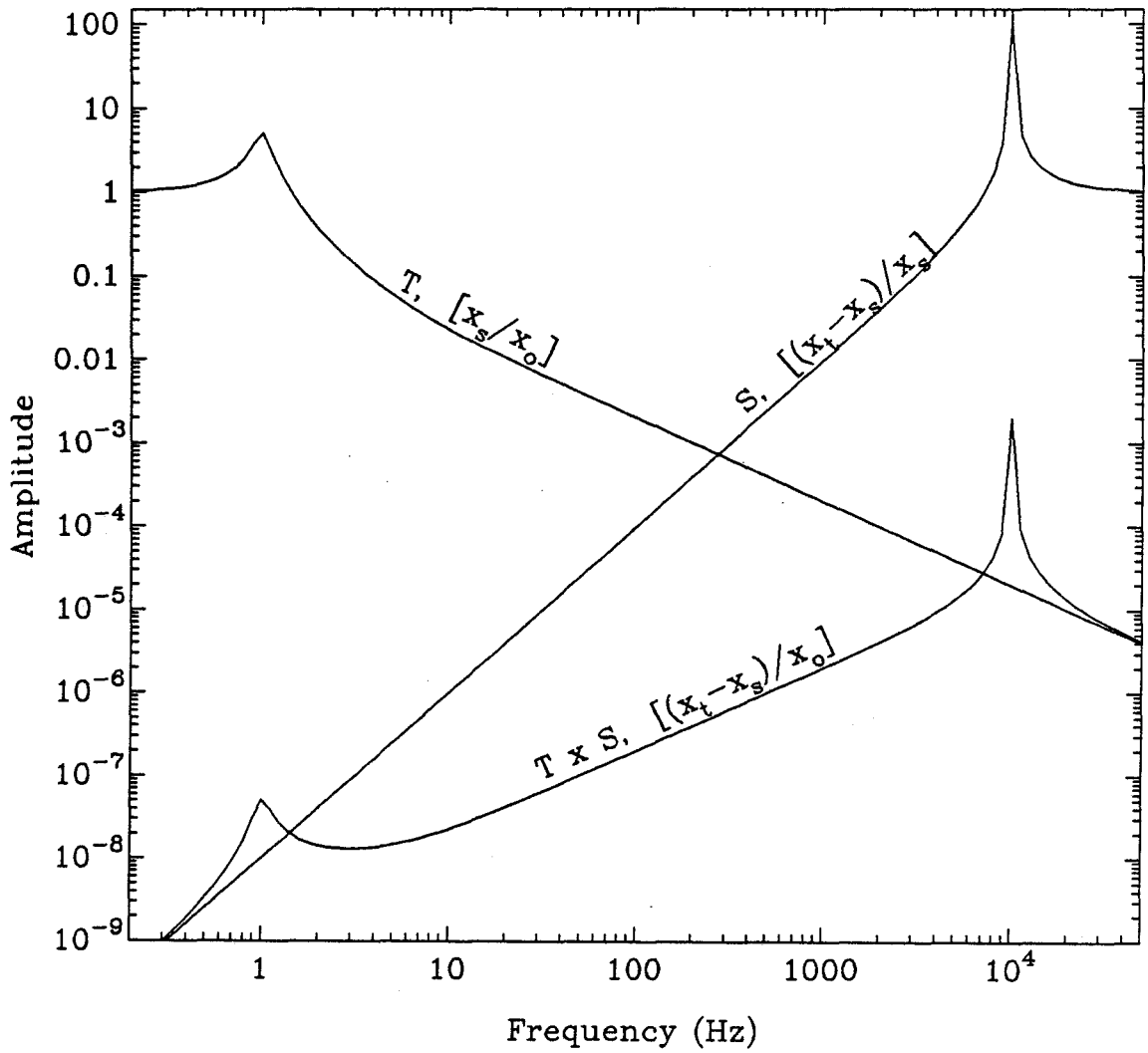
100
10
1
0.1
0.01
10^{-3}
10^{-4}
10^{-5}
10^{-6}
10^{-7}
10^{-8}
10^{-9}
Amplitude
1
10
100
1000
10^4
Frequency (Hz)
T, $[x_s/x_o]$
S, $[(x_t-x_s)/x_s]$
T x S, $[(x_t-x_s)/x_o]$

Figure 6

Schematic representation of the vibration-isolation system used in our STM. Two stages of spring suspension supports are incorporated, as well as an isolation platform made from five stacked stainless steel plates separated by Viton rubber spacers. The motion of the spring stages is damped, using magnetic eddy currents in copper blocks. Also, the suspension points of the springs are attached, using Viton rubber O-rings to damp the spring resonances and decouple them from the stages.

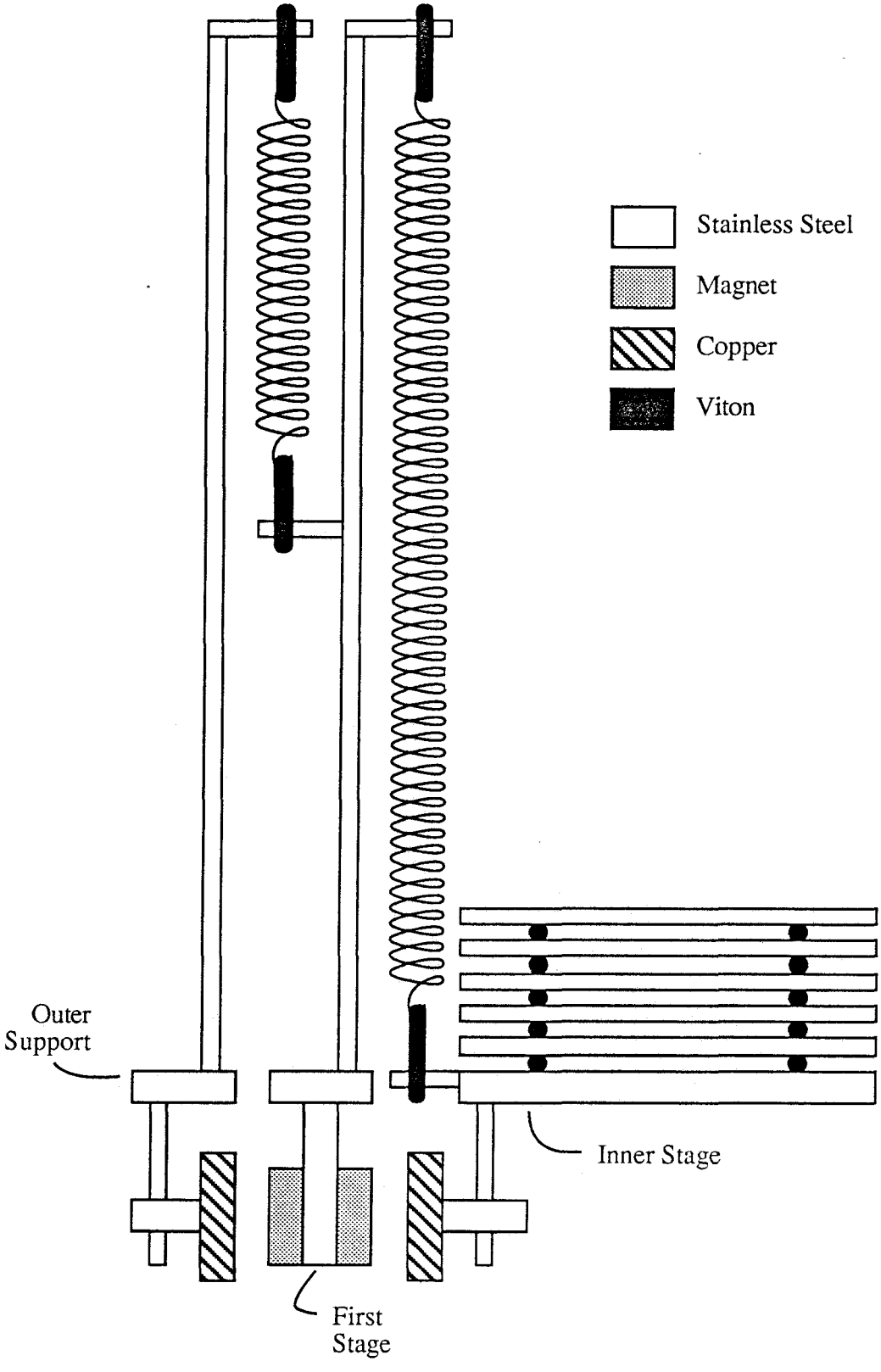
Stainless Steel
Magnet
Copper
Viton
Outer
Support
Inner Stage
First
Stage

Figure 7

Top and side views of the high-resolution XYZ translator and the coarse approach mechanism (a piezoceramic louse) used in our STM. This is basically the "pocket" STM design of Gerber *et al.* [Ref. 10, *p.* 44].

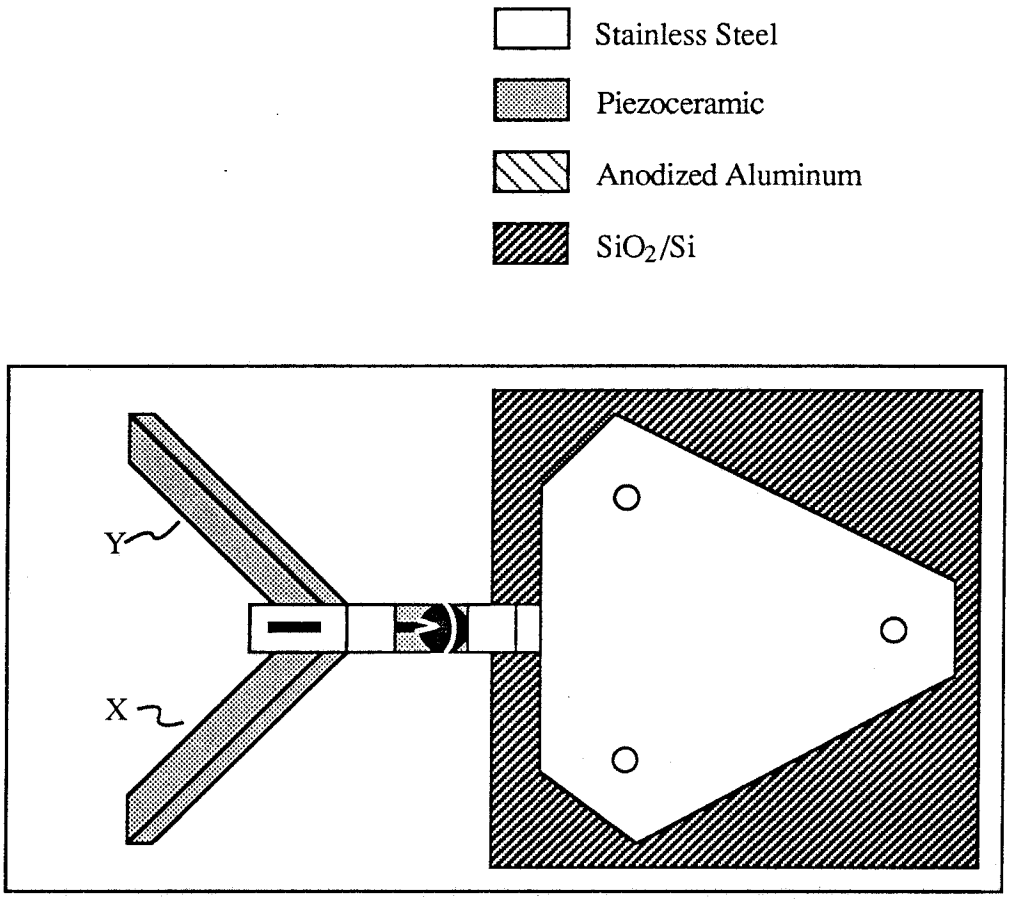
Stainless Steel
Piezoceramic
Anodized Aluminum
SiO_2/Si
Y
X

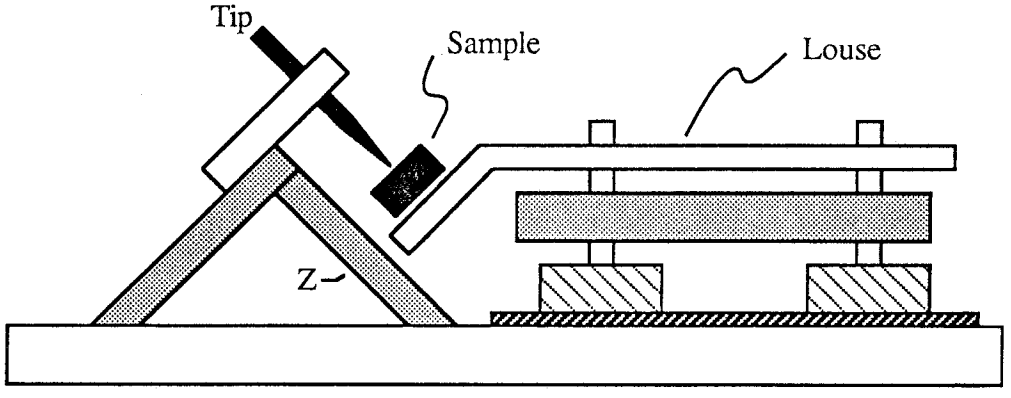
Tip
Sample
Louse
Z

Figure 8

Block diagram of the feedback control electronics. The specific model numbers of the important components are given in the text.

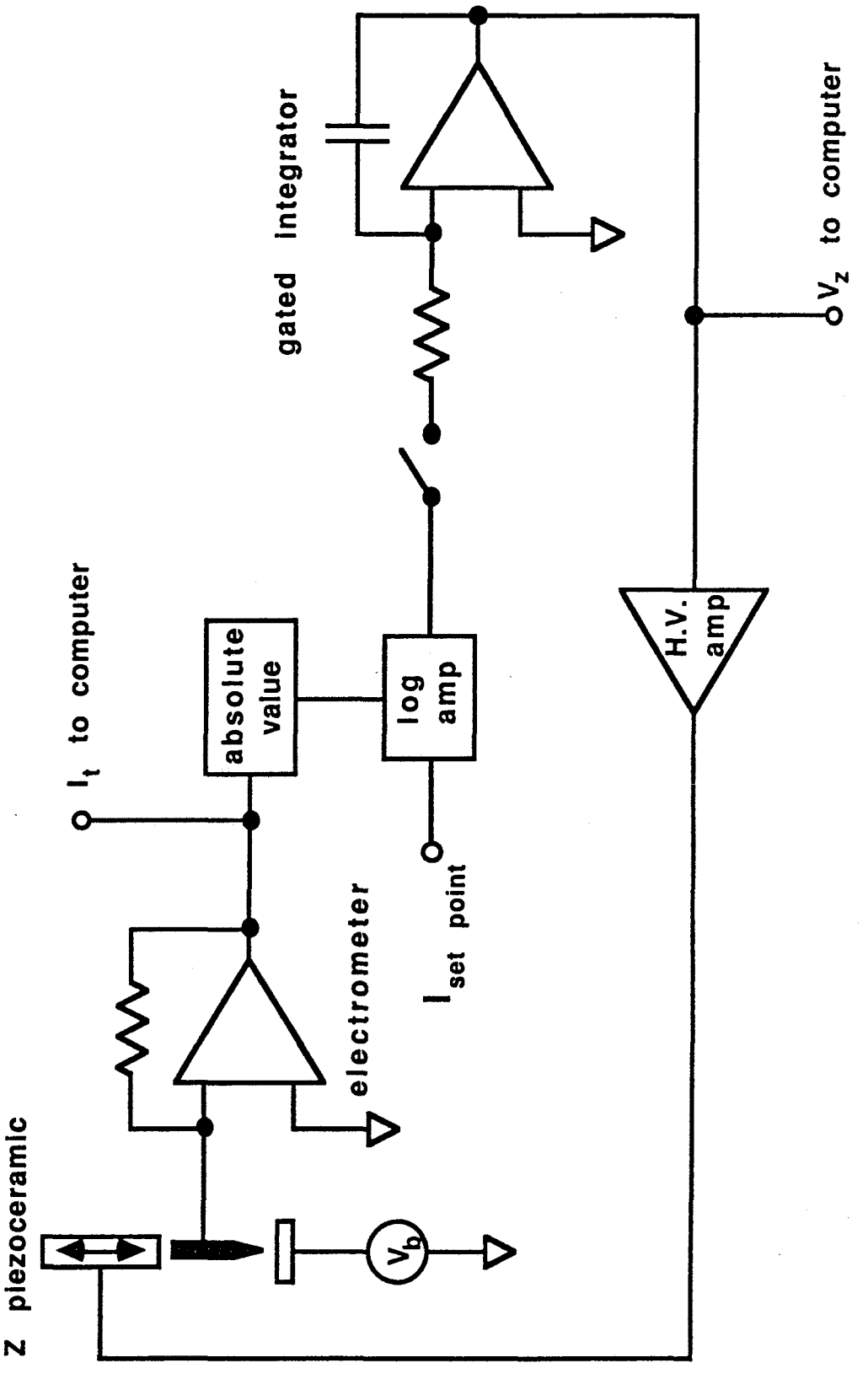
Z piezoceramic
V_b
electrometer
$I_{set\ point}$
log amp
absolute value
I_t to computer
H.V. amp
gated integrator
V_z to computer

Figure 9

Block diagram of microprocessor-based control system for STM. Most microscope functions can be controlled directly from the microprocessor through the analog and digital interfaces. The video graphics monitor provides important real-time display

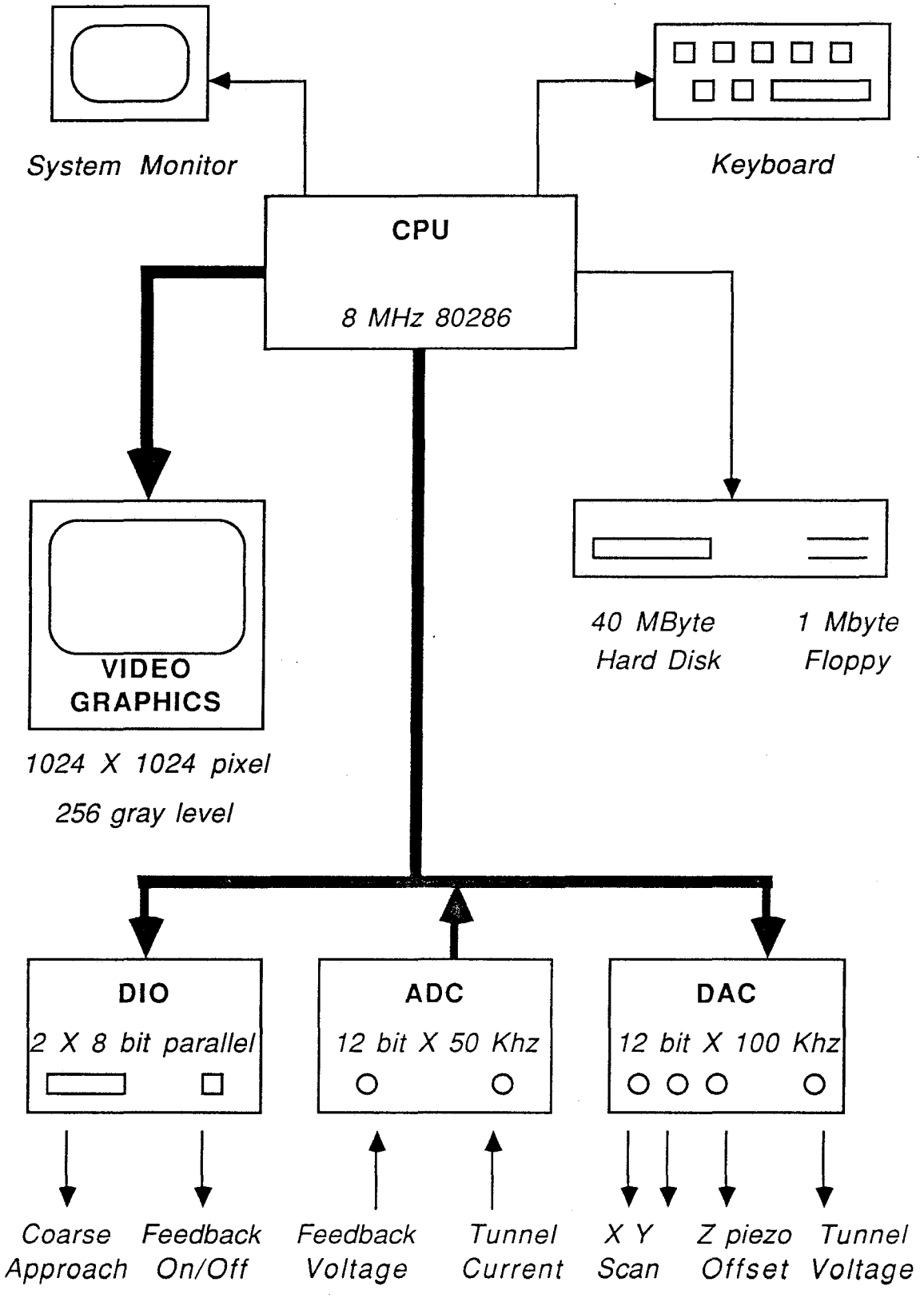

(figure from Michael Weimer)

Figure 10

Schematic representation of the UHV system, including the STM chamber, sample preparation chamber, and vacuum load lock with long stroke translator. Base pressures of 5×10^{-11} torr are readily achieved in the STM chamber. This is probably due in part to the infrequency with which it must be opened, since tip and sample transfers through the vacuum load lock are routine.

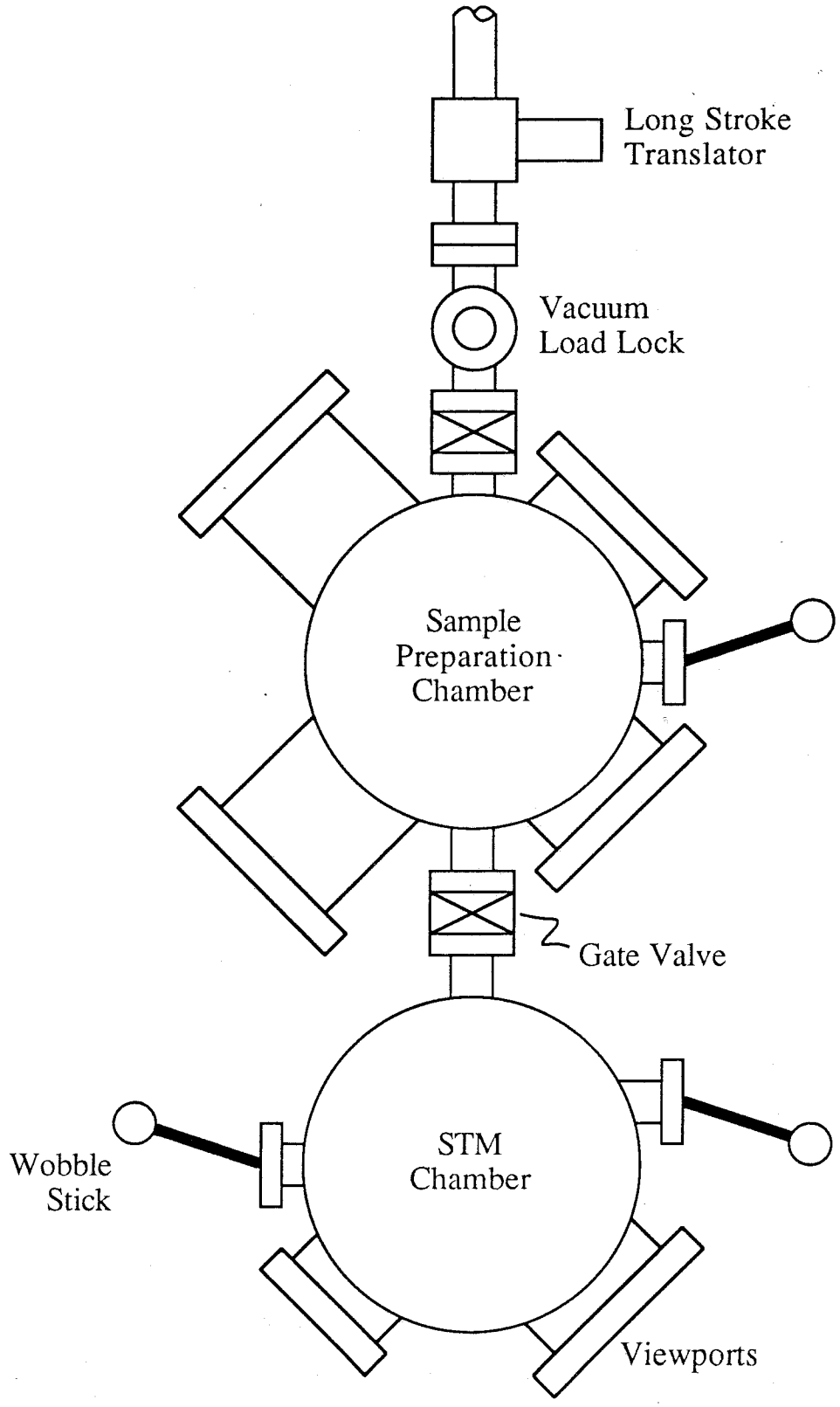
Long Stroke
Translator
Vacuum
Load Lock
Sample
Preparation
Chamber
Gate Valve
STM
Chamber
Wobble
Stick
Viewports

Chapter 3

SURFACE MORPHOLOGY OF MOLYBDENUM DISULFIDE BY SCANNING TUNNELING MICROSCOPY§

Introduction

Since its introduction as a new probe for surface analysis,[1] the scanning tunneling microscope (STM) has been used to examine the geometric and electronic structures of a variety of metal and semiconductor samples.[2] Most of the initial studies, including all of the early atomic-resolution results, were obtained on elemental surfaces. More recently, compound surfaces such as GaAs and several of the layered transition metal dichalcogenides have been studied with the STM and have yielded their surface structure with atomic resolution. Within the past year or two, high-resolution images of atomic and molecular adsorbates on various substrates have also been increasingly reported.

A question that arises in studies of multicomponent samples is the extent to which the STM is able to distinguish between the different atomic species. This is a particularly challenging problem in STM, since the interaction of the probe tip and the surface is through a tunneling current that is strongly weighted to the most weakly bound electrons. The characteristic energies of the core level electrons, for example, are completely inaccessible. The most dramatic success in atom identification with the STM is found in the work of Feenstra *et al.*[3] on the GaAs (110) surface. In this study, either the Ga or As atoms were selectively imaged by a choice of the tunnel bias voltage. So far this is the only case where such selectivity has been achieved. In an effort to add to our understanding of the capability of the STM for establishing chemical identity, we have undertaken a vacuum STM study of MoS_2.

Motivation for Studying Molybdenum Disulfide

For several reasons molybdenum disulfide (MoS_2) is a good compound on which to study the chemical identity capability of STM. An atomically flat and clean surface of MoS_2 is easily prepared, minimizing the problems of sample preparation. The surface is relatively inert chemically, which means that the prepared surface will not be quickly

contaminated by residual gasses in the vacuum environment. Both the sulfur and the molybdenum atomic species are available for tunneling from the cleavage surface, so differences in their topographic or electronic structure can be studied. Lastly, MoS_2 is a semiconductor, so the electronic states are expected to be more localized over specific atoms than, for example, in a metal.

The first step is to be able to resolve the two atomic sites within the crystal lattice. Specific properties associated with the two sites can then be addressed. These differences might manifest themselves as differences in the topographical images measured at opposite tunnel bias, because of a difference in the spatial distribution of the filled and empty states. Alternatively, a measurement of the wave function decay lengths (*i. e.*, tunneling barrier heights) over the two sites could provide an additional contrast mechanism. In either case, the experimental results will need to be correlated with theoretical studies that predict the state distribution or the wave function decay lengths over the atomic sites.

The corrugation amplitude measured by the STM on atomically resolved surface planes is also of interest. MoS_2 is a layered compound, similar in its mechanical properties to graphite. STM imaging mechanisms on graphite have been the subject of some debate, in part because of the anomalously large atomic corrugation amplitudes (up to 7 nm) that have been observed on this surface.[4] Some of the explanations for this effect are based on the proposal that tip-sample interaction forces, in conjunction with the mechanical anisotropy of the graphite surface with its strong intraplanar bonding but relatively weak interplanar bonding, produce large elastic deformations of the graphite surface during scanning.[5] Other proposals are based solely on the electronic properties of graphite.[6] MoS_2 is very similar to graphite in its macroscopic mechanical properties. Its electronic properties, however, are substantially different. A comparison of STM

imaging behavior of these two compounds could therefore provide some new information on this issue.

Physical Properties of MoS_2

Molybdenum disulfide is the most well known of the layered transition-metal dichalcogenides (LTMD). These compounds have been much studied because of their interesting electronic and structural properties.[7] Most of the group VI LTMD compounds are found to be semiconducting because of the nature of the bonding within the crystals. In MoS_2, for example, the S is formally of –2 charge and the Mo is in a +4 state. The two remaining outer-shell electrons in Mo lie in a band made up of the Mo $4d_{z^2}$ orbital, which is therefore fully occupied and non-bonding. The lowest unoccupied states seem to be comprised predominantly of Mo $4d_{(x^2-y^2)}$ and $4d_{xy}$ orbitals.[7] The direct band gap in MoS_2 is about 1.7 eV, and the indirect band gap has been measured at 1.2 eV.[8]

The crystal structure of MoS_2 is also well known, having first been studied by x-ray diffraction in the 1920's.[9] The basic structural unit is a sandwich of S–Mo–S planes. The S atoms are in a close-packed arrangement within their planes, with the second S layer eclipsed by the first. The Mo layer is located halfway between these two planes, with each Mo atom bonding covalently to the three sulfur atoms above and the three below with trigonal prismatic coordination (Fig. 1). The S–S distance within the plane is 0.316 nm and the distance between the S and Mo planes is 0.149 nm. The S–Mo bond length is 0.241 nm.

The crystals themselves are made up of repeating stacks of these sandwich units. The 2*H* type studied here is hexagonal and has two S–Mo–S sandwich layers per unit cell. The relative symmetry of the Mo within the S hexagon is reversed from sandwich to sandwich, and both the S and the Mo in each subsequent sandwich are eclipsed by the Mo and S, respectively, in the sandwich above them. The hollow sites extend through the crystal. The sulfur planes between sandwiches are separated by 0.317 nm. At this

distance, the bonding between sandwiches is chiefly a van der Waals interaction. This weak bonding between S–Mo–S sandwich layers is thought to give rise to the excellent lubricative properties of MoS_2. The electrical resistivity is also about 10^3 times higher perpendicular to these planes than it is parallel to them.

MoS_2 is easily cleaved at the van der Waals plane, by using a sharp blade or by simply peeling off a few surface layers with adhesive tape. The surface so exposed is unreconstructed from the bulk structure and is chemically inert because of the stable covalent bonding, which utilizes all of the valence electrons with the exception of those in the fully occupied Mo non-bonding d_{z^2} orbitals. An air-stable basal surface is therefore easily prepared. The STM experiments are nevertheless best done in UHV in order to avoid complications of physisorbed surface contaminants such as hydrocarbons and water vapor. Insertion of air-cleaved surfaces into UHV with no further preparation has been shown to yield ordered LEED patterns and very little carbon contamination in Auger measurements, thus indicating an easily desorbed contamination layer.[10] Completely clean surfaces as determined by x-ray photoelectron spectroscopy can be regenerated by heating in vacuum for 30 minutes at 450 °C.

STM Studies of MoS_2

Tunneling microscope studies of the MoS_2 surface have also been reported by other workers. Stupian and Leung[11] have presented atomically resolved current-contrast images of MoS_2. In their work, they found that stable tunneling current and atomic-resolution images could only be obtained at negative sample bias. The peaks which they observed in their images were attributed to tunneling out of the Mo $4d_{z^2}$ orbitals. Sarid *et al.*[12] have demonstrated that atomic-resolution current images can be obtained in either tunnel bias polarity. In the present work, a more thorough investigation of the nanometer scale morphology of the MoS_2 surface is described, and atomic-resolution constant

current as well as current-imaging mode topographs are presented, which show the two atomic sites within the crystal lattice.

Experimental

Instrumentation

The scanning tunneling microscope used in this study is described in detail in Chapter 2. Briefly, the STM is housed in a two-chamber ultrahigh vacuum system with an additional vacuum load lock for sample introduction. Samples are transferred initially into a sample preparation chamber, and from there they may be moved on into the STM chamber. The tunneling microscope is based on the "pocket" STM design,[13] with the addition of two stages of spring-suspension vibration isolation. Constant tunneling current is maintained by means of an analog feedback circuit, which includes a commercial electrometer, a logarithmic amplifier to linearize the response, a gated integrator for band width control, and a ±150 V piezoceramic driver. Scanning, data acquisition, and image display for both the constant-current and current-imaging modes are controlled by an Intel 80286 based microprocessor.

Sample Preparation

The MoS_2 samples used in this study are of natural origin. Sample A was shown to be of the more abundant *2H* crystal type by x-ray powder diffraction. The sign of the thermopower voltage indicated *n*-type doping for this sample. This was confirmed by a Hall coefficient measurement, from which were also derived a carrier concentration of 8×10^{16} cm^{-3}, a resistivity of 2.91 Ω-cm, and a mobility of 28 $cm^2V^{-1}s^{-1}$. Sample B came from a separate source, but was also measured to be *n*-type with a carrier concentration of 6×10^{17} cm^{-3}, a resistivity of 0.473 Ω-cm, and a mobility of 24 $cm^2V^{-1}s^{-1}$. Note, however, that these measurements are bulk properties and do not measure local deviations.

The samples were mounted on our stainless steel, stub sample mounts with molten indium metal or silver paint. In some cases, electrical contact was extended directly to the top plane of the sample using silver paint. In our experience, this had little effect on the characteristics of the current conduction, and stable tunneling currents could be obtained either way.

The samples were cleaved to expose a fresh surface before imaging. When imaging in vacuum, the samples were cleaved immediately before insertion. In some cases, this was done in a nitrogen flow out of the sample load lock. No systematic difference in the imaging characteristics was observed for these different preparation methods, nor even for experiments in which the samples were cleaved in vacuum or baked in vacuum for a half hour at 450 °C to insure removal of surface contaminants.

Tip Preparation

Tips for these studies were prepared from two different metals, both with similar results. Tungsten tips were electrochemically etched in 2 M NaOH, using either the DC drop-off method or the AC method. Gold tips were prepared by AC etching in a solution of 25% glycerin, 25% ethanol and 50% concentrated HCl. After etching, the tips were thoroughly rinsed, first with deionized water and then with ethanol.

Most of the tips were used without further preparation. With some of the Au tips an attempt was made to ensure cleanliness by field emitting onto a Au foil in vacuum. While it is clear that this treatment induces changes in the microstructure of the tip, there was no evidence that the overall imaging ability, or tunneling-current stability was consistently improved. Some of the W tips were also subjected to the same field-emission procedures. Electrochemical etching of W is known to produce a thick surface oxide layer, so one might expect a more dramatic improvement in tip performance; however, the results were similarly inconclusive. Other attempts to improve the performance of the tips included lightly touching them to the surface, presumably either physically knocking

off surface contaminants or reforming the microtip by cold welding and plastic deformation. "Light" surface crashes can be achieved either by opening up the feedback bandwidth, thus inducing small oscillations in the Z ceramic feedback response, or by scanning across the surface at a rate at which the feedback circuit cannot completely compensate for the changes in topography.

Results and Discussion

Contaminated Tip and Surface

In many cases, approach of the STM tip to the surface gave indications of a contaminated tip or sample. This is evidenced by a very small sensitivity of the tunneling current to the tip-sample spacing. In these cases, instead of the expected order-of-magnitude change in current with a 0.2 nm change in separation, a tip displacement of as much as 100 nm was necessary. These conditions were perhaps more frequent in air than in vacuum, but were often seen in either environment, especially on first approach of tip to sample. Under these conditions, no measurements of the surface topography is possible because the motion of the tip normal to the surface under feedback control is at best weakly correlated to the height of the surface. The tip must then be "cleaned" by one of the methods outlined above, or a different area of the surface must be found for the investigations.

Rough Surface Morphology

Once the tip is cleaned and a successful approach is made, a rough and irregular surface topography is often found. This may be due to imperfect cleaves or to imperfections in the crystals themselves, including possible inclusions of other materials in these samples. On the other hand, in some cases it may be due to inadvertent tip-surface contact and deformation of the surface, especially upon approach, because of a jerky motion of the coarse approach mechanism (a piezoceramic louse). There is also some

evidence that at times these rough areas may be caused by either too high or too low a tunnel bias voltage, or by too high a tunnel current. The high voltage may cause a chemical change because of interactions of surface species with high-energy electrons. Low voltages or high currents, on the other hand, could induce changes by *de facto* tip-sample contact as the gap spacing is reduced. High tunnel currents may also damage the surface through ohmic heating. Whatever the cause, the tunneling characteristics lack the stability in these regions for the atomic-scale surface structure to be determined. A representative topographical scan of a 180 × 180 nm area of sample A exhibiting this type of morphology is shown in Fig. 2. A flat basal plane can be seen in certain regions of the image, but a large part of the surface is very rough and is subject to tunneling instabilities.

Tunnel-Bias Dependent Topography

Scanning across the surface reveals areas where the rough topography gives way to atomically smooth planes. One such instance is illustrated in Fig. 3(a). This is a smaller area of the surface, 12 × 12 nm, taken with the same tunneling conditions, 0.6 V bias on the sample, and a feedback current set point of 2 nA. Qualitatively, the left half of the image appears similar to the rough areas in Fig. 2. On increasing the sample bias to 2.0 V, the tunneling conditions stabilize somewhat and the image appears much smoother, as shown in Fig. 3(b). The area scanned in Fig. 3(b) does not exactly coincide with that in Fig. 3(a) because of some thermal drift. However, even in the overlapping regions, some differences are seen in topography, and the relative height of some of the features is changed. This points to the importance of bias-dependent imaging in STM investigations of this surface. This can be contrasted to STM studies of metals, where the topographical images are usually independent of the tunnel-bias voltage except for a decrease in the corrugation amplitude with increasing voltage (at a constant current) that is due to the increased tip-sample separation.[14]

A more dramatic example of bias-dependent imaging is illustrated in Fig. 4. These images are of a 45 × 45 nm area of sample B, taken in air with an AC etched gold tip, and acquired sequentially within a period of 25 min. In all of the images the tunneling-current feedback set point was 1 nA. The images shown in Figs. 4(a) and 4(c) were taken at a sample bias of –0.5 V. Several double island features are seen in these images. Each island is about 2 nm in diameter and protrudes from the surface about 0.5 nm. A small shift is apparent in comparing the two images, which is due to a thermal drift of about 0.5 nm/min. The spacing between the two islands in each of the three lower clusters is about 2.5 nm, and their relative orientation is the same. Likewise, for the two upper pairs, the spacing is about 4.5 nm, and the relative orientation is the same, but is rotated from that of the three lower pairs by about 30°. One intriguing possibility is that the islands lie in preferred sites that are commensurate with the underlying crystal structure. This would imply eight lattice spacings between the nearer islands and would explain the suggestive 30° rotation and $\sqrt{3}$ relationships between the orientations and spacings of the top and bottom clusters. The two successive images that show the same differences in the relative spacings and orientations of the double islands eliminate, in this case, the possibility that these double islands are due to a double tip effect.

The image shown in Fig. 4(b) is a scan of the same area of the surface as the scans shown in Figs. 4(a) and (c), but at a sample bias of +0.5 V. This image is extremely rough, with a completely different apparent surface structure from that seen in the bracketing scans. One hint of a possible cause is the observation of a change in the Z piezoceramic voltage, corresponding to a 2–3 nm decrease in the tip-sample separation when switching from negative to positive sample bias. Of course, the change in piezoceramic voltage does not necessarily imply that the gap spacing changed by the full amount. If the tip were to come in contact with the sample, for example, some of the "distance" change would be taken up by the elastic (and possibly plastic) deformations of

the tip and sample. The 2–3 nm distance change was necessary to maintain the feedback condition of 1 nA tunneling current at the new bias voltage. This indicates a very non-linear and asymmetric current-voltage characteristic. In the topography of Fig. 4(b) then, the tip was much nearer the sample surface than in Figs. 4(a) and (c)—quite possibly even touching. If the tip and surface were indeed touching, the lateral motion of the microscopic tip across the surface might be severely restricted because of frictional interactions. Also, the surface corrugation amplitude for this tunneling polarity is about ten times greater than that seen at –0.5 V. This would be consistent with varying amounts of elastic deformation as the tip was scanned across the surface. Large-scale plastic deformations of the tip or sample that are due to any possible contact can be ruled out by a comparison of the two bracketing images.

The last scan in the series was taken at a sample bias of +1.25 V. In this case, changing the sample bias from –0.5 V in scan 4(c) to +1.25 V in scan 4(d) resulted in no measured change in the Z piezoceramic voltage beyond the uncertainties caused by noise and drift (0.3 nm). Once again, it is apparent that there is much more noise because of tunnel current instabilities than was seen at negative sample bias. In this case, however, the same features that were observed at negative bias can be discerned just barely. Apparently then, the differences seen in the topographies at the alternate sample biases are not due to tunneling from two completely different parts of the tip.

In this series of images, as in the images of Fig. 3, imaging with different tunnel bias voltages results in differences in the measured topography. This may be due partially to differences in the topography of the surface (or tip) wave functions in the different tunnel biases, but may also, in extreme cases, be due to deformations caused by tip surface contact, especially at lower gap resistance.

Mounds

Islands or mounds in a variety of sizes similar to those seen in Fig. 4 are often observed on these MoS_2 samples. Figure 5 shows three different size scans of the same region of sample A. The sample had been cleaved in air two days prior to the scans and introduced to the load lock and pumped down immediately to about 10^{-10} torr. An AC etched gold tip was used for these images, and the tunneling current feedback set point and the sample bias were 1 nA and 1.0 V, respectively. Several islands of different sizes are apparent in these images. The smallest island in the 90×90 nm scan of Fig. 5(a) is barely visible in the 360×360 nm scan of Fig. 5(c). The mounds range in size from about 4 nm to at least 15 nm. Some of the larger mounds have a diameter of up to 30 nm, but are not completely smooth and spherical and may actually be conglomerates of several smaller mounds. A clear example of this is the cluster near the top of Fig. 5(a), which appears as a single island in the larger area scans.

In trying to interpret the shape of these mounds, it is important to keep in mind that the observed features are a convolution of tip and surface structure. If, for example, one were to assume a spherical tip and a hemispherical island on the sample, both with the same radius of curvature, it is easy to see that the actual diameter of the surface feature would be about half of the measured dimension.

These mounds are not completely stable to the stresses induced by the tunneling microscope. Figure 6 is a sequence of five scans on a 45×45 nm area of the same sample, under the same tunneling conditions. In each of the first two scans of the series, after the tip had completed the first few traversals over the largest mound, the mound appeared to shift laterally by about 5 nm. (As in all the scans in this work, the image is built up from horizontal scan lines, starting from the bottom of the picture.) It is unknown whether this instability in the position of the mound is caused by mechanical contact, larger distance tip-surface interaction forces, or is perhaps due to some inelastic inter-

action with the tunneling electrons. In the next scan [Fig. 6(c)], the location of the mound seemed to have stabilized, perhaps anchored to that spot on the surface by the smaller mound which it has moved next to. In the subsequent scan [Fig. 6(d)], however, after a single traversal of the tip over the mound, the mound disappeared. Then as the tip continued to scan over the area where the mound had been, the mound seemed to again reappear in a few of the isolated scan lines. In the last scan of the series shown in Fig. 6(e), hardly a trace of this 15 nm mound remains.

The identity of these mounds is not known. It seems unlikely that they are caused by structural defects, be they missing atoms or impurity atoms, because of their general appearance, size and clustering. Also, the observation that they are mobile under the relatively weak perturbing influence of the tip indicates that they are probably not fixed within a crystal lattice.

It seems much more probable then that they are caused either by atomic or molecular adsorbates. Recall, however, that the surface of MoS_2 is relatively inert chemically and is unreactive toward common residual gasses.[10] Gasses that are merely physisorbed are not expected to be observed with the STM under these conditions. Clear evidence of this is the ability to image with atomic-resolution in air on this and other surfaces, indicating that the tunneling tip must be displacing even the relatively strongly adsorbed contaminants such as water vapor. Nevertheless, it is conceivable that some of the ions created by the ionization gauges or ion pumps, or yet bysome other reactive species, were able to reach the surface and react with it. Alternatively, if there were interstitial metal contaminants in the octahedral sites between the sulfur layers in the van der Waals gap, they might be exposed upon cleavage of the surface. Early studies on MoS_2 suggest that a number of metal impurities are commonly incorporated in amounts up to 0.1%.[15] Other studies have suggested that a small S excess may be found at the cleavage surface of MoS_2 which can only be driven off by vacuum-baking at 650°C for 1 hour.[16]

The other likely possibility is that the mounds in the topographical images are due to intercalants or subsurface interstitial impurities. MoS_2 is known to intercalate alkali and alkali earth metals from liquid ammonia solutions. These intercalants affect the structural and electronic properties of the surface, causing the planes to spread on average (as measured by x-ray crystallography) and in many cases turning MoS_2 into a metal at room temperature, and a superconductor below 10 K.[17] Also, synthetic In_xMoS_2 ($0<x\leq1$) has been shown to have increased interlayer spacing, and decreased temperature dependence of electrical conductivity when compared to MoS_2, while remaining a semiconductor.[18] It is quite possible, then, that if interstitial impurities exist in these mineralogical samples, they might give rise to mounds in the STM topographies, either because of mechanical deformation of the top layer of MoS_2 or because of an increase in either the surface state density or the wave function decay length above the surface. Since the intercalants are not covalently bonded, they might be expected to be somewhat mobile under the influence of the tunneling probe tip. It is worth noting that these kinds of moundlike features on atomically smooth planes have been observed both in air and in vacuum, suggesting that they are a property of the samples (intercalants or exposed interstitials) and not the environment (adsorbed gasses).

Screened Defects

Some of these islandlike regions are surrounded by a depression in the topography. A hint of this type of behavior is seen in Fig. 3(b). Much clearer examples are presented in Fig. 7. As in all the images presented so far, the background corrugation or ripple that extends throughout these images is due to periodic vibrational and electrical noise. Figure 7(a) shows a 12 × 12 nm region of sample A on which is found a small island approximately 1.9 nm in diameter. This image was acquired at –0.5 V sample bias and 2 nA tunneling current using a W tip. The sample had been cleaved in air and immediately pumped down to ~ 5×10^{-9} torr five days prior to taking the image.

Surrounding the island is a small depression in the topography. Another depressed region that is due to an island which is off the edge of the scan is seen near the bottom of the image. The large range, smooth onset, and small amplitude of these depressions (the total height variation in the image is less 0.3 nm) suggest that the depressions may be due to electrostatic screening rather than to a true geometric effect.

Qualitatively similar topographies have been described by Stroscio *et al.*[19] for oxygen atoms adsorbed on the GaAs (110) surface. In their work, negative sample bias images showed the oxygen adsorbates as peaks surrounded by depressions. The underlying atomic corrugation was seen to extend through both the depression and the peak. The topographical peaks were explained as arising from a "chemical" effect—the increase in the density of filled states in the immediate vicinity of the adsorbate because of the O $2p$ states. The longer range depression, on the other hand, was thought to be due to electrostatic repulsion of the conduction band electrons from the extra negative charge at the O adsorbate. This repulsion may be viewed as band bending in a semiclassical picture. Convincing evidence that both the peak and the depression were due to electronic effects was provided by imaging the same feature in the opposite tunneling polarity. In positive sample-bias images, the O adsorbates were seen as pits in the topography, that were due presumably to a depletion in the density of empty states which they caused. This same kind of modification of the surface state density by electronegative adsorbates has been described in theoretical calculations of Lang.[20]

Unfortunately, we were unable to obtain images in both bias polarities for the selfsame feature. Nevertheless, several positive sample-bias images were obtained in the same general area of the sample. None of these images showed a large hole in the topography as might have been expected in comparison with the results on O/GaAs. Instead, what we found was qualitatively the same behavior as seen in the negative sample bias images. An example of this is seen in the 6×5 nm image of Fig. 7(b) taken

at a sample bias of –0.5 V. As before, a small mound surrounded by a larger area depression is evident.

Because of the number of times these qualitative features were observed in this region of the sample in both bias polarities, it seems reasonable to propose that they may all be due to the same effect. The negative sample-bias topographies would then be understood in analogy to the results on O/GaAs as an increase in the density of filled states at the island and a depletion of free carriers in the surrounding semiconductor. The positive sample-bias results can also be understood within this framework if it is borne in mind that they were obtained at only +0.1 V sample bias. At this low bias, the theoretical work of Lang[19] would agree that an electronegative adsorbate might still be providing an increase in the density of (empty) states over that expected for the clean surface, thus giving rise to a peak in the topography. The depression surrounding the peak can once again be explained, based on band bending in the surrounding semiconductor. In this case, the current into the depressed region is not limited by the depletion of carriers at the surface, but rather by the potential barrier that is due to the semiconductor space charge which the electrons from the tip must either penetrate or surmount.

Atomic-Resolution Imaging

Under favorable conditions, smaller area scans on smooth basal planes revealed the atomic structure of this surface. Figure 8 is a scan of a 0.9×0.9 nm area of the surface of sample A taken in vacuum of about 2×10^{-8} torr. The tip was again electro-chemically etched W, and the scan was taken on the same data run as the scans of Fig. 7. Feedback conditions of 2 nA constant current and +0.14 V sample bias were used. The scan was acquired in 24 sec at a scan rate of 13 nm/sec. The basic observed structural pattern is a centered hexagon of bright spots. The sixfold symmetry of these bright spots is broken by spots of secondary intensity centered in alternate threefold hollows. An overlay of the surface unit cell is shown for comparison with Fig. 1. We see four bright

spots in the corners, with a secondary site at one end of the long diagonal, and a dark site in the other end of the unit cell, in agreement with the expected crystal structure.

Figure 9 shows the amplitude of the surface corrugation along the cross-sectional cuts indicated by the dotted lines in Fig. 8. Figure 9(a) is a cut along a $[\bar{1}\bar{1}0]$ cell diagonal and clearly shows a major peak, a secondary peak, and a hollow. The peak-to-hollow corrugation amplitude is about 0.05 nm, while the difference in height of the primary and secondary peaks is roughly half that. It is worth noting that in contrast to what is sometimes seen on graphite,[4,5] there is nothing unexpected or "anomalous" about this corrugation amplitude, despite the similar mechanical properties of graphite and MoS_2. Figure 9(b) shows the corrugation along a $[\bar{1}00]$ cell edge, where only a simple sinusoidal modulation is evident. The peak-to-hollow amplitude measured along this edge is almost as large as that along the $[\bar{1}\bar{1}0]$ cell diagonal.

Atomic-resolution current-contrast images were also acquired on this same surface. Because of the higher scan speeds, these images show less external noise interference and a complete absence of thermal drift effects.[21] The current images presented here were acquired in 1.6 sec at a scan rate of 135 nm/sec. The image shown in Fig. 10 was taken at an average tunneling current of 2 nA and a sample bias of +0.25 V. The gray scale reflects the variation in the tunnel current relative to its mean value. Once again, the unit cell is outlined to guide the eye. Cuts taken through these data along the dotted lines indicated are presented in Fig. 11. The cut along the $[\bar{2}10]$ cell diagonal shows a repeated pattern of primary peak, secondary peak and valley, with a total current variation of 50% in $\Delta I/I$, while along the $[0\bar{1}0]$ unit cell edge, a smaller sinusoidal variation is observed, as required by symmetry.

All of the scan dimensions quoted in this chapter are based on the measured piezoceramic lengths and the manufacturer supplied expansion coefficients, and none of the figures has been corrected for piezo drive non-orthogonality. As a result, the

atomically-resolved images show some distortion, and the measured lattice spacings all vary by about ±10% from the expected values indicated in Fig. 1.

Although high-resolution images displaying the two distinct sites were regularly observed on several different samples using a variety of both Au and W tips, not all atomically resolved images showed this structure. Because of the multiplicity of image types, there has been some question that the secondary sites which we often see on these MoS_2 surfaces may be due to a double tip effect, especially in light of similar effects in HOPG.[22] Figure 12 shows another current image of the MoS_2 surface, using the same physical tip and sample combination. This image was also acquired at 2 nA tunneling current, but at a sample bias of +0.14 V. The same centered hexagonal pattern of bright spots seen in Fig. 10 is observed, but the spots of secondary intensity seem to be missing. Fig. 13 shows cuts through the data along the lines indicated in Fig. 12. The cut along the unit-cell diagonal shows some evidence that even in this image the secondary site persists, albeit at lower intensity. It is also interesting to note that the "two-site" image shown in Fig. 10 has a greater corrugation amplitude than the "single-site" image of Fig. 12, despite the fact that the two-site image was acquired at a slightly higher bias voltage, and therefore presumably at a greater tip-sample separation where the corrugation of the surface wave function is expected to be smaller. This suggests that the microtip active in tunneling in Fig. 10 is sharper than that of Fig. 12. That is, in Fig. 10 the tip must be sampling a smaller area of the surface plane, thus allowing it to better resolve the detailed corrugations of the surface wave function. Although certainly not ruling out the possibility of a double tip, this observation, in conjunction with the accurate placement of the secondary site within the unit cell, and the frequency with which we see the two-site images, leads us to the conclusion that the two sites observed in these images are indeed due to the two atomic species within the surface unit cell.

Assignment of the Two Sites

Given that the two sites observed in these high-resolution images are due to topographical features, it still remains to assign which is associated with which surface atom. Simple geometric considerations would lead to the assignment of the higher peaks to the sulfur atoms, which are closest to the tip, while the secondary peaks would arise from the molybdenum atoms in the second layer. The predominant feature governing tunneling microscope images, however, is the contribution made by each atom's valence orbitals to the position *and* energy-dependent density of states at energies near the Fermi level and at distances above the surface normally associated with tunneling.[13,23] Numerous theoretical investigations of the band structure of MoS_2 point to strongly covalent bonding with a substantial Mo 4*d* contribution at the top of the valence band and bottom of the conduction band.[7,24] Thus, one cannot *a priori* ignore the possibility that Mo 4*d* levels, rather than S 3*p* levels, are primarily responsible for the tunneling current. Ultraviolet photoelectron spectroscopy performed on MoS_2 reveals a large peak in the density of states near the top of the valence band, which appears to be due mainly to the Mo $4d_{z^2}$ non-bonding orbital.[25] The symmetry of the lower conduction band states is still open to debate, but is probably due to some mixture of Mo $4d_{(x^2-y^2)}$ and $4d_{xy}$ with the addition of some S 3*p*. Thus, the empty-state density might be expected to be centered between atoms, or possibly on the S. Tunneling images acquired at opposite sample bias might therefore exhibit a shift in the topographic maxima.

Alternate-Bias Current Imaging

In order to test for any possible shift in the topographic maxima at opposite sample biases, we have implemented an alternate bias current-imaging scan mode. In this method, the sample is scanned four times sequentially in the current-imaging mode under microprocessor control with the possibility of changing the tunneling bias voltage

between each scan. For the 126 × 126 pixel scans which we acquired, each image took a total of 3.3 seconds to acquire and display.

Figure 14 is a set of images that was acquired in this way, with a sample bias of −0.3 V for scans (a) and (c), and +0.7 V for scans (b) and (d). These scan voltages were selected by taking current-voltage scans at constant separation with the gap stabilized at 1 nA and +0.7 V. The sample bias for the negative bias scans was then chosen as the voltage at which the absolute value of the current was again 1 nA. In this way, the same current set-point in both positive and negative sample bias corresponds to approximately the same tip-sample spacing.

Very little thermal drift is expected between images at this 3.3 second refresh rate. That this is indeed the case can be seen by comparing the images in (a) and (c) or in (b) and (d). Therefore, if any shift is seen in the location of the topographic maxima between the images at opposite sample bias, it must be due to an electronic effect. What we find, however, is that for this series of images, at least, the positioning of the topographic maxima seems to be independent of sample bias. This does not rule out the possibility that in images taken using higher or lower tunnel currents or sample biases, a shift in the topographic maxima might be seen. Some preliminary evidence of this has recently been observed.[26]

It remains inconclusive then which specific surface sites are actually responsible for the peaks in our atomically resolved images. The tunneling matrix elements that determine the rate of electron transfer between the tip and the sample involve both geometric and energetic factors. In predicting the location of the highest electron transfer rate for this particular system (at negative sample bias at least), these two factors are in opposition. Distance considerations favor dominance over the S atoms, but for tunneling from the valence band, the proper energy electrons have the highest probability near the metal. A careful theoretical study is therefore necessary to gain the proper intuition.

Some progress has been made in recently this vein, which indicates that the dominance of one or the other effect is very sensitive to the tip-sample separation.[27]

Conclusions

Molybdenum disulfide is an interesting sample for tunneling microscope studies because of its unique electronic and structural properties. Of special interest is the possibility of probing the differences between the two surface atoms in the basal plane. Many unexpected imaging effects are observed that illustrate the importance of a thorough understanding of the tip-surface interaction and the imaging conditions. It is clear, for example, that on this as well as on other semiconductor samples, very different surface topographies may be observed at different tunnel biases, both in atomic-resolution images and in lower-resolution, large-area scans. The measured topographies are understood to be a convolution of the topographical and electronic structure of the tip and the sample. Also, the forces exerted by the tip on the surface have been observed to cause changes in the surface morphology, especially for features that are not strongly surface bound.

Atomic-resolution images of MoS_2 were also obtained in both the constant-current and the current-contrast imaging modes. These images reveal two distinct sites in the surface unit cell that can be correlated with the locations of the Mo and S atoms within the crystal structure. The assignment of a particular imaged site with a specific atomic species is complicated on this surface because of competing electronic and geometric effects. Further experimental work, such as measurements of opposite bias topographies under a wide range of operating conditions (separations, bias voltages) will be an important step in in understanding this problem.

References

§ *Portions of this chapter have been published as:* M. Weimer, J. Kramar, C. Bai, J. D. Baldeschwieler, *Phys. Rev.* **B 37**(8), 4292–5 (1988); M. Weimer, J. Kramar, C. Bai, J. D. Baldeschwieler, W. J. Kaiser, *J. Vac. Sci. Technol.* **A 6**(2), 336–7 (1988).

1. G. Binnig, H. Rohrer, Ch. Gerber, E. Weibel, *Phys. Rev. Lett.* **49**(1), 57–61 (1982).

2. *For a recent review of STM see:* P. K. Hansma, J. Tersoff, *J. Appl. Phys.* **61**(2), R1-23, (1987).

3. R. M. Feenstra, J. A. Stroscio, J. Tersoff, A. P. Fein, *Phys. Rev. Lett.* **58**(12), 1192–5 (1987).

4. S. Morita, S. Tsukada, N. Mikoshiba, *Jap. J. Appl. Phys.* **26**(4), L306–8 (1987).

5. J. M. Soler, A. M. Baró, N. Garcia, H. Rohrer, *Phys. Rev. Lett.* **57**(4), 444–7 (1986); H. J. Mamin, E. Ganz, D. W. Abraham, R. E. Thomson, J. Clarke, *Phys. Rev.* **B 34**(12), 9015–8 (1986); J. B. Pethica, *Phys. Rev. Lett.* **57**(25), 3235 (1986).

6. J. Tersoff, *Phys. Rev. Lett.* **57**(4), 440–3 (1986).

7. V. Grasso, ed., *Electronic Structure and Electronic Transistions in Layered Materials*, Reidel, Dordrecht, Holland (1986).

8. K. K. Kam, B. A. Parkinson, *J. Phys. Chem.* **86**, 463–7 (1982).

9. R. G. Dickinson, L. Pauling, *J. Am. Chem. Soc.* **45**, 1466–71 (1923).

10. R. H. Williams, A. J. McEvoy, *J. Phys.* **D 4**, 456–64 (1971); M. Salmeron, G. A. Somorjai, A. Wold, R. Chianelli, K. S. Liang, *Chem. Phys. Lett.* **90**(2), 105–7 (1982).

11. G. W. Stupian, M. S. Leung, *Appl. Phys. Lett.* **51**(19), 1560–2 (1987).

12. D. Sarid, T. D. Henson, N. R. Armstrong, L. S. Bell, *Appl. Phys. Lett.* **52**(26), 2252–4 (1988).

13. Ch. Gerber, G. Binnig, H. Fuchs, O. Marti, H. Rohrer, *Rev. of Sci. Instrum.* **57**(2), 221–4 (1986).

14. J. Tersoff, D. R. Hamann, *Phys. Rev.* **B 31**(2), 805–13 (1985).

15. R. F. Frindt, A. D. Yoffe, *Proc. Roy. Soc.* **A 273**, 69–83 (1963); B. L. Evans, P. A. Young, *Proc. Roy. Soc.* **A 284**, 402–22 (1965).

16. J. S. Zabinski, B. J. Tatarchuk, *Mat. Res. Soc. Symp. Proc.* **140**, 239–44 (1989).

17. R. B. Somoano, A. Rembaum, *Phys. Rev. Lett.* **27**(7), 402–4 (1971).

18. S. K. Srivastava, B. N. Avasthi, *Synth. Metals* **11**, 193–205 (1985).

19. J. A. Stroscio, R. M. Feenstra, A. P. Fein, *Phys. Rev. Lett.* **58**(16), 1668–71 (1987).

20. N. D. Lang, *Phys. Rev. Lett.* **B 58**(1), 45–8 (1987).

21. A. Bryant, D. P. E. Smith, C. F. Quate, *Appl. Phys. Lett.* **48**(13), 832–4 (1986).

22. H. A. Mizes, S. Park, W. A. Harrison, *Phys. Rev.* **B 36**(8), 4491–4 (1987).

23. J. Tersoff, D. R. Hamann, *Phys. Rev. Lett.* **50**(25), 1998–2001 (1983).

24. R. Coehoorn, C. Haas, J. Dijkstra, C. J. F. Flipse, R. A. de Groot, A. Wold, *Phys. Rev.* **B 35**(12), 6195–202 (1987).

25. R. Mamy, A. Boufelha, B. Carricaburu, *Phys. Stat. Sol.* **B 141**, 467–73 (1987).

26. M. G. Youngquist, *private communication.*

27. T. R. Coley, *private communication.*

Figure 1

The crystal structure of $2H$–MoS_2 as determined by x-ray diffraction, showing **(a)** the (001) surface structure and **(b)** the (110) cross section [along the dashed line in (a)].

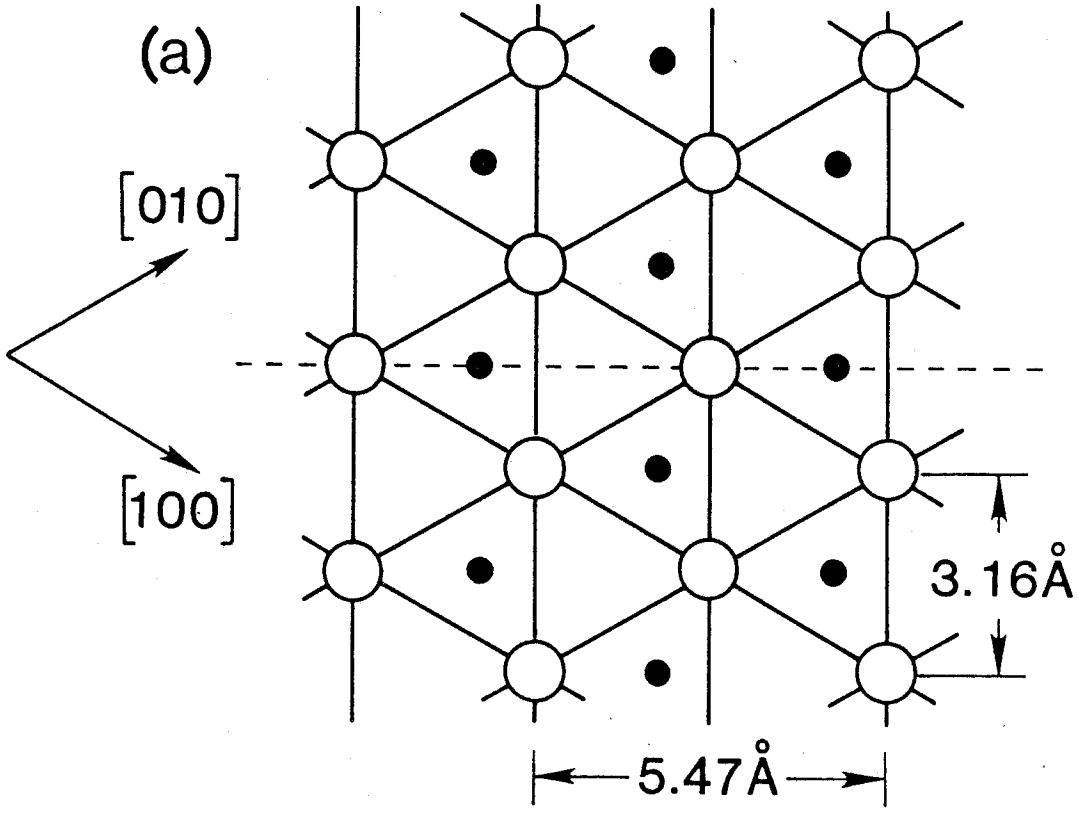
(a)
[010]
[100]
3.16Å
5.47Å

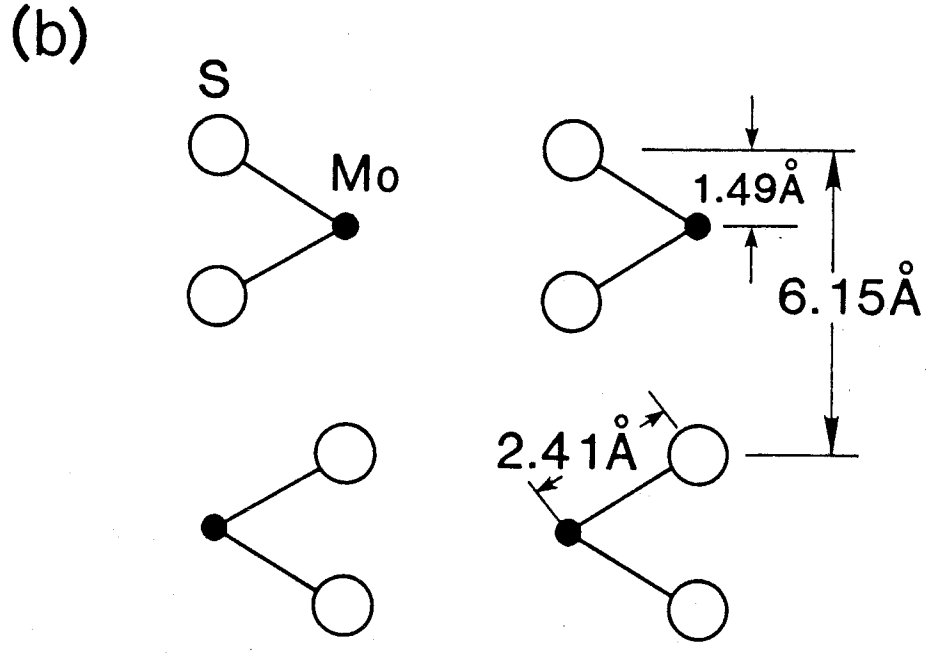
(b)
S
Mo
1.49Å
6.15Å
2.41Å

Figure 2

A 180 × 180 nm scan of sample A shown in both (**a**) line scan and (**b**) gray scale images. The scan was taken in vacuum of ~ 5×10^{-9} torr with an electrochemically etched W tip. Sample bias is 0.6 V, and tunneling current feedback set point is 2 nA.

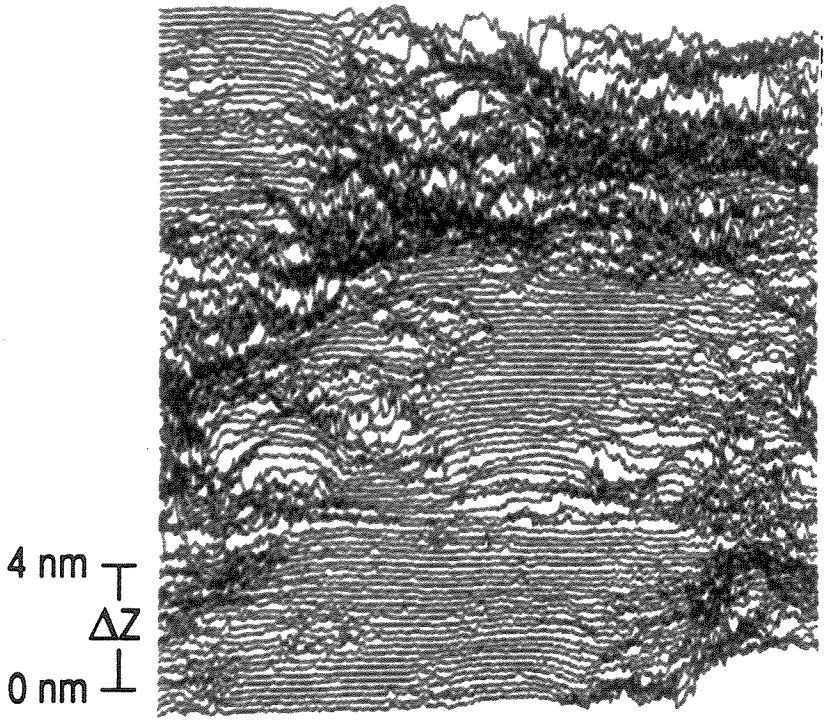

180 × 180 nm

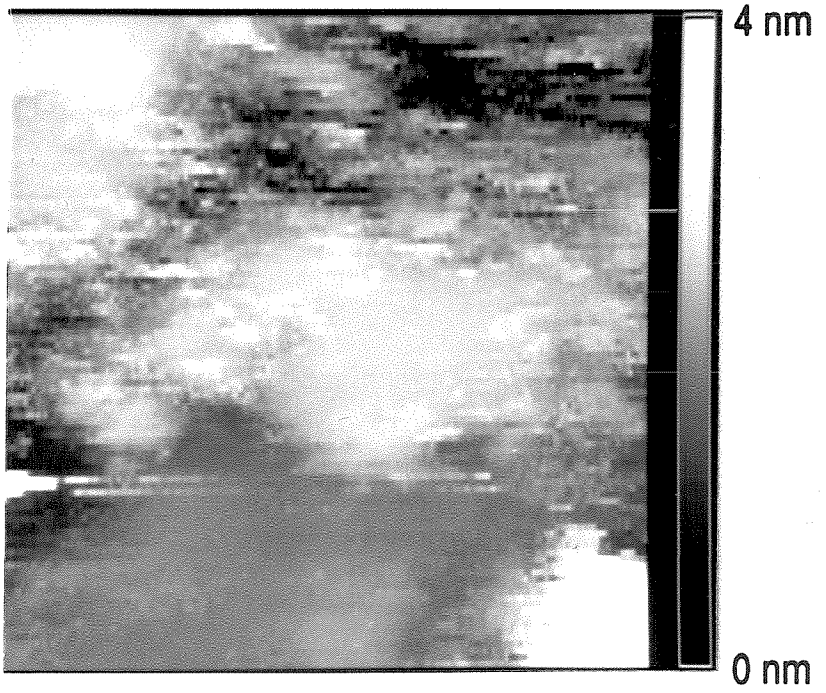

180 × 180 nm

Figure 3

(a) Gray scale image of a 12 × 12 nm scan of sample A with the same tunneling conditions as in Fig. 2. (0.6 V sample bias, 2 nA tunneling current) **(b)** A subsequent scan of the same general area of the sample (offset by thermal drift) with the sample bias changed to 2.0 V, but with the current feedback set point still at 2 nA. Note the subtle differences in measured topography and the decrease in noise in (b). The abrupt steps in image height (such as the white line about halfway up the image) are due to sudden (apparently reversible in this case) changes in the microscopic tip structure.

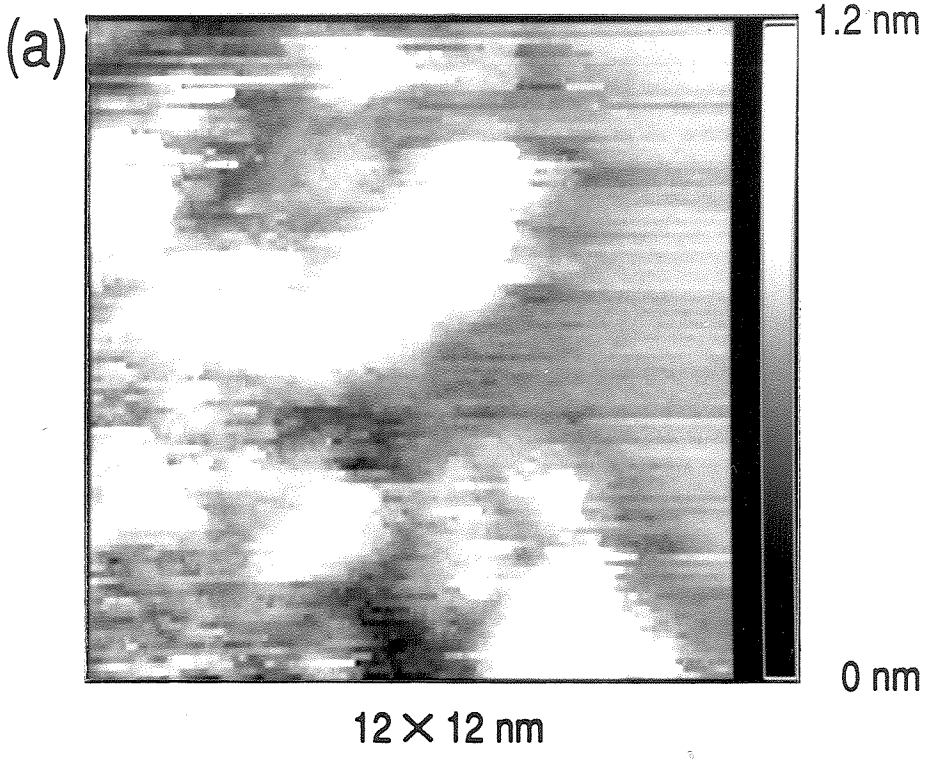
(a)
1.2 nm
0 nm
12 × 12 nm

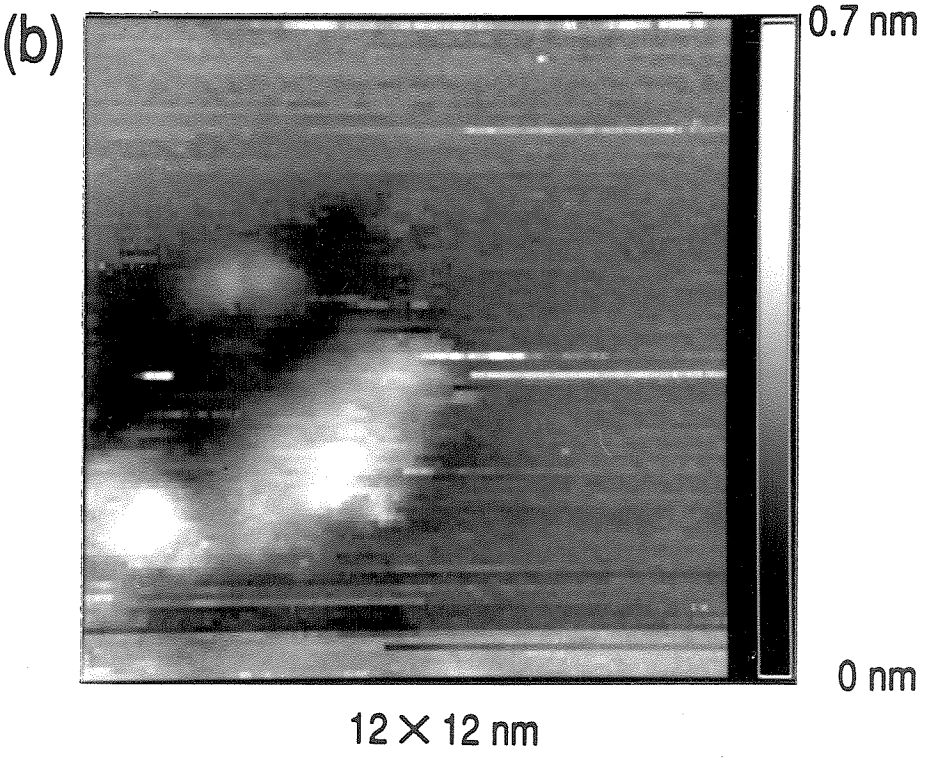
(b)
0.7 nm
0 nm
12 × 12 nm

Figure 4

Four sequential images of the same 45 × 45 nm area of sample B taken in air with an AC etched Au tip at a tunneling-current feedback set point of 1 nA. All four images were acquired within a period of 25 min. The sample bias voltages for the images were **(a)** −0.5 V, **(b)** +0.5 V, **(c)** −0.5 V, and **(d)** +1.25 V. The tip was about 3 nm closer to the surface in scan (b) than in the other three scans.

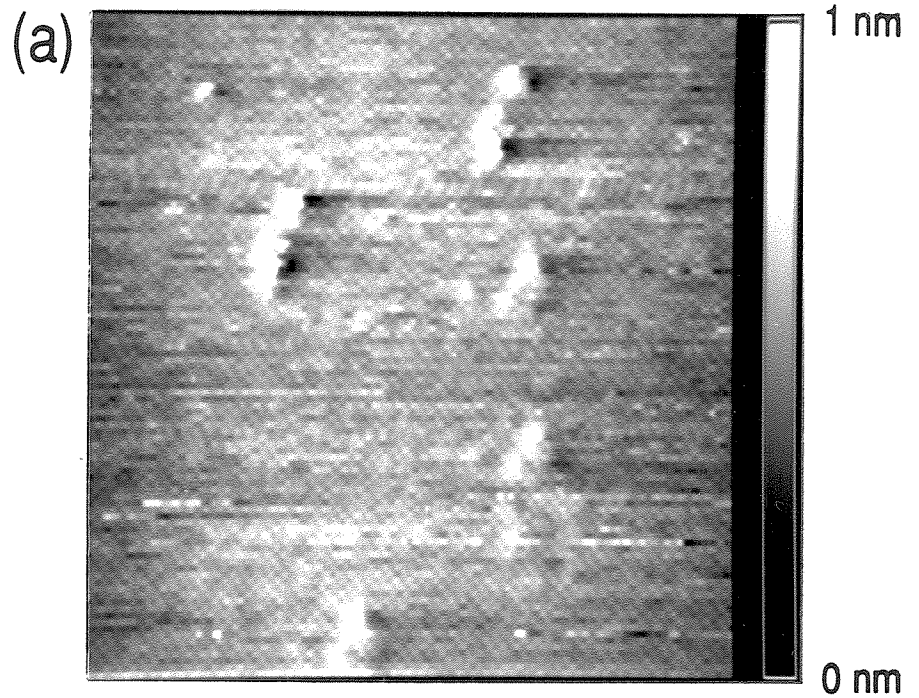
(a)
1 nm
0 nm
45 × 45 nm

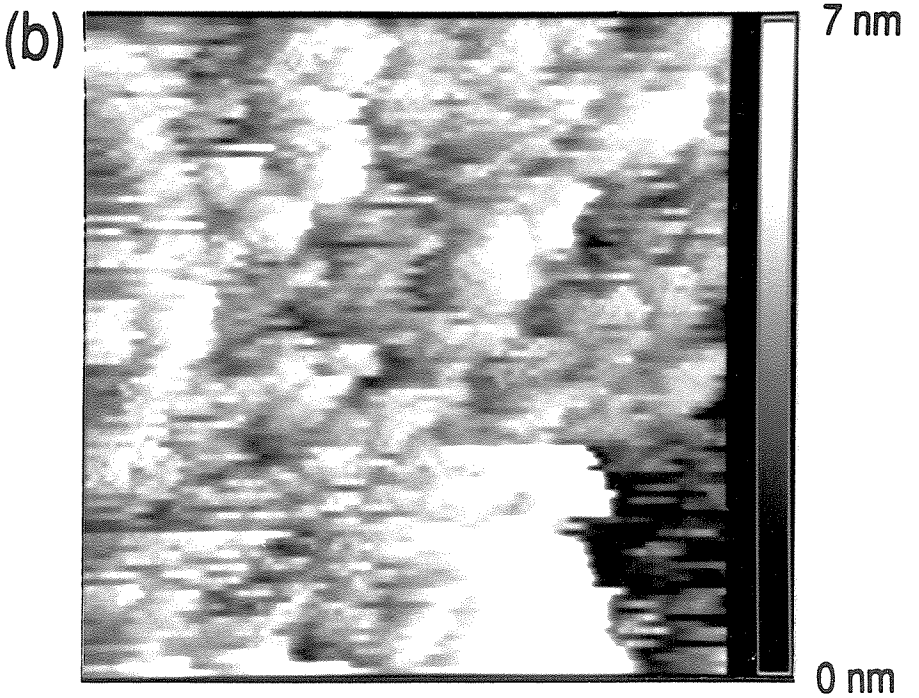
(b)
7 nm
0 nm
45 × 45 nm

(c)

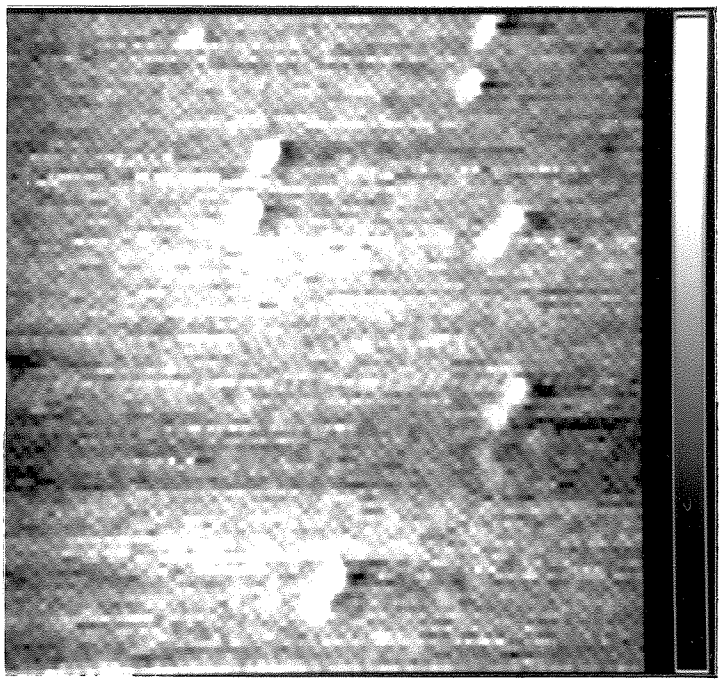

0.8 nm

0 nm

45 × 45 nm

(d)

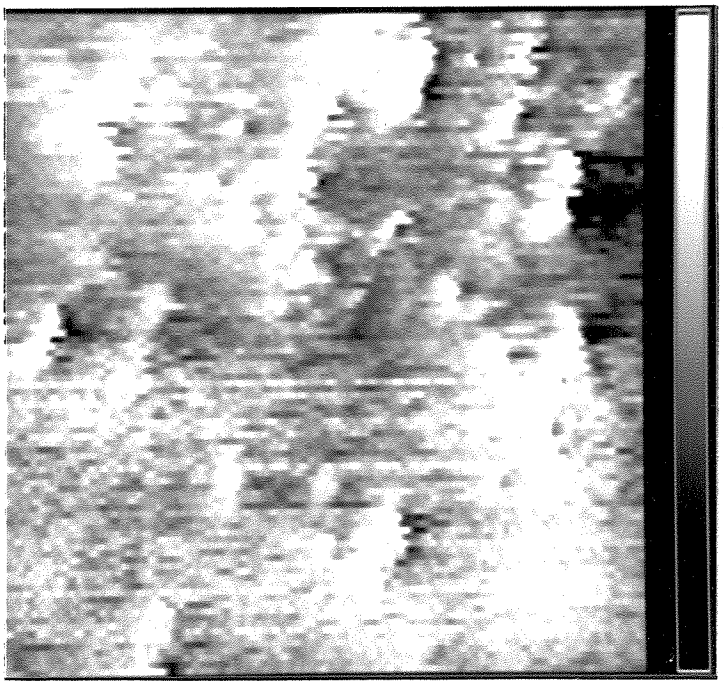

2.5 nm

0 nm

45 × 45 nm

Figure 5

Islands or mounds on the surface of sample A taken with an AC etched Au tip with the sample in a vacuum of 10^{-10} torr. Each subsequent image encompasses a larger area going from **(a)** 90×90 nm to **(b)** 180×180 nm to **(c)** 360×360 nm. All three were taken with the same conditions of +1.0 V sample bias and 1 nA tunneling current.

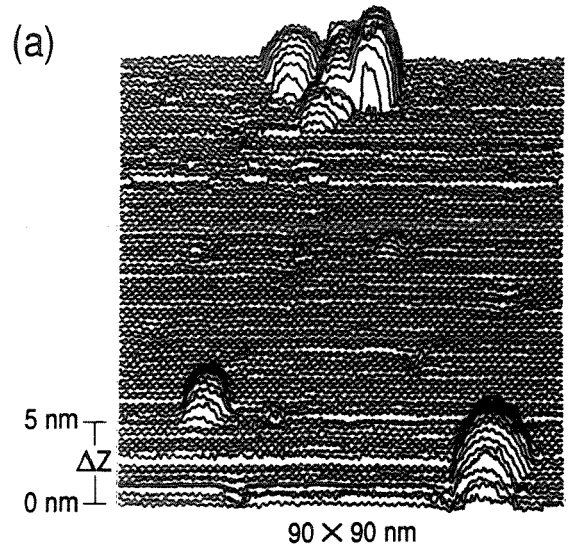
(a)
5 nm
ΔZ
0 nm
90 × 90 nm

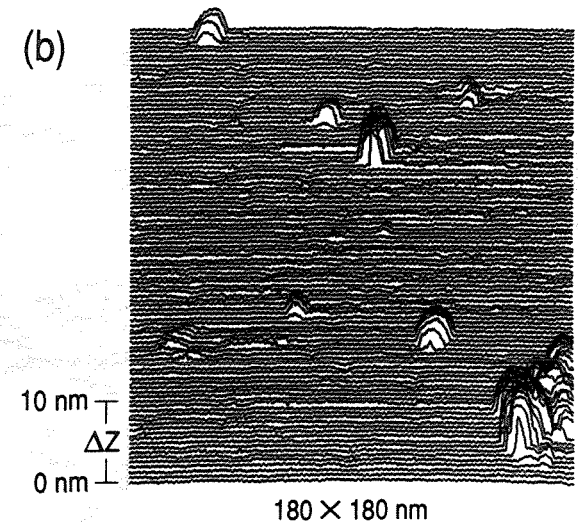
(b)
10 nm
ΔZ
0 nm
180 × 180 nm

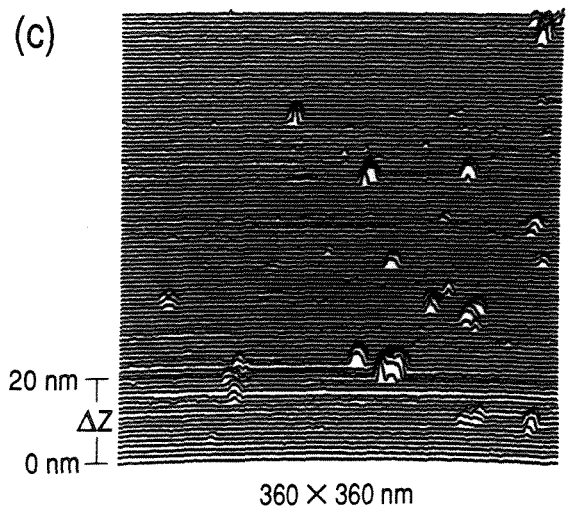
(c)
20 nm
ΔZ
0 nm
360 × 360 nm

Figure 6

A series of five scans over a 45×45 nm area of sample A, using the same tunneling conditions as in Fig. 5. In **(a)** and **(b)**, after the tip had made a few traversals over the larger mound near the top of the image, the mound was seen to shift laterally. In **(c)** the location of the mound appears to have stabilized, but in **(d)** even though the mound doesn't appear to have shifted farther, only a few of the scan lines show its presence. In **(e)** the mound has all but disappeared.

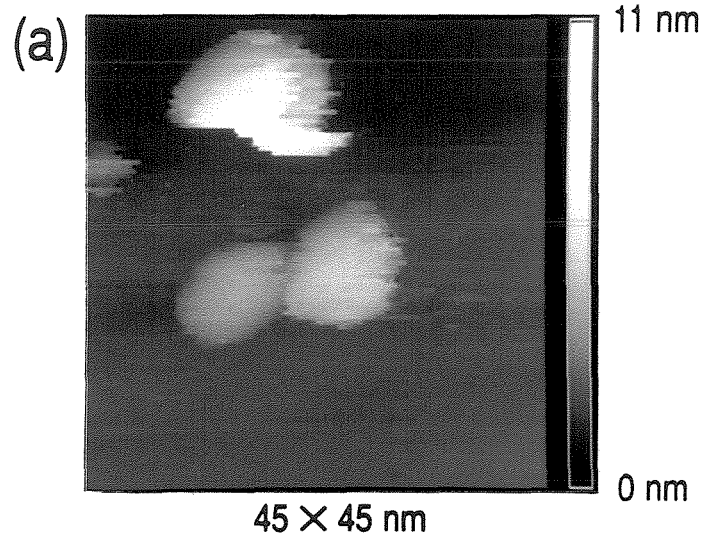
(a)
11 nm
0 nm
45 × 45 nm

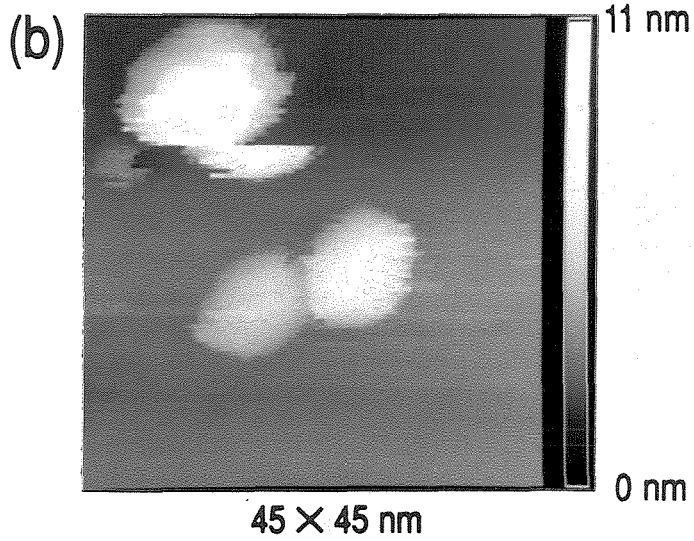
(b)
11 nm
0 nm
45 × 45 nm

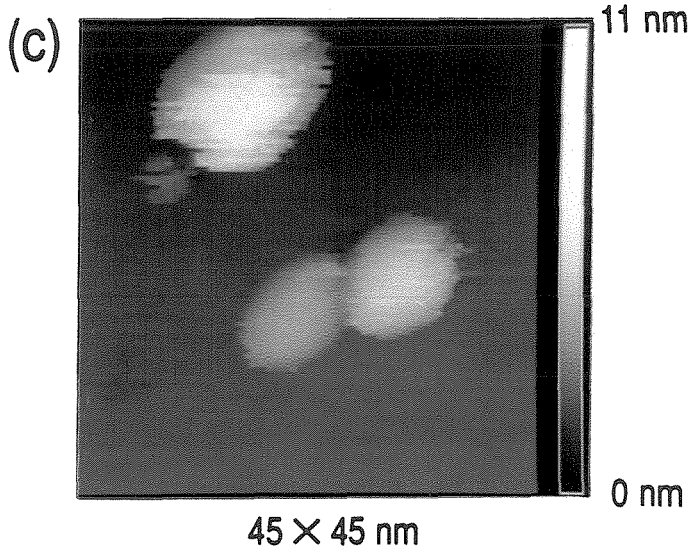
(c)
11 nm
0 nm
45 × 45 nm

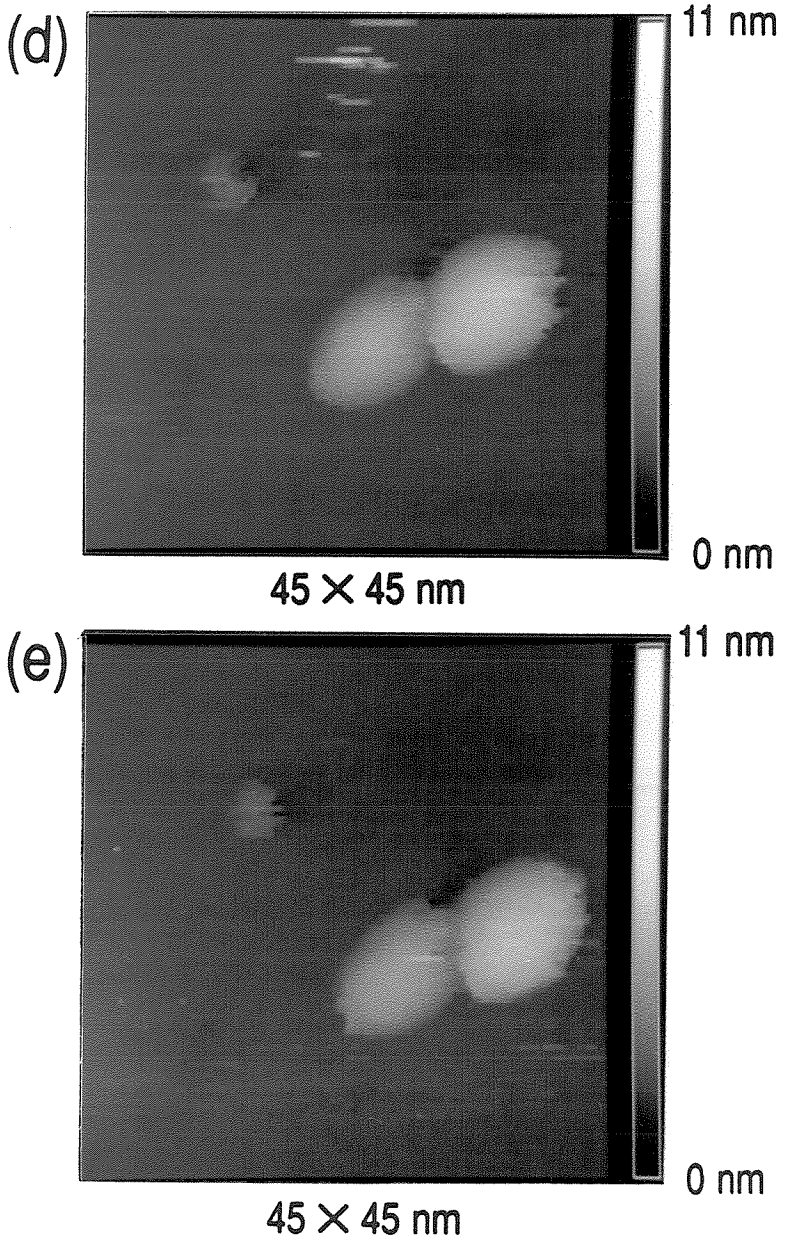
(d)
11 nm
0 nm
45 × 45 nm
(e)
11 nm
0 nm
45 × 45 nm

Figure 7

Topographical images of islandlike features surrounded by depressions on air-cleaved sample A using a W tip at $\sim 5 \times 10^{-9}$ torr. **(a)** A 1.9 nm diameter island in a 12 $\times$ 12 nm viewing window at -0.5 V sample bias. **(b)** A 0.9 nm diameter island in a 6 $\times$ 5 nm window acquired at +0.1 V sample bias. A feedback set point of 2 nA was used for both images.

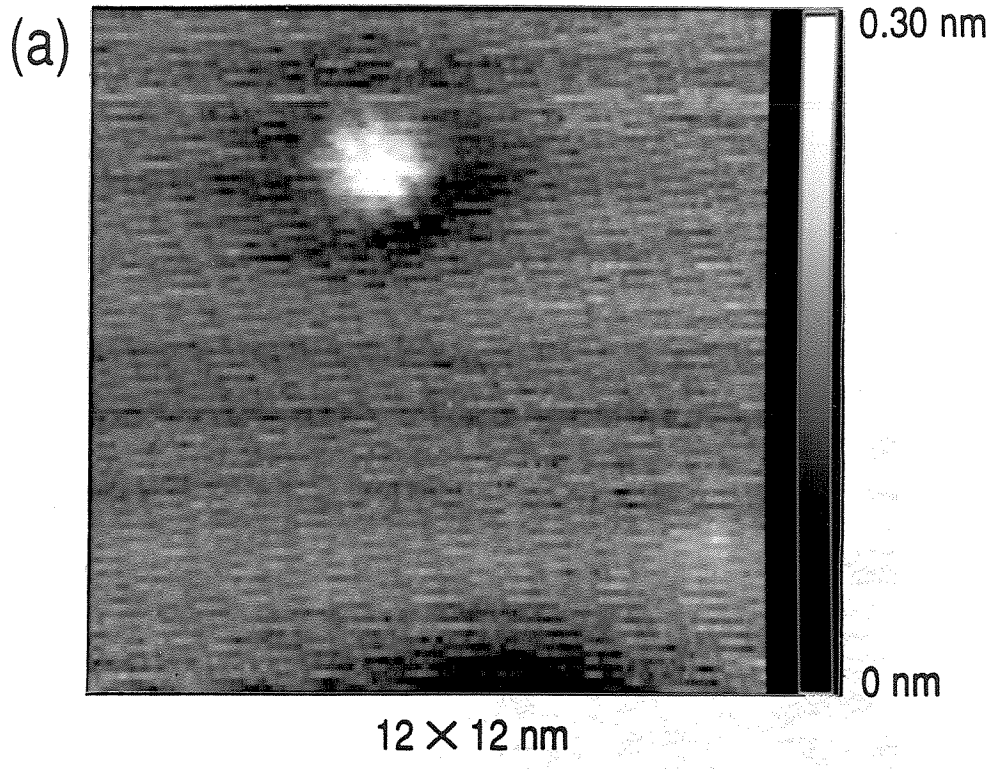
(a)
0.30 nm
0 nm
12 × 12 nm

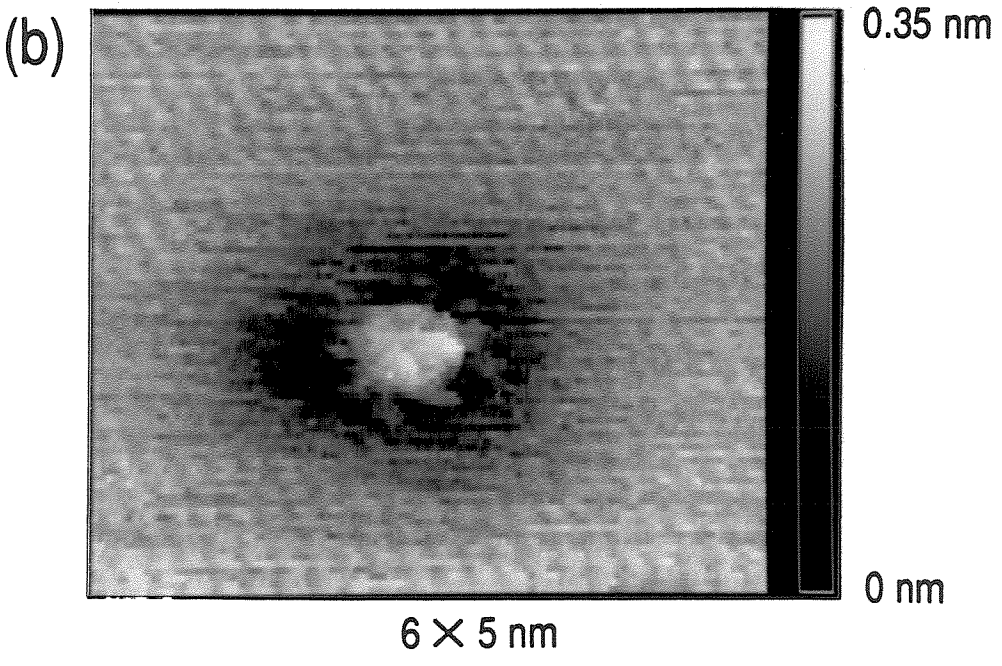
(b)
0.35 nm
0 nm
6 × 5 nm

Figure 8

Atomic-resolution, constant-current image of MoS_2. The image is of a 0.9 × 0.9 nm area taken with a W tip in a vacuum of 2×10^{-8} torr. Feedback conditions were +0.14 V sample bias and 2 nA tunneling current. The image is digitally low-pass-filtered, using a 33 point binomially weighted, sliding-window average, equivalent to a 2-D Gaussian of about 90 pm FWHM.

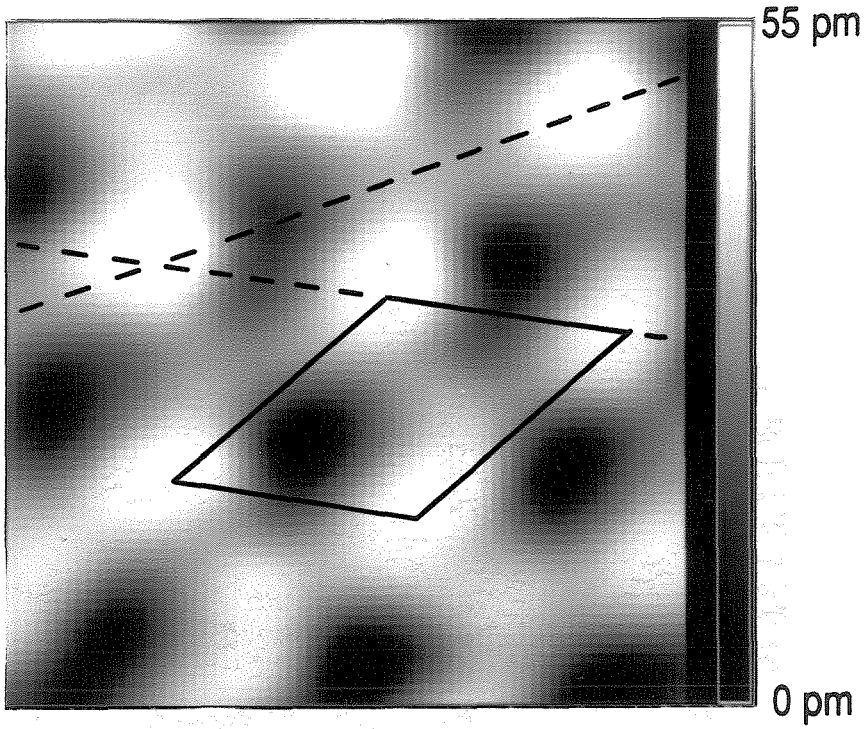
55 pm
0 pm
0.9 × 0.9 nm

Figure 9

Cross-sectional cuts through the data of Fig. 8 along the lines indicated. **(a)** A cut along the [$\bar{1}\bar{1}0$] cell diagonal. **(b)** A cut along the [$\bar{1}00$] cell edge.

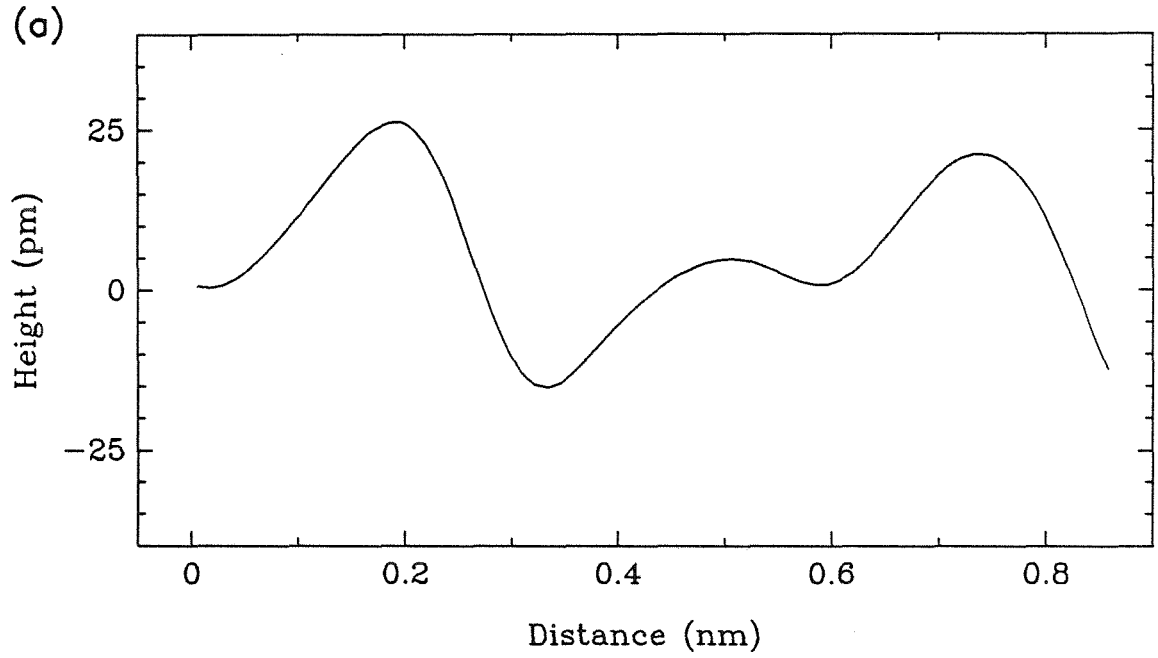
(a)
25
0
−25
Height (pm)
0
0.2
0.4
0.6
0.8
Distance (nm)

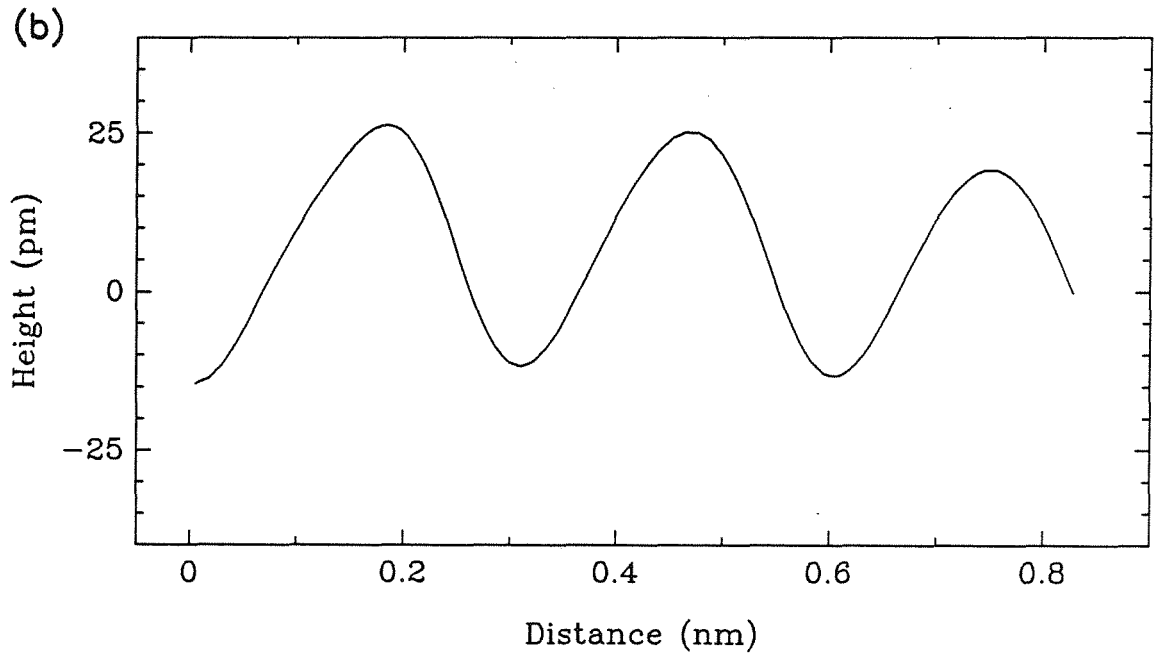
(b)
25
0
−25
Height (pm)
0
0.2
0.4
0.6
0.8
Distance (nm)

Figure 10

A 1.2 × 1.2 nm atomic-resolution, current-contrast image of MoS_2 at +0.25 V sample bias and 2 nA mean tunnel current under the same conditions as Fig. 8. The gray scale indicates the fluctuation of the current relative to its mean. This image was also low-pass-filtered in the same way as Fig. 8.

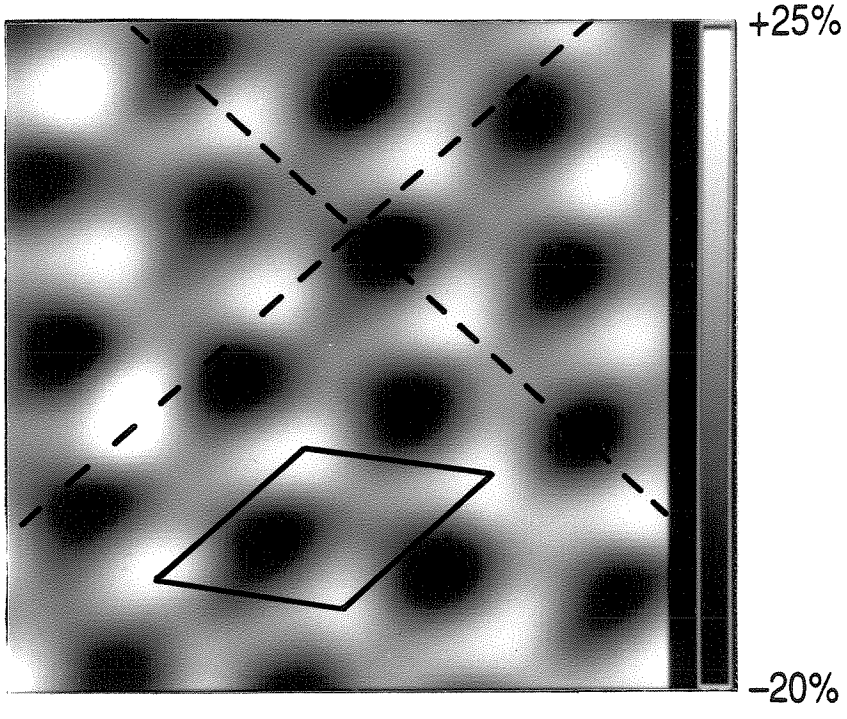
+25%
–20%
1.2 × 1.2 nm

Figure 11

Cross-sectional cuts through the data of Fig. 10 along (**a**) the [$\bar{2}$20] cell diagonal and (**b**) the [0$\bar{1}$0] cell edge.

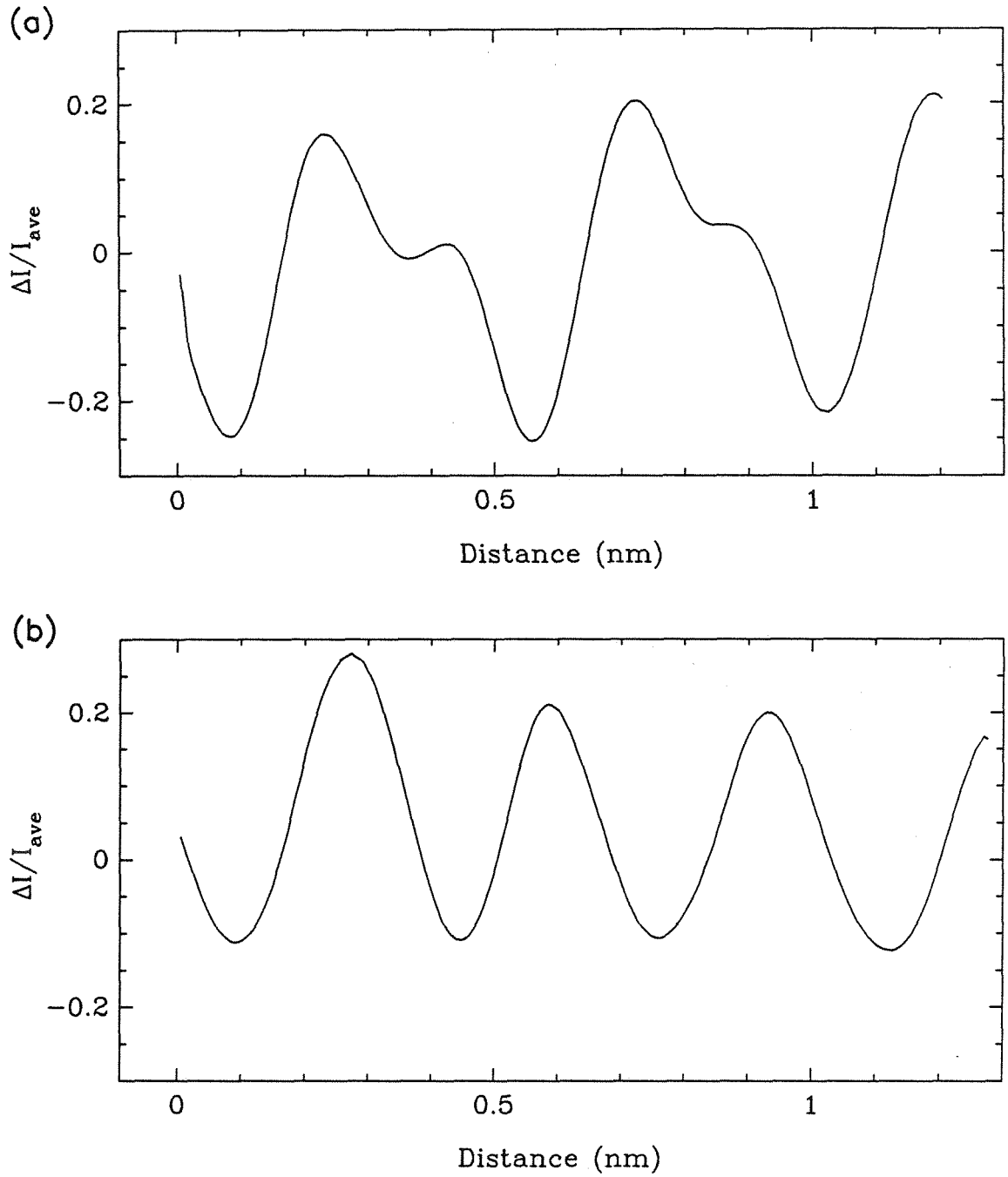
(a)
0.2
0
−0.2
ΔI/I_ave
0
0.5
1
Distance (nm)
(b)
0.2
0
−0.2
ΔI/I_ave
0
0.5
1
Distance (nm)

Figure 12

A current-contrast image of MoS_2 in which the secondary sites are not observed. The same physical tip and surface are used as in Fig. 10, and the image is acquired in the same way and presented using the same filtering. The only different external parameter is the sample bias, which is now changed to +0.14 V.

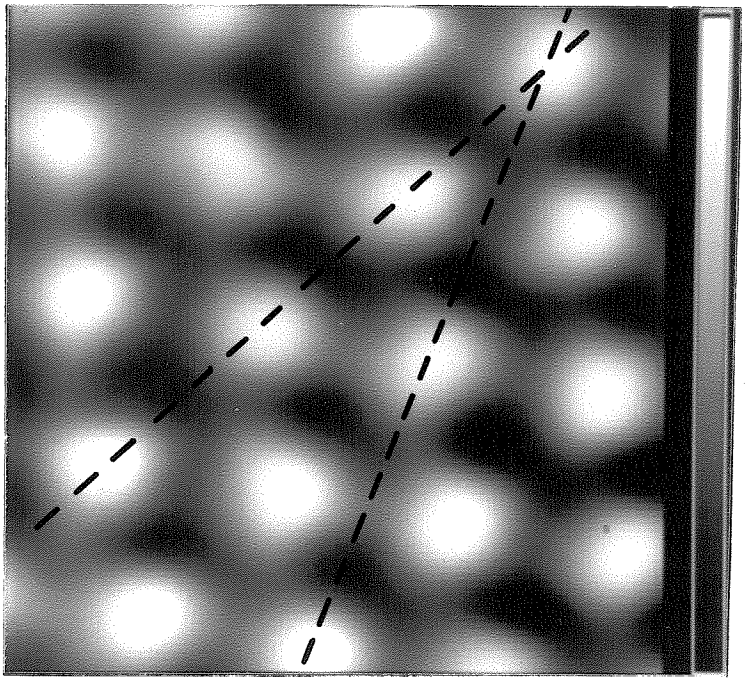
+20%
−15%
1.2 × 1.2 nm

Figure 13

Cross-sectional cuts through the data of Fig. 12 along **(a)** the unit-cell diagonal and **(b)** the unit-cell edge indicated by the lines in Fig. 12.

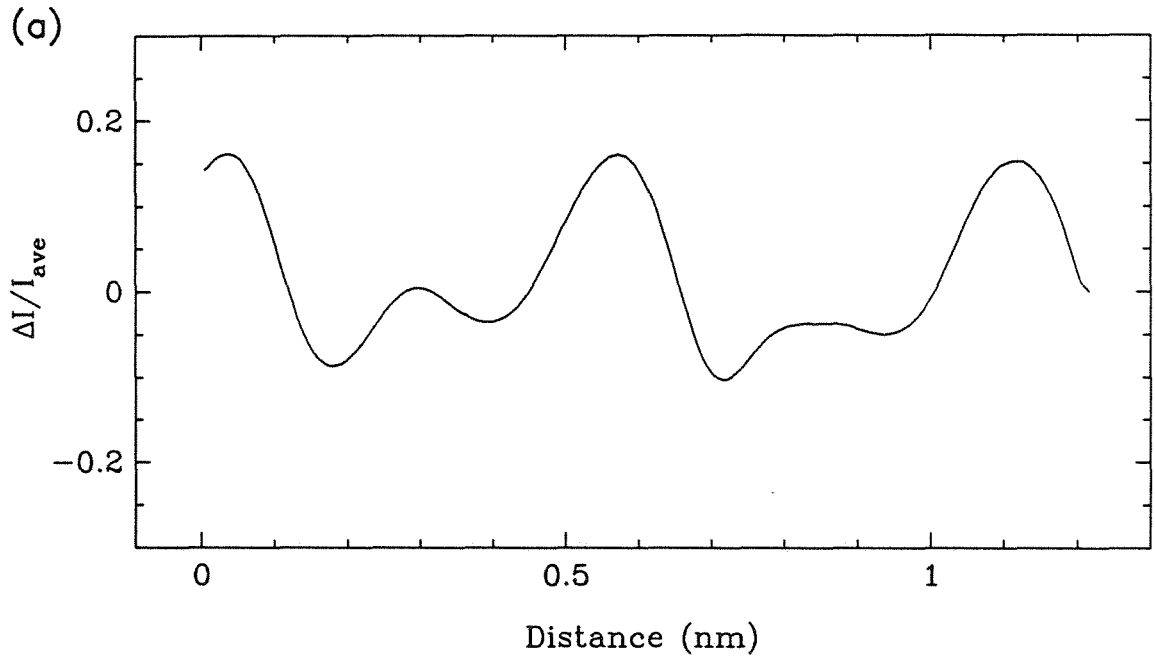
(a)
0.2
0
−0.2
ΔI/I_ave
0
0.5
1
Distance (nm)

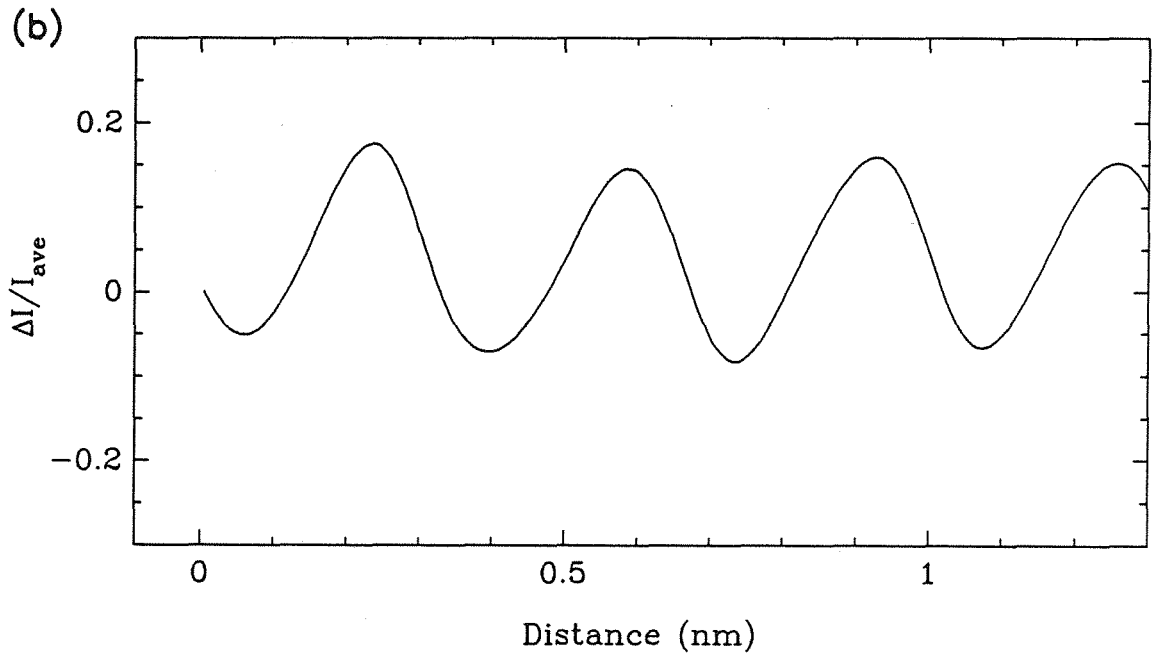
(b)
0.2
0
−0.2
ΔI/I_ave
0
0.5
1
Distance (nm)

Figure 14

Alternate bias current-contrast images of MoS_2 taken on sample B with an Au tip in a vacuum of ~ 1×10^{-9} torr. The sample was cleaved in N_2 flow and baked in vacuum for 30 minutes at 450 °C. The sample bias was sequentially altered from **(a)** −0.3 V to **(b)** +0.7 V to **(c)** −0.3 V to **(d)** +0.7 V. All four scans were acquired within a 12 second period. The mean tunneling current was 1 nA in all images. Scan size and filtering are the same as in Fig. 10.

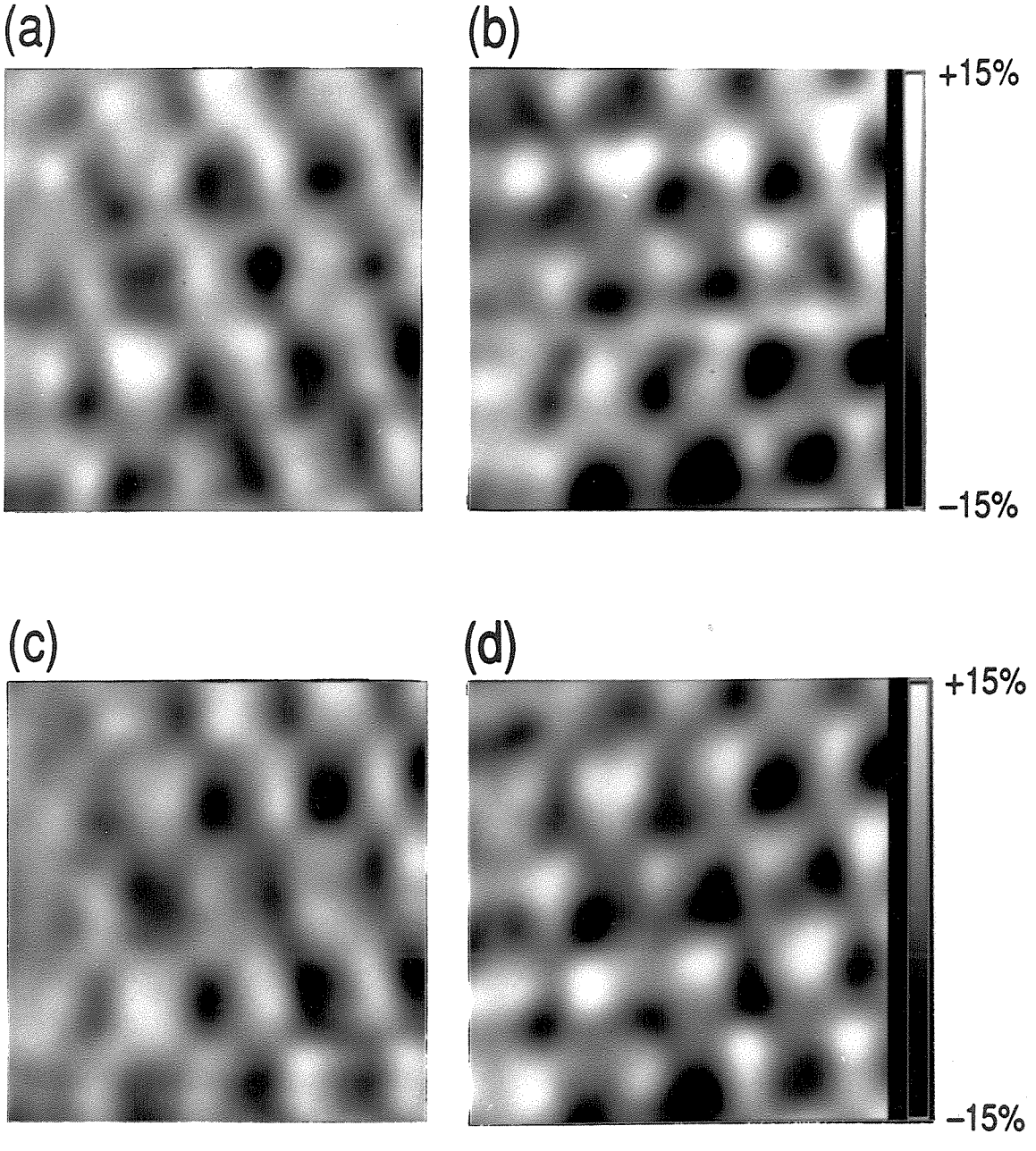
(a)
(b)
+15%
–15%
(c)
(d)
+15%
–15%
1.2 × 1.2 nm

Chapter 4

SEPARATION DEPENDENCE OF TIP-INDUCED BAND-BENDING EFFECTS IN SCANNING TUNNELING MICROSCOPE CURRENT MEASUREMENTS§

Introduction

Several important semiconductor surfaces, notably the cleavage surfaces of most of the III-V semiconductors[1] as well as specially prepared Si (111) surfaces,[2,3] have unusually low surface-defect densities and an absence of intrinsic surface states within the semiconductor band gap, resulting in a Fermi level that is not pinned at the vacuum-semiconductor interface. This means that the surface Fermi level will change relative to the band edges as the doping level of the semiconductor is changed or as an external field is applied. Recent scanning tunneling microscope (STM) studies of such a surface, the H-terminated Si (111) surface, have demonstrated the importance of tip-induced band bending in the tunneling current-voltage characteristics of these systems.[3] In this chapter, a model calculation is presented whereby the effects of tip-induced band bending on both the current-voltage behavior as a function of separation and the current-distance characteristics can be qualitatively understood. This model is based on the foundational work of Bell and Kaiser *et al.*[3]

MIS Theory

The theory of planar metal-insulator-semiconductor (MIS) structures serves as our starting point.[4] Tip-induced band bending at an ideal, unpinned semiconductor surface is illustrated in Fig. 1 for an *n*-type sample with no external bias. The field in the vacuum and in the space-charge region of the semiconductor arises from the difference in tip and sample work functions, $\Delta\phi = \phi_m - \phi_s$, where ϕ_s is the sum of the semiconductor electron affinity, χ, and the offset of the Fermi level from the conduction band minimum, ϕ_n. The semiconductor surface diffusion potential, V_d, under the influence of this field and any external bias voltage, V, applied to the sample, can be obtained by integration of Poisson's equation. We treat the semiconductor in the depletion approximation with fully

ionized donors, matching the electric displacement vectors at the vacuum-semiconductor interface. Assuming no significant surface-state charge density, this yields

$$V_d(s,V) = \Delta\phi \{[\, 1 + (s/s_0)^2 + V/\Delta\phi \,]^{1/2} - s/s_0\}^2, \qquad (1)$$

where s is the separation between the metal and the semiconductor. $\Delta\phi$ serves as a natural voltage scale for the surface potential, while $s_0 = (\varepsilon_0/\varepsilon_s)W(\Delta\phi)$ provides a natural length scale for the vacuum gap width. Here, $\varepsilon_s/\varepsilon_0$ is the dielectric constraint of the semiconductor relative to vacuum, and $W(\Delta\phi)$ is the zero bias, zero-separation depletion width given by

$$W(\Delta\phi) = \left(\frac{2\varepsilon_s\Delta\phi}{qN_d}\right)^{1/2}, \qquad (2)$$

where q is the electronic charge constant and N_d is the semiconductor dopant density.

For fixed tip-sample separation, a negative voltage applied to the sample will result in an decrease in V_d. This is known as forward bias, since in most common metal-semiconductor contacts this is the direction of easy current flow. A positive sample bias, on the other hand, will result in an increase in V_d, which is known as reverse bias, since in this direction the current is rectified. When the external bias exactly compensates for the difference in work functions ($V = -\Delta\phi$), then $V_d = 0$. This is the flat-band condition.

In considering the separation dependence of the diffusion potential, what we find is that V_d decreases with increasing vacuum gap width. As the ratio s/s_0 approaches zero, which is the regime of negligible tip-sample separation, or of very light semiconductor doping, all of the voltage drop occurs in the semiconductor. This is the ideal Schottky barrier limit. Alternatively, when s/s_0 becomes infinite, either at very large tip-sample separations or at very high doping, the entire voltage drop occurs in the vacuum region. Figure 2 illustrates the scaled functional dependence of V_d on s and V.

The magnitude of V_d is of central importance to the current conduction in non-degenerately doped MIS structures. Current conduction in these junctions is conventionally thought to be described by a thermionic emission process, which can be written as[5]

$$I = I_s \exp[-qV_d(s,V)/kT] \{1 - \exp[qV/kT]\}. \quad (3)$$

This equation describes a two-step process in which the majority carriers in the semiconductor must first possess enough thermal kinetic energy normal to the interface to surmount V_d and reach the surface before they can tunnel through the vacuum barrier. This picture ignores any contribution to the current from carriers tunneling through the semiconductor space charge region of length W—justifiable, since typically $W \gg s$. The vacuum-tunneling term is given in the Wentzel-Kramers-Brillouin (WKB) approximation by,[6]

$$I_s = A^* T^2 \exp[-\phi_n/kT] \exp[-A\bar{\phi}^{1/2}s]. \quad (4)$$

Here $\bar{\phi}$ refers to the mean barrier height experienced by the tunneling electrons, $A = \sqrt{8m/\hbar^2} = 10.25\ \mathrm{eV}^{-1/2}\mathrm{nm}^{-1}$, and A^* is an effective Richardson constant.

Based on the thermionic emission expression of Eq. (3), the complete $I(s,V)$ surface can be mapped out. The emphasis here is on those cuts through the $I(s,V)$ surface that are commonly accessed in tunneling microscopy—current *versus* voltage at constant separation (I-V), current *versus* separation at constant voltage (I-s), and the logarithmic derivative of the current with respect to voltage ($d\ln I/ds$), which is typically related to the tunneling barrier height.

Current-Separation Characteristics

We first consider the predicted current-separation characteristics, since this is a cut through the $I(s,V)$ surface that was not readily accessible prior to the invention of

STM. In Fig. 3 we have plotted the I-s curves for the specific case of a planar, passivated, non-degenerate, n-type Si (111)/Au junction at small forward bias and three different sample dopings. Also plotted for comparison is the predicted I-s curve for the case where V_d is not a function of separation and the Fermi level is pinned at its zero separation position. The most striking feature, for the higher dopings at least, is an unexpected peak in the I-s plot. This is in contrast to the more familiar metal-insulator-metal contacts, or the MIS junction with a pinned Fermi level, where the exponential spatial decay of the sample and tip wave functions leads to an approximately exponential decay in the tunneling matrix element with increasing separation.

The peak in the I-s spectra can be understood in terms of the competing exponentials in the expression for the current density. At zero separation, all the curves in Fig. 3 have the same magnitude of tunneling current since in this case, $V_d = \Delta\phi + V$, independent of doping. As the separation between the metal and semiconductor is increased, an exponential decrease in the vacuum tunneling probability is expected. Concomitant with that, however, is a decrease in the semiconductor diffusion potential because of the doping and separation-dependent distribution of the total field between the semiconductor and vacuum regions through the parameter s/s_0. The decrease in V_d will lead to an exponential *increase* in the population of carriers at the semiconductor surface available for tunneling. The competition between the exponentially increasing thermal population factor and the exponentially decreasing tunneling factor is what gives rise to the unusual current-separation behavior. This competition will always lead to a decrease in the rate of decay of the current with increasing separation. For higher sample dopings and narrower gap widths where the decrease in V_d with increasing separation is more rapid (the s/s_0 dependence in Fig. 2), an actual increase in the current with increasing separations is expected. As the separation continues to increase and the surface diffusion potential decays to zero, the tunneling factor will again inevitably win out, and the

familiar asymptotic behavior dominated by the exponential decay in the tunneling probability will be seen.

Apparent Barrier Height

Measurements of tunneling barrier heights using the STM have received some attention in recent years,[7,8] partly because of the unique ability of the STM to probe the tunneling current as a function of a precisely controllable separation that is not averaged over the surface. Contamination-mediated barrier reductions are well known in surface science, and have been seen in STM experiments as well.[9] A certain barrier lowering is expected even at ideal interfaces with no surface dipole, because of the electrostatic attraction of the tunneling charge carrier to its multiple images in the conductors. At small separations, an additional contribution that is due to exchange-correlation effects is expected.[8]

Following Lang,[8] we here define the apparent barrier height, ϕ_A, for tunneling in STM as

$$\phi_A = [(-1/A)\, d\ln I/ds]^2, \tag{5}$$

based on the expectations for a one-dimensional square barrier. This is typically measured in STM experiments by a modulation of the gap separation with phase-sensitive detection of the current at the modulation frequency.

For an unpinned semiconductor, the fraction of the applied bias which drops in the semiconductor is a sensitive function of the gap spacing. Modulation of the tip-sample separation therefore inevitably modulates the surface potential as well. For the thermionic emission formulation of Eq. (3), one finds that[10]

$$d\ln I/ds = -A\bar{\phi}^{1/2} - \frac{q}{kT}[dV_d/ds]. \tag{6}$$

Since the surface potential decreases with increasing separation, we find that the new term in Eq. (6) is the opposite sign of the familiar tunneling contribution. Thus, one predicts that STM measurements of ϕ_A at unpinned semiconductor surfaces will yield low values. This can be seen graphically by examining the slope of the I-s curves in Fig. 3.

Figure 4 is a plot of the apparent barrier height expected for an ideal MIS junction as a function of separation based on Eqs. (3) and (6). These curves are plotted for the same dopings and tunnel bias as Fig. 3. Once again, we have included for comparison the prediction for the case in which the distance dependence of the V_d is artificially disabled. As expected, the *apparent* barrier heights as defined in Eq. (6) are dramatically lowered. This lowering persists to large separations, especially for the more lightly doped semiconductors, since dV_d/ds continues to be a significant factor at larger distances in this case. For high doping levels and small separations, there is a sign change in the *apparent* inverse decay length (if one were to interpret the I-s characteristics without considering thermal-population contributions) since the current is an increasing function of the separation.

Current-Voltage Characteristics

The other effect of metal-induced band bending which we will consider here is a modification of the current-voltage curves. The I-V characteristics of metal-semiconductor contacts and MIS junctions have been extensively studied.[11] It is well known that a lightly doped, ideal semiconductor in intimate contact with a metal will usually produce rectified I-V curves. Higher doping or an interfacial oxide layer begins to soften the knee of the rectified curve, and eventually a symmetric or reverse rectified I-V may be observed.

In an STM experiment, the precisely controllable tunnel gap spacing gives an additional degree of freedom whose functional dependence can be investigated. As seen in Eq. (1), the change in separation causes a change in V_d analogous to that which

would be caused by a change in the doping level, through the factor s/s_0. Figure 5 shows the predicted I-V curves for a single doping level at four different separations. The current magnitude at the different separations varies widely, as was already seen in Fig. 3; therefore, for comparison purposes the curves are all scaled by the magnitude of their current at -0.25 V.

When the tip and sample are in contact, the familiar Schottky diode behavior is found. At negative sample bias, the thermal activation barrier, which is the offset of the conduction band edge at the semiconductor surface from the semiconductor Fermi level, is equal to $V_d+\phi_n$. For an ideal metal-semiconductor contact, V_d decreases linearly with the applied bias, resulting in an exponential increase in I. At positive sample bias, on the other hand, the electrons are flowing from metal to semiconductor, and the thermal activation barrier is the offset of the conduction band edge at the semiconductor surface from the Fermi level of the *metal*—in the notation of Fig. 1, V_b. In the zero-separation limit, this offset is known as the Schottky barrier height and it is simply equal to $\Delta\phi$ independent of bias. This means that increasing the sample bias results in no increase in the current beyond the saturation limit, proportional to $\exp[-q\Delta\phi/kT]$. The I-V curve is therefore negatively rectified.

As the separation is increased, the negative rectification of the junction is seen to decrease, with the shape of the curve eventually passing through symmetric to reverse rectification. This can be understood on the basis of the decreasing bias dependence of V_d with increasing separation [Eq. (1)]. In forward bias, this decreased sensitivity of V_d to V is directly reflected in the thermal activation barrier, leading to a softer current turn-on. In reverse bias, the thermal activation barrier is given by $V_b=V_d+\phi_n-V$. The decreased dependence of V_d on V will therefore lead to a decrease in V_b with increasing bias, and hence an increasing current. For large enough s/s_0, $V_b(V_m)$ becomes less than $V_d(-V_m)+\phi_n$, where V_m is the maximum voltage of a symmetric

bias sweep. Beyond this point, the I-V curves will begin to appear reverse-rectified. This relationship between thermal activation barriers for forward and reverse currents can be reduced to the expression $[V_d(+V_m) - V_d(-V_m)]/V_m$, which is plotted in Fig. 6 as a function of $V/\Delta\phi$ with s/s_0 as a parameter. Values greater than one correspond to normal rectification, and values less than one to reverse rectification. We see from the figure that the condition for reversal of rectification is met when s/s_0 reaches a value between 0.5 and 0.6, depending on the magnitude of the voltage sweep.

Note that as the separation and the magnitude of the reverse bias are increased, V_b will eventually become less than zero, meaning that the Fermi level in the metal has crossed the conduction band edge of the semiconductor. As this point is neared, Eq. (3) is no longer a valid description of the current, since the Maxwell-Boltzmann statistics used to approximate the thermal population are an accurate description of the Fermi distribution only for $E-E_F>3kT$. Also, as a result of the depletion approximation, the range of validity in negative sample bias extends only to $-\Delta\phi$.

Description of Calculation

To test the quantitative reliability of these phenomenological predictions, and to assess the significance of any tunneling through the semiconductor space-charge region for these moderately doped semiconductors, we have also formulated a more complete quantum mechanical treatment. The calculational approach involves the numerical solution of a one-dimensional (1D) Schrödinger equation in the effective mass approximation. The method also avoids the use of the WKB approximation and allows for such intrinsically quantum mechanical effects as reflection at a potential step.

The space-charge potential is computed in the depletion approximation. It is parabolic in x, the direction normal to the vacuum interface, decaying from V_d at the semiconductor surface to zero at $x = -W$ in the bulk. The vacuum barrier is taken to be trapezoidal, and the metal is treated as a free-electron Fermi gas. Image-potential effects

are ignored. For the case of MIM tunneling, it has been shown that image-potential effects cancel to first order in measurements of $d\ln I/ds$.[7] Neglecting the barrier lowering that is due to the image potential will, of course, decrease the total amplitude of the current, but the qualitative trends in the distance-dependence are expected to be unchanged.

The semiconductor is modeled in a one-band, many-valley, effective mass approximation, including anisotropy. The indirect conduction band minima in silicon lie along the six equivalent <100> directions in the Brillouin zone, and the constant-energy surfaces are ellipsoidal. Following Stratton and Padovani,[12] the anisotropic effective mass equation is reduced to an equivalent 1D Schrödinger equation for motion through the semiconductor in the [111] direction. Because of the symmetry of this axis, the equation is identical for all six ellipsoidal pockets. We assume that the single-band effective mass computed for allowed conduction band states also properly describes tunneling through the space-charge region. This equation is then solved by discretizing the position-dependent electron potential energy into a series of piecewise linear segments and by employing matrix methods to calculate the overall transmission probability.[13] Note that the appropriate wave-function derivative matching at the boundaries must include $1/m^*$ because of the discontinuities in the effective mass.[14]

Equilibrium distribution functions at finite temperature are used for electron in both metal and semiconductor. This lifts the previous restriction that $V_b>0$. The phase-space summation, conserving energy and transverse momentum, reduces to a single, unrestricted integral, provided that the transmission coefficient D depends only on E_x, the energy component normal to the barrier.[15] The net current density is then given by the expression

$$j = \frac{qm_t}{\gamma^{1/2} m_0} \int_0^\infty dE_x D(E_x)[N_0(E_x) - N_0(E_x - qV)], \qquad (7)$$

where N_0 is the 1D supply function[16] for electrons in the semiconductor and metal, respectively, while γ is the anisotropy factor for Si <100> ellipsoidal pockets projected along the [111] direction.

Results

Computations based on Eq. (7) reveal that thermally-activated tunneling through the semiconductor space-charge region is responsible for most of the observed current at these moderate doping levels. This effect is illustrated in Fig. 7 for $N_d = 5 \times 10^{18}$ cm^{-3}, which corresponds to the doping levels used in Ref. 3. The current distribution, as a function of the energy component normal to the barrier, peaks well below the top of the semiconductor space-charge region potential barrier for all the distances of interest. The inset shows how the fraction of total current arising from thermionic emission always remains small. There are two reasons for this. First, the effective mass for tunneling in the [111] direction is small, $m_x = 0.26\, m_0$. Second, and more importantly, V_d is enormous on the scale of kT (*e. g.*, several hundred meV), so that despite relatively long depletion widths, tunneling through the space charge is favored.

This new avenue for current conduction relative to the non-quantum-mechanical treatment changes the magnitude, but not the general trends, of the separation-dependent effects described above. In the *I-s* curves, the peak in the current is shifted to smaller separations, as illustrated in Fig 8. This is because the current contribution that is due to electrons penetrating the space-charge barrier is scaled in its sensitivity to V_d, which tends to mitigate the dV_d/ds dependence of the overall current-separation behavior.

For the same reason, the apparent barrier heights deduced from these curves are not lowered as much as they were before the space-charge tunneling contributions were included (relative to the expectations based on ignoring band-bending effects). This is especially true at the higher doping levels where the depletion widths are smaller and the surface potential drops off more quickly with separation, as shown in Fig. 9.

Nevertheless, because of tip-induced band-bending effects, there is still a very definite lowering of ϕ_A for conditions in which STM experiments could easily be performed.

The apparent barrier height is also expected to have a unique voltage signature because of the bias dependence of the diffusion potential. This is illustrated in Fig. 10 for several different bias voltages, using the same doping density. By examining this functional relationship, barrier lowering that is due to tip-induced band bending can be conveniently distinguished from that which is due to image-potential or exchange-correlation effects. Examination of the apparent barrier height as a function of separation and bias could also, in principle, provide a sensitive experimental means of measuring the local value of $\Delta\phi$, and hence the local semiconductor doping level.

In the *I-V* curves, the major trend predicted from the MIS phenomenology is for the sign of the current rectification to reverse as the separation increases from contact. This reversal will always occur at a great enough separation (as $s/s_0 \rightarrow \infty$), though for more lightly doped semiconductors, the distances can easily become prohibitive for measurements of tunneling currents. When the current that is due to thermionic field emission through the diffusion-potential barrier is included in the estimate of the total current, it is found that this reversal in rectification will occur at a smaller separation. This is illustrated in Fig. 11, which is a plot of *I-V* curves including the space charge tunneling contribution at the same separations and doping as used in Fig. 5. We see that at a 0.5 nm separation, for example, the inclusion of a space-charge tunneling contribution changes the character of the *I-V* from forward-rectified to symmetric. This trend can be understood on the basis of the parabolic penetration of the field into the semiconductor space-charge region. Since the field is greater for reverse bias, the width of the space-charge region through which an electron must tunnel is decreased. This leads to a relatively greater contribution of the space-charge tunneling component of the current for reverse bias than for forward bias.

The description presented here of the distance dependence of the current conduction MIS structures has focused on *n*-type semiconductors in depletion. However, the analogous situation for *p*-type semiconductors in depletion (where in this case, $\phi_m<\phi_s$) is also described by the same thermionic emission equation, the majority carriers in this case being the holes. The trends predicted for the separation dependence of the current, as well as implications for ϕ_A and the *I-V* characteristics, should therefore be the same.

Conclusions

The separation dependence of the surface diffusion potential in MIS structures leads to some interesting effects that can be conveniently measured using an adjustable vacuum-gap tunneling device such as the STM. We have presented a model for an ideal (unpinned) semiconductor surface in depletion. What we find is that depending on a scaling which is a function of semiconductor doping and dielectric constant, it may be possible to observe a peak in the *I-s* curves at small separations. We also predict a substantial lowering of the apparent barrier height as deduced from the slope of the *I-s* curves, relative to the barrier heights expected for metal-metal or metal–pinned-semiconductor tunneling. The functional relationship between the current and the separation is sample-bias-dependent, and so any lowering of the apparent barrier height should be easily distinguishable from other barrier-lowering mechanisms.

The same relationship for the current as a function of voltage and separation also leads to some interesting effects in the measured *I-V* characteristics. As the separation increases relative to the same scaling factor as before, the *I-V* curves are found to switch from the usual Schottky-barrier–type rectification, through a regime where conductivity is similar at both biases, to a complete reversal of rectification.

These effects are all predicted on the basis of the conventional theory of MIS structures which includes only those contributions to the current that are due to thermionic emission of carriers over the semiconductor diffusion-potential barrier. For the moderately high doping levels considered here (and those typically used in STM experiments), a more complete quantum mechanical treatment shows that the majority of the current is due to electrons that tunnel through the semiconductor space-charge region. Including this new avenue of current conduction leads to a shift of the predicted peak in the *I-s* curve to smaller distances, where the approximations we have made may break down. The slope of the *I-s* curve is also changed, leading to a lesser, but still easily observable, lowering of the apparent barrier height. In the *I-V* curves, on the other hand, the new contribution to the total current results in a decrease in the separation at which reversal of rectification will be seen at a given doping level, rendering these effects even more accessible to STM experiments than previously believed.

References

§ *Portions of this chapter have been published as*: M. Weimer, J. Kramar, J. D. Baldeschwieler, *Phys. Rev.* **B 39**(8), 5572–5 (1989).

1. J. van Laar, A. Huijser, T. L. van Rooy, *J. Vac. Sci. Technol.* **14**(4), 894–8 (1977); L. J. Brillson, R. E. Viturro, C. Mailhiot, J. L. Shaw, N. Tache, J. McKinley, G. Margaritondo, J. M. Woodall, P. D. Kirchner, G. D. Pettit, S. L. Wright, *J. Vac. Sci. Technol.* **B 6**(4), 1263–9 (1988).
2. E. Yablonovich, D. L. Allara, C. C. Chang, T. Gmitter, T. B. Bright, *Phys. Rev. Lett.* **57**(2), 249–52 (1986).
3. L. D. Bell, W. J. Kaiser, M. H. Hecht, F. J. Grunthaner, *Appl. Phys. Lett.* **52**(4), 278–80 (1988); W. J. Kaiser, L. D. Bell, M. H. Hecht, F. J. Grunthaner, *J. Vac. Sci. Technol.* **A 6**(2), 519–23 (1988).
4. S. M. Sze, *Physics of Semiconductor Devices*, Wiley, New York (1981).
5. Originally derived by H. Bethe for MS contacts: *see* V. L. Rideout, *Thin Solid Films* **48**, 261–91 (1978).
6. H. C. Card, E. H. Rhoderick, *J. Phys. D: Appl. Phys.* **4**, 1589–1601 (1971); *ibid.*, 1602–11 (1971).
7. G. Binnig, N. García, H. Rohrer, J. M. Soler, F. Flores, *Phys. Rev.* **B 30**(8), 4816–8 (1984); J. H. Coombs, M. E. Welland, J. B. Pethica, *Surf. Sci.* **198**, L353–8 (1988).
8. N. D. Lang, *Phys. Rev.* **B 37**(17), 10395–8 (1988).
9. G. Binnig, H. Rohrer, Ch. Gerber, *Appl. Phys. Lett.* **40**(2), 178–80 (1982); D. W. Abraham, H. J. Mamin, E. Ganz, J. Clarke, *IBM J. Res. Develop.* **30**(5), 492–99 (1986).
10. This ignores a further small correction term that is due to the change in the mean barrier height with gap spacing.
11. E. H. Rhoderick, *Metal-Semiconductor Contacts*, Clarendon, Oxford (1980).

12. R. F. Stratton, F. A. Padovani, *Phys. Rev.* **175**, 1072–6 (1968).

13. W. W. Lui, M. Fukuma, *J. Appl. Phys.* **60**(5), 1555–9 (1986).

14. D. J. BenDaniel, C. B. Duke, *Phys. Rev.* **152**, 683–92 (1966).

15. Strictly speaking, the mass discontinuity at the vacuum-semiconductor interface couples the normal and transverse energy components. Following the usual approach in tunneling theories of Schottky barrier structures, we presume that this is a small correction and that D depends only on E_x. [see, *e. g.*, W. J. Boudville, T. C. McGill, *J. Vac. Sci. Technol.* **B 3**, 1192–6 (1985)].

16. C. B. Duke, *Tunneling in Solids*, Academic, New York (1969) (supplement 10 of series *Solid State Physics*, edited by F. Seitz, D. Turnbull, H. Ehrenreich).

Figure 1

Electron potential energy diagram for an ideal metal-insulator-semiconductor junction in the absence of an external bias voltage. Band bending is observed near the semiconductor-insulator interface that is due to incomplete shielding of the external field at the semiconductor surface. Note that the drawing is not to scale, since typically $W \gg s$.

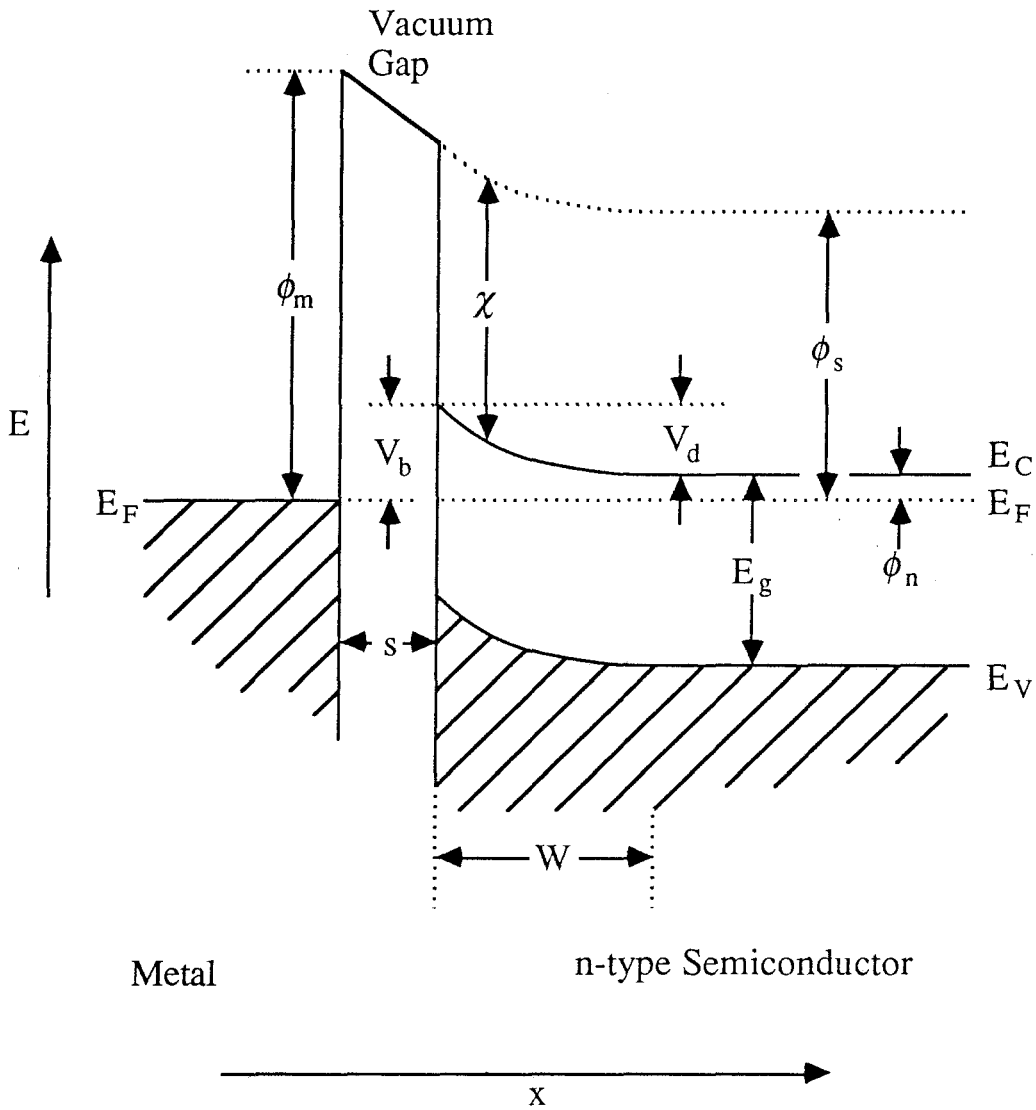
Vacuum
Gap
ϕ_m
χ
ϕ_s
E
V_b
V_d
E_C
E_F
E_F
E_g
ϕ_n
s
E_V
W
Metal
n-type Semiconductor
x

Figure 2

Scaled functional dependence of the semiconductor surface-diffusion potential on the tip-sample separation and the sample bias.

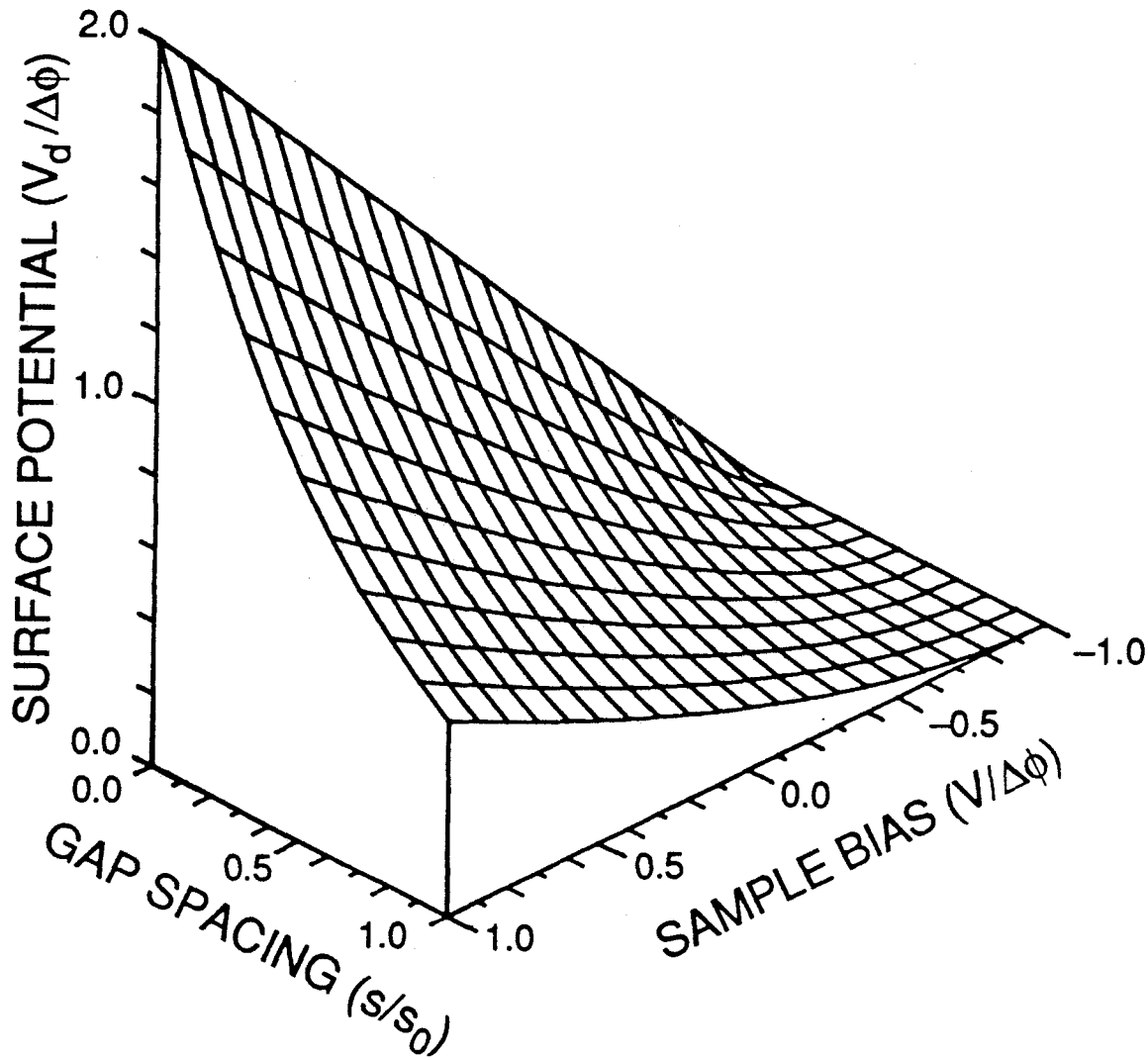
SURFACE POTENTIAL ($V_d/\Delta\phi$)
2.0
1.0
0.0
0.0
0.5
1.0
GAP SPACING (s/s_0)
1.0
0.5
0.0
−0.5
−1.0
SAMPLE BIAS ($V/\Delta\phi$)

Figure 3

I-s curves as a function of semiconductor doping, showing the separation-dependent effects of the surface diffusion potential on the thermionic current in an Au/*n*-type Si (111) system. Shown for comparison is the predicted *I-s* curve when the Fermi level is pinned at its zero separation value so that the V_d is not a function of s. Absolute current is arbitrary, and T=300 K, ϕ_m=5.1 eV, and χ=4.3 eV. A small negative sample bias of −100 mV is used throughout.

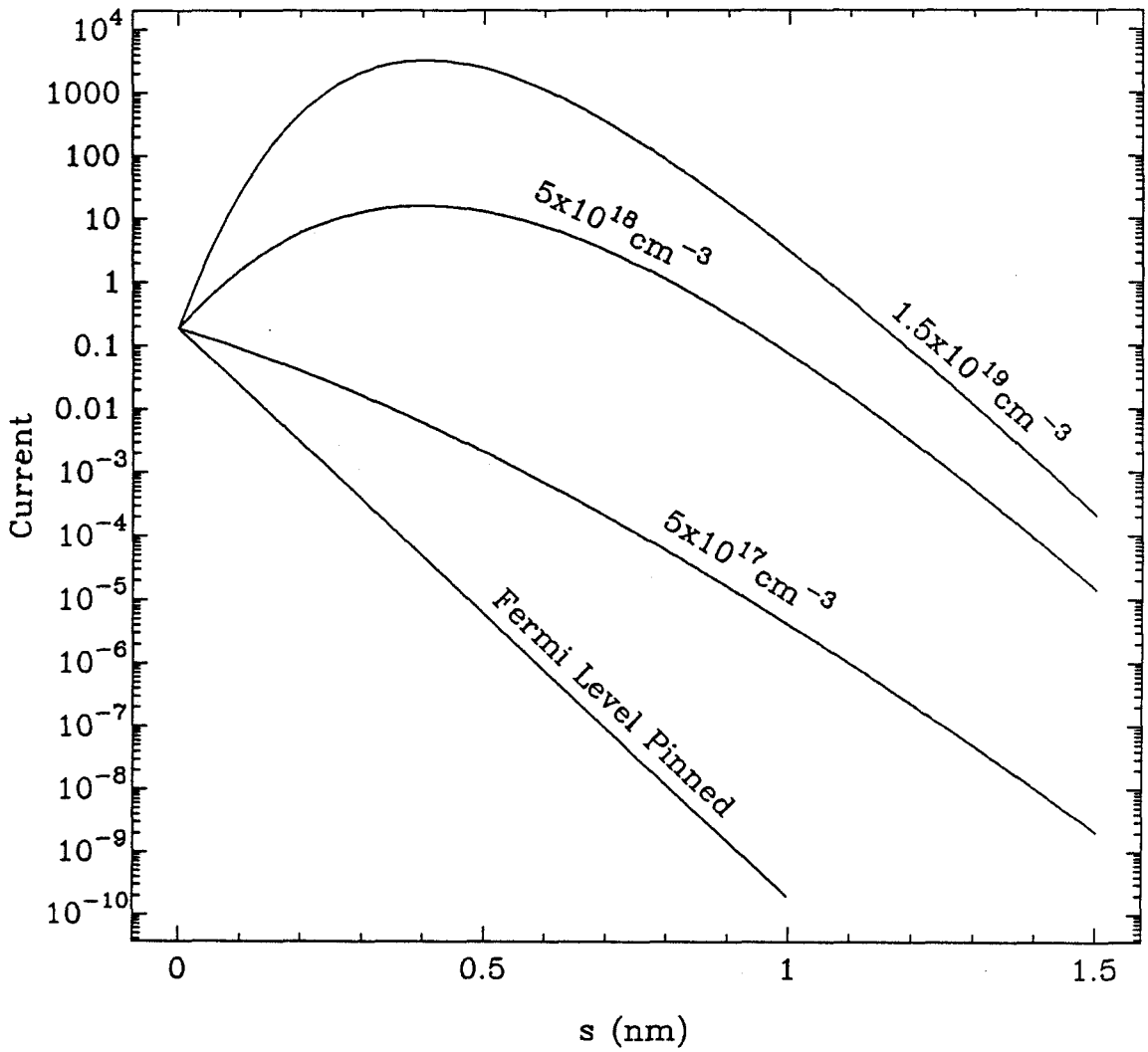
Current
s (nm)
5x10^18 cm^-3
1.5x10^19 cm^-3
5x10^17 cm^-3
Fermi Level Pinned

Figure 4

Apparent barrier height *versus* tip-sample separation based on the curves shown in Fig. 3.

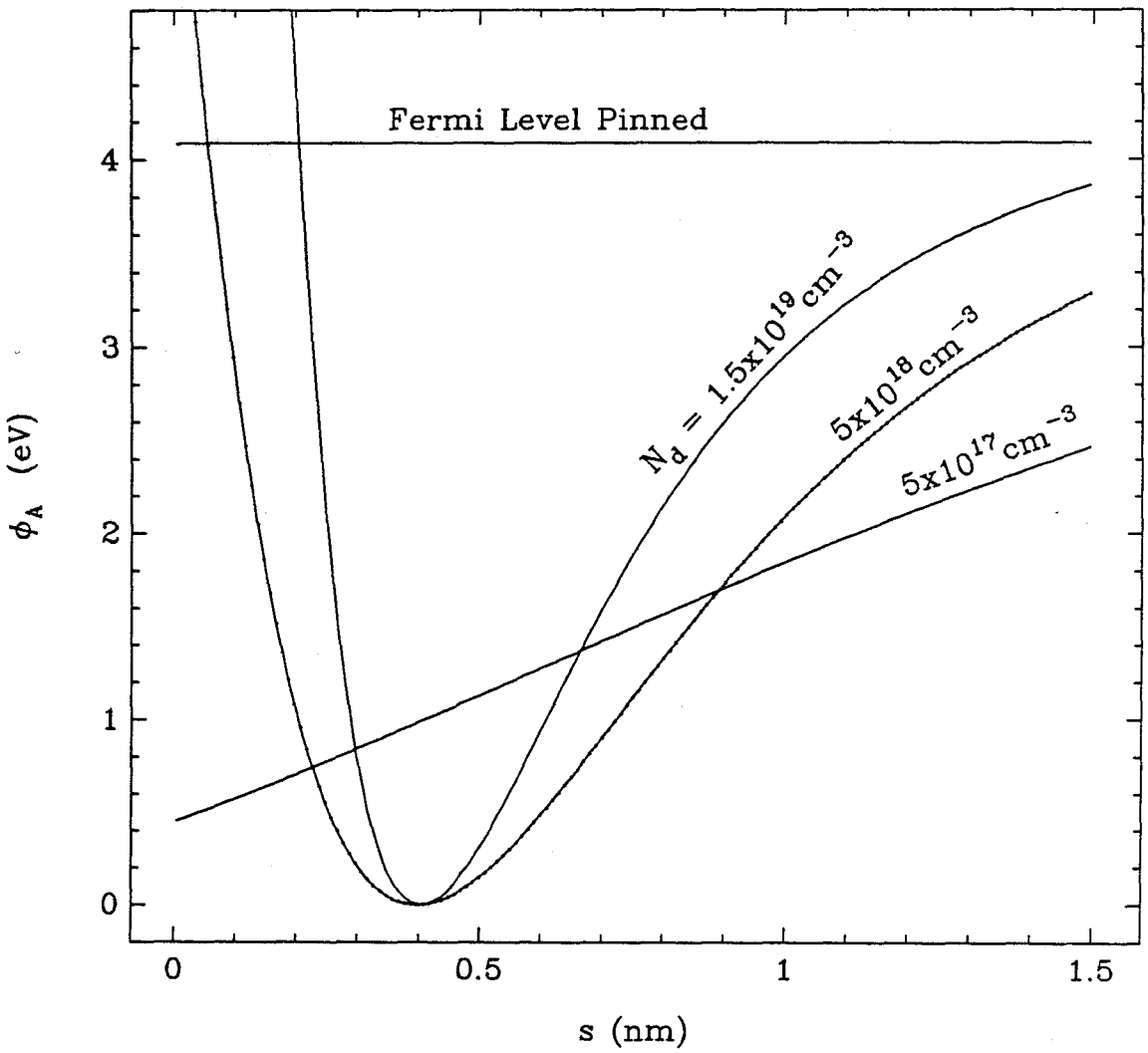
Fermi Level Pinned
$N_d = 1.5x10^{19}\,cm^{-3}$
$5x10^{18}\,cm^{-3}$
$5x10^{17}\,cm^{-3}$
ϕ_A (eV)
s (nm)
0
1
2
3
4
0
0.5
1
1.5

Figure 5

Current *versus* sample bias as a function of tip-sample separation for thermionic emission in an Au/*n*-type Si (111) system. The current is normalized to its value at –0.25 V sample bias. Semiconductor doping of 5×10^{18} cm^{-3} is used throughout.

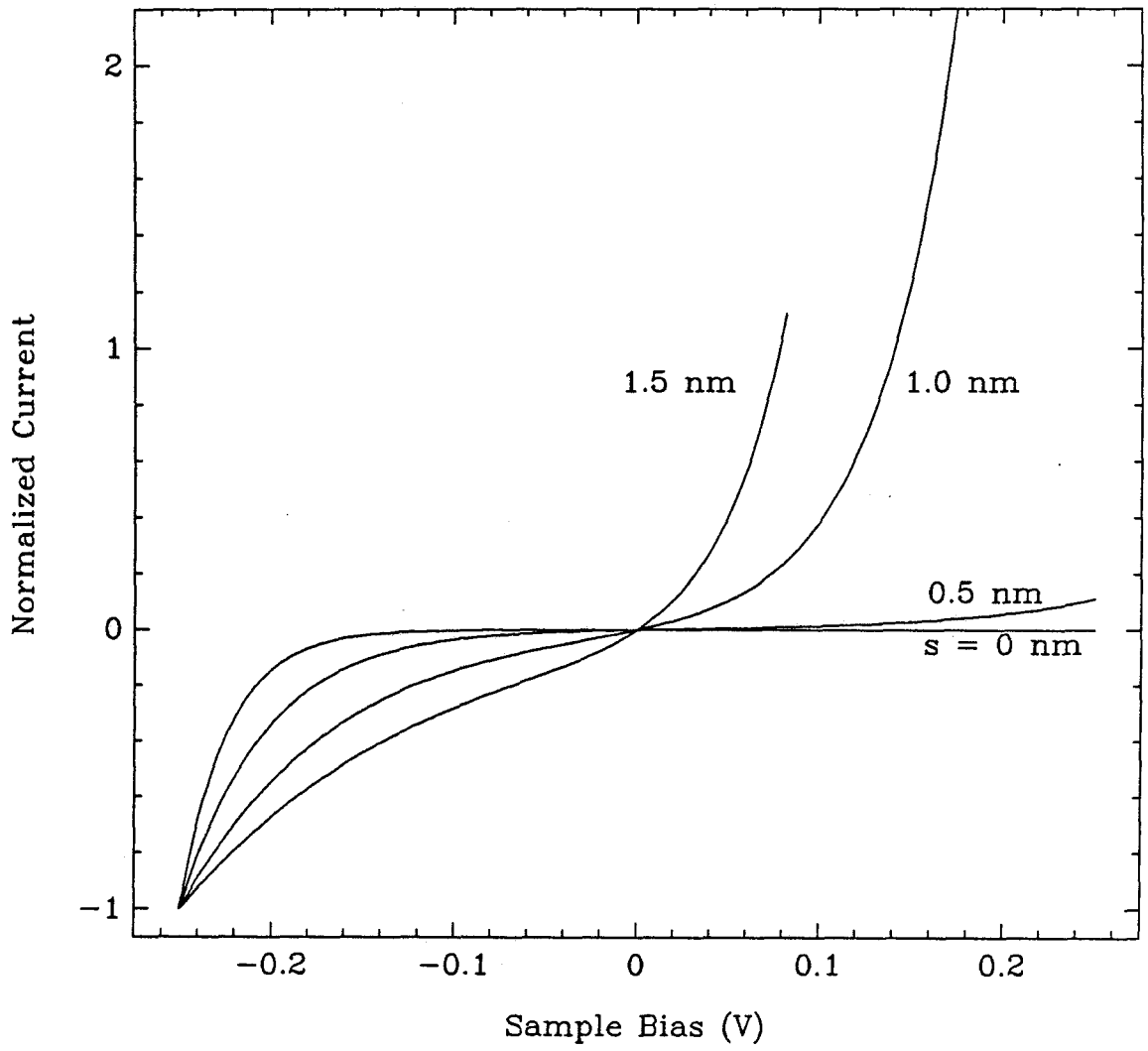
Normalized Current
2
1
0
−1
−0.2
−0.1
0
0.1
0.2
Sample Bias (V)
1.5 nm
1.0 nm
0.5 nm
s = 0 nm

Figure 6

The difference in surface diffusion potential for the same amplitude forward and reverse bias scaled by that amplitude, $[V_d(V_m) - V_d(-V_m)]/V_m$, plotted versus the magnitude of the bias (scaled by $\Delta\phi$), as a function of the scaled gap spacing (s/s_0). The magnitude of $[V_d(V_m) - V_d(-V_m)]/V_m$ is found to predict the sign of the bias at which the greater current will be measured for a symmetric voltage sweep of $\pm V_m$. Values greater than one result in normal rectification (higher current at negative sample bias for an *n*-type MIS structure) and values less than one will result in reverse rectification.

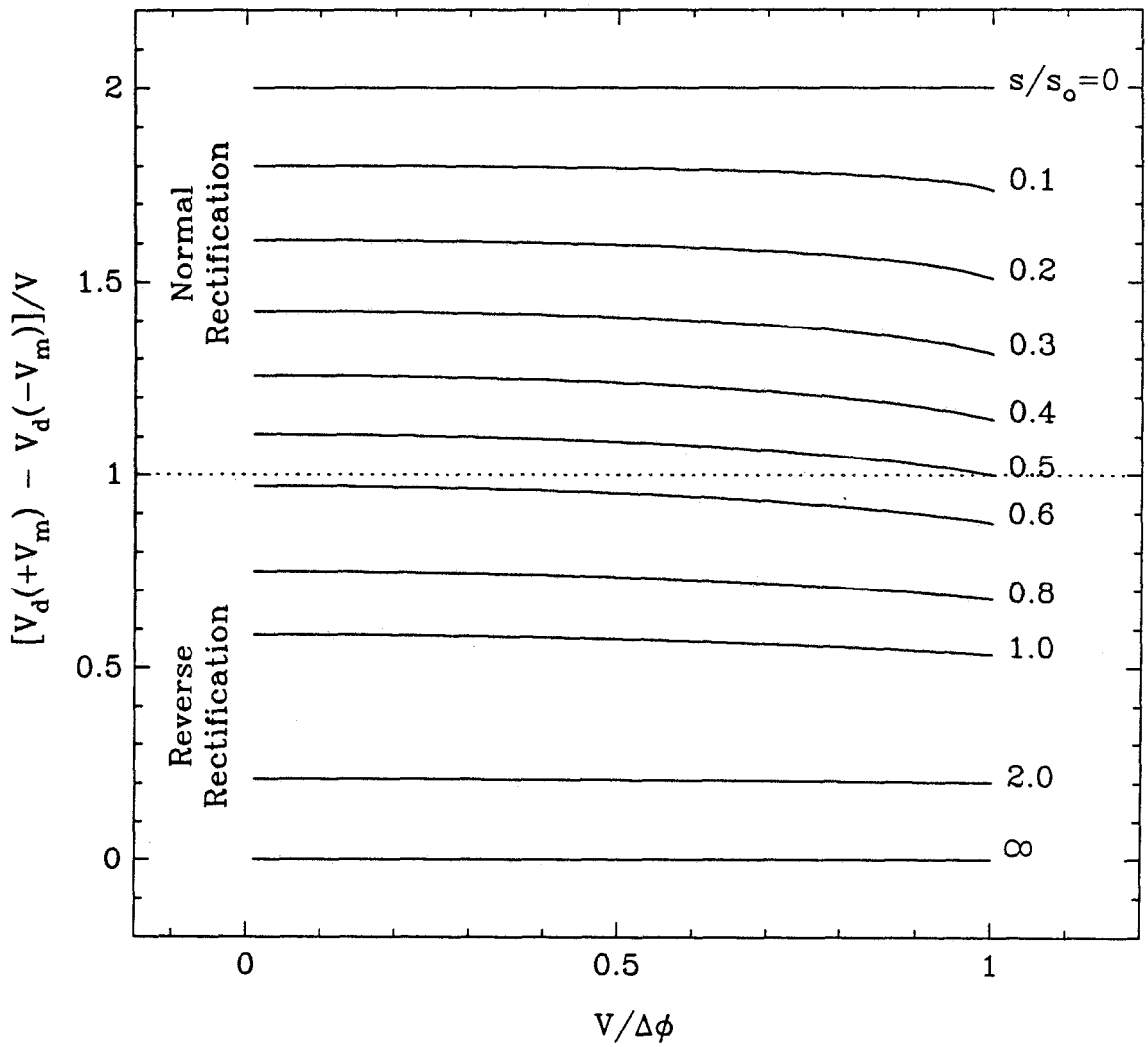
$[V_d(+V_m) - V_d(-V_m)]/V$
2
1.5
1
0.5
0
Normal Rectification
Reverse Rectification
$s/s_o=0$
0.1
0.2
0.3
0.4
0.5
0.6
0.8
1.0
2.0
∞
0
0.5
1
$V/\Delta\phi$

Figure 7

Differential current density distribution *versus* normal energy (relative to the semiconductor surface potential), as a function of tip-sample separation.

Inset: The thermionic contribution as a fraction of the total current density.

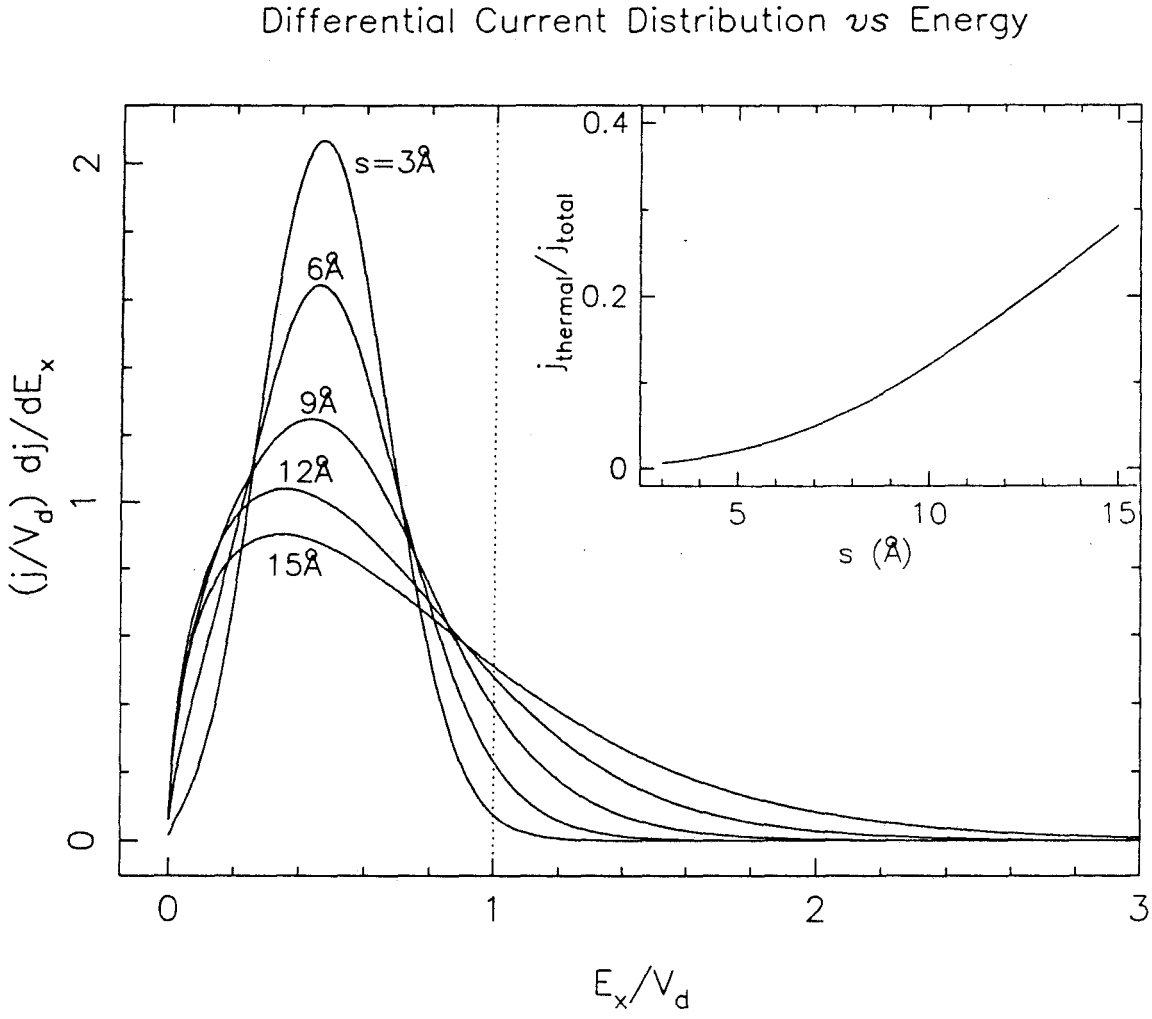
Differential Current Distribution vs Energy
s=3Å
6Å
9Å
12Å
15Å
(j/V_d) dj/dE_x
E_x/V_d
0
1
2
3
j_thermal/j_total
0.4
0.2
0
5
10
15
s (Å)

Figure 8

I-s curves as in Fig. 3 including the contribution to the total current that is due to tunneling through the semiconductor space charge region.

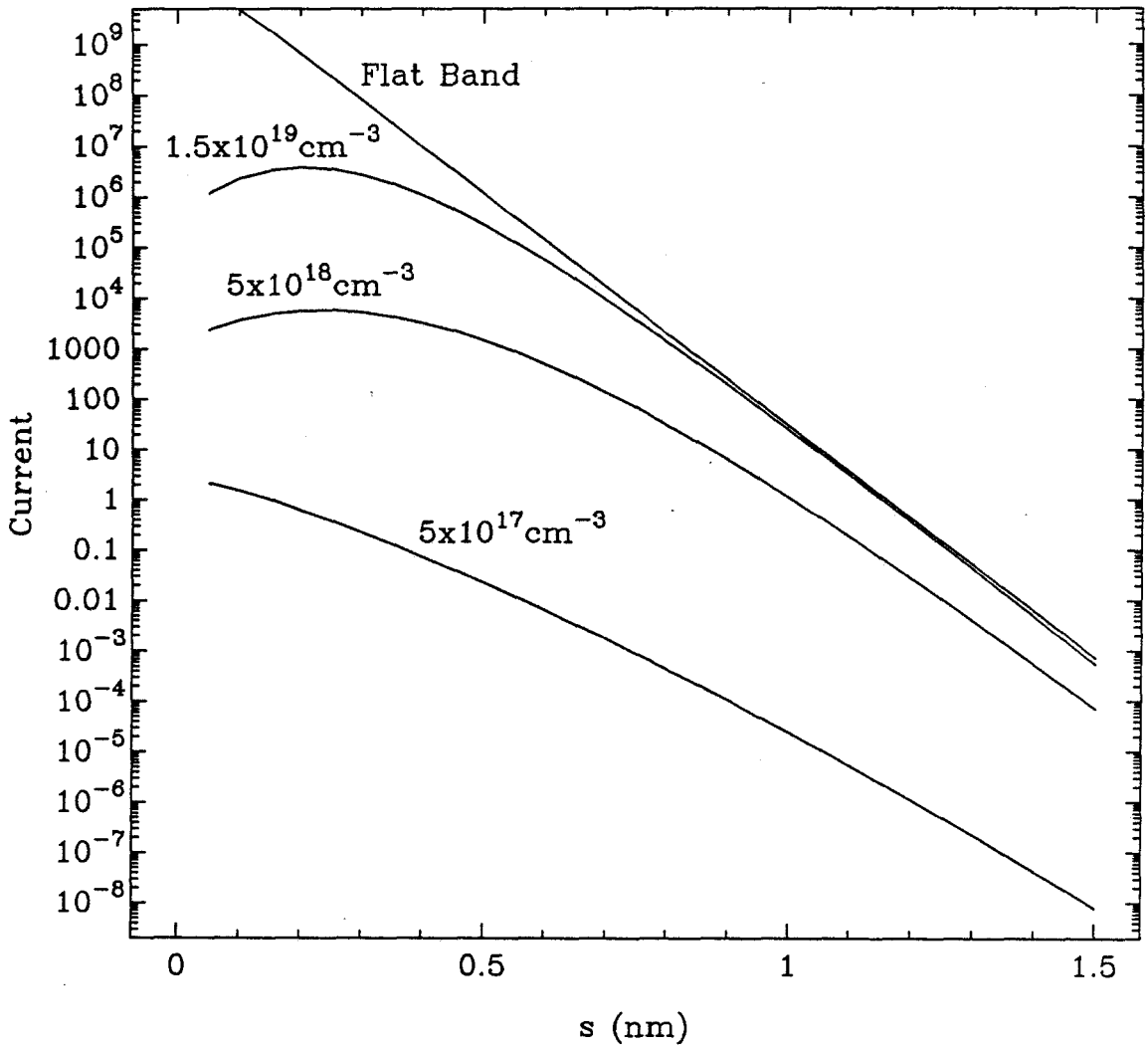
Flat Band
1.5x10^19cm^-3
5x10^18cm^-3
5x10^17cm^-3
Current
s (nm)
10^9
10^8
10^7
10^6
10^5
10^4
1000
100
10
1
0.1
0.01
10^-3
10^-4
10^-5
10^-6
10^-7
10^-8
0
0.5
1
1.5

Figure 9

Apparent barrier height *versus* tip-sample separation based on the *I-s* curves shown in Fig. 3.

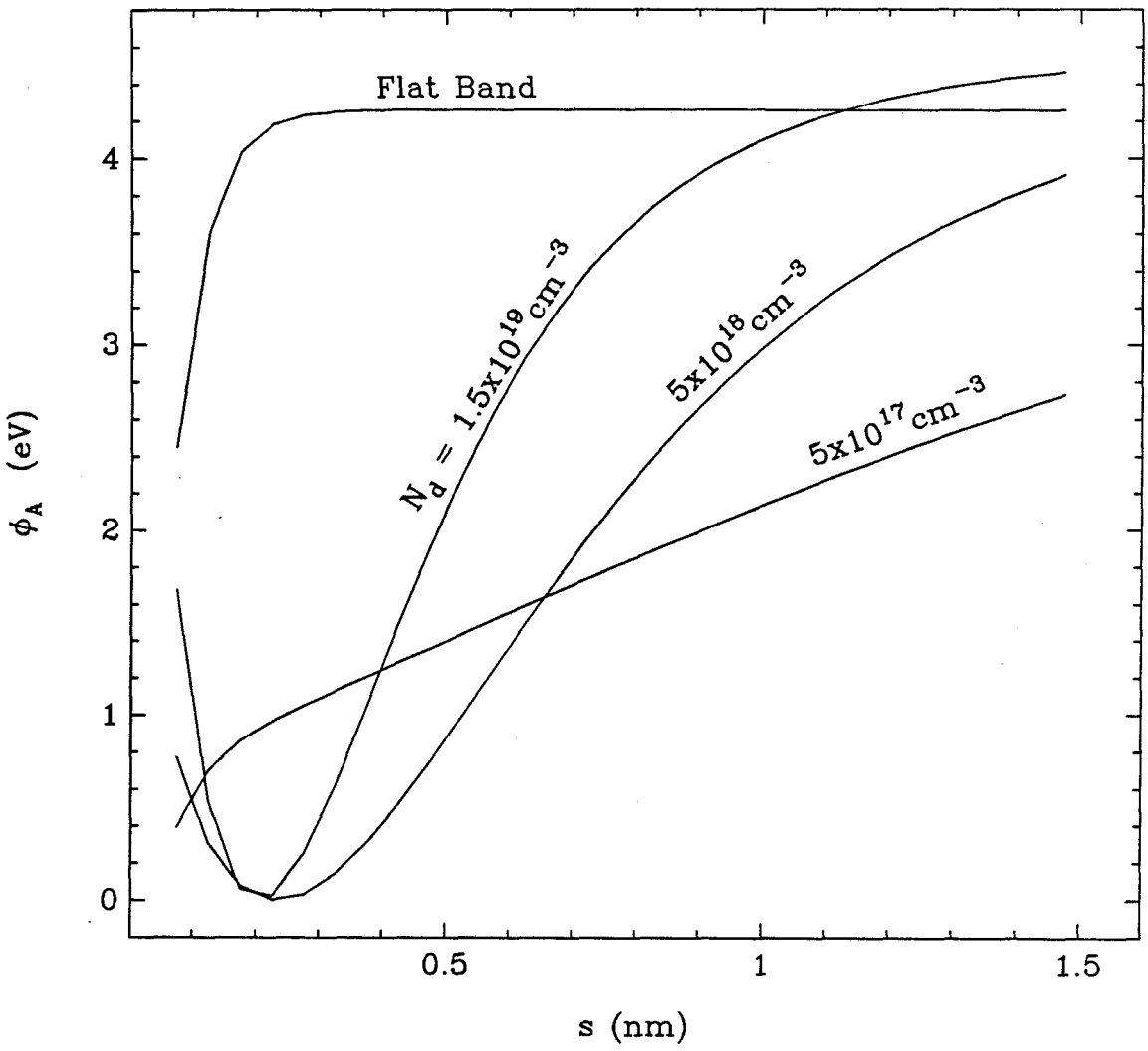
Flat Band
$N_d = 1.5x10^{19} cm^{-3}$
$5x10^{18} cm^{-3}$
$5x10^{17} cm^{-3}$
ϕ_A (eV)
s (nm)
0
1
2
3
4
0.5
1
1.5

Figure 10

Apparent barrier height *versus* tip-sample separation as a function of sample bias for a fixed doping of 5×10^{18} cm^{-3}, with tunneling through the semiconductor space-charge region included.

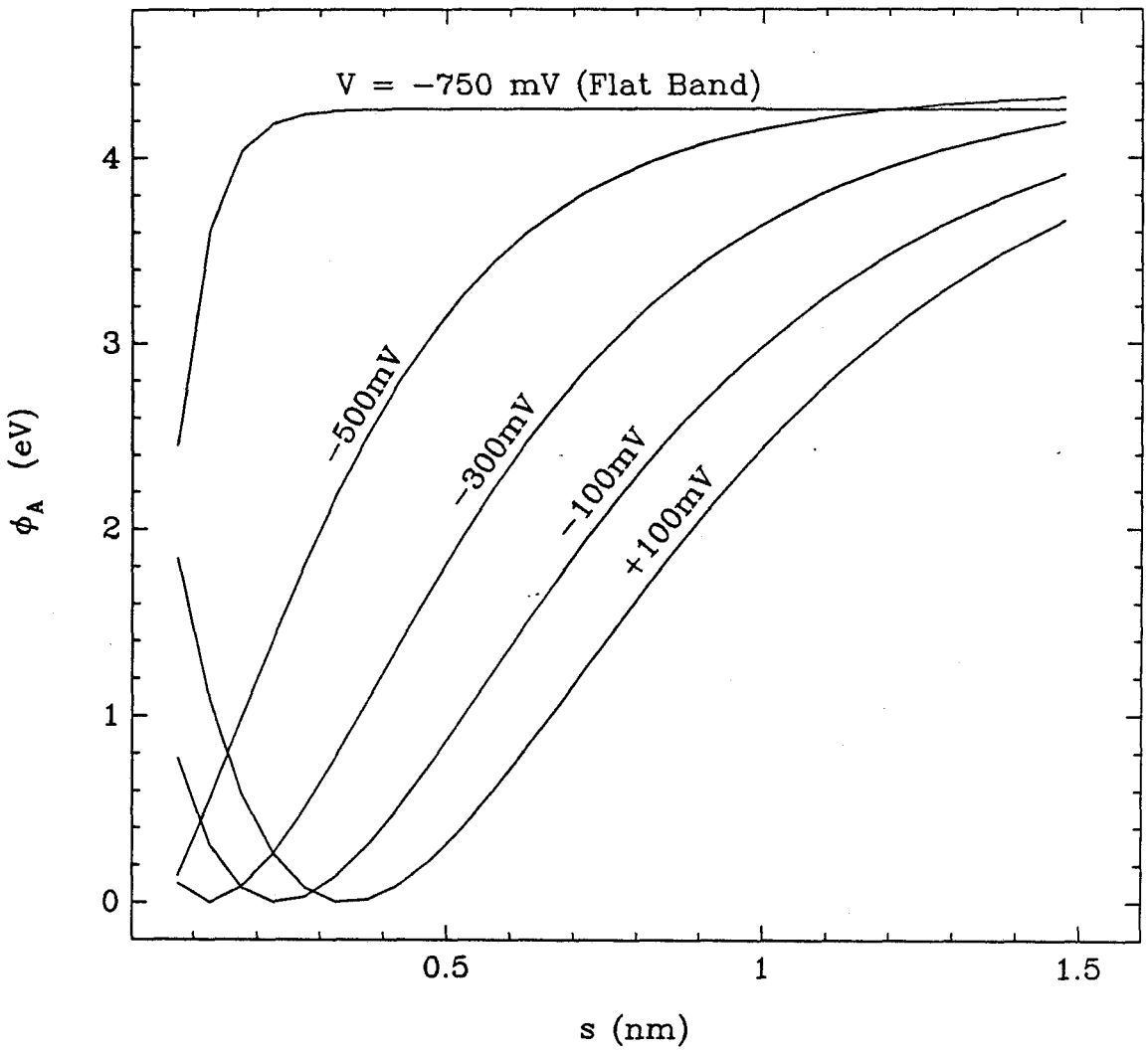
V = −750 mV (Flat Band)
−500mV
−300mV
−100mV
+100mV
ϕ_A (eV)
0
1
2
3
4
0.5
1
1.5
s (nm)

Figure 11

Current *versus* sample bias as a function of tip-sample separation for the same conditions as Fig. 5, but including the contribution to the current that is due to tunneling through the semiconductor space charge region.

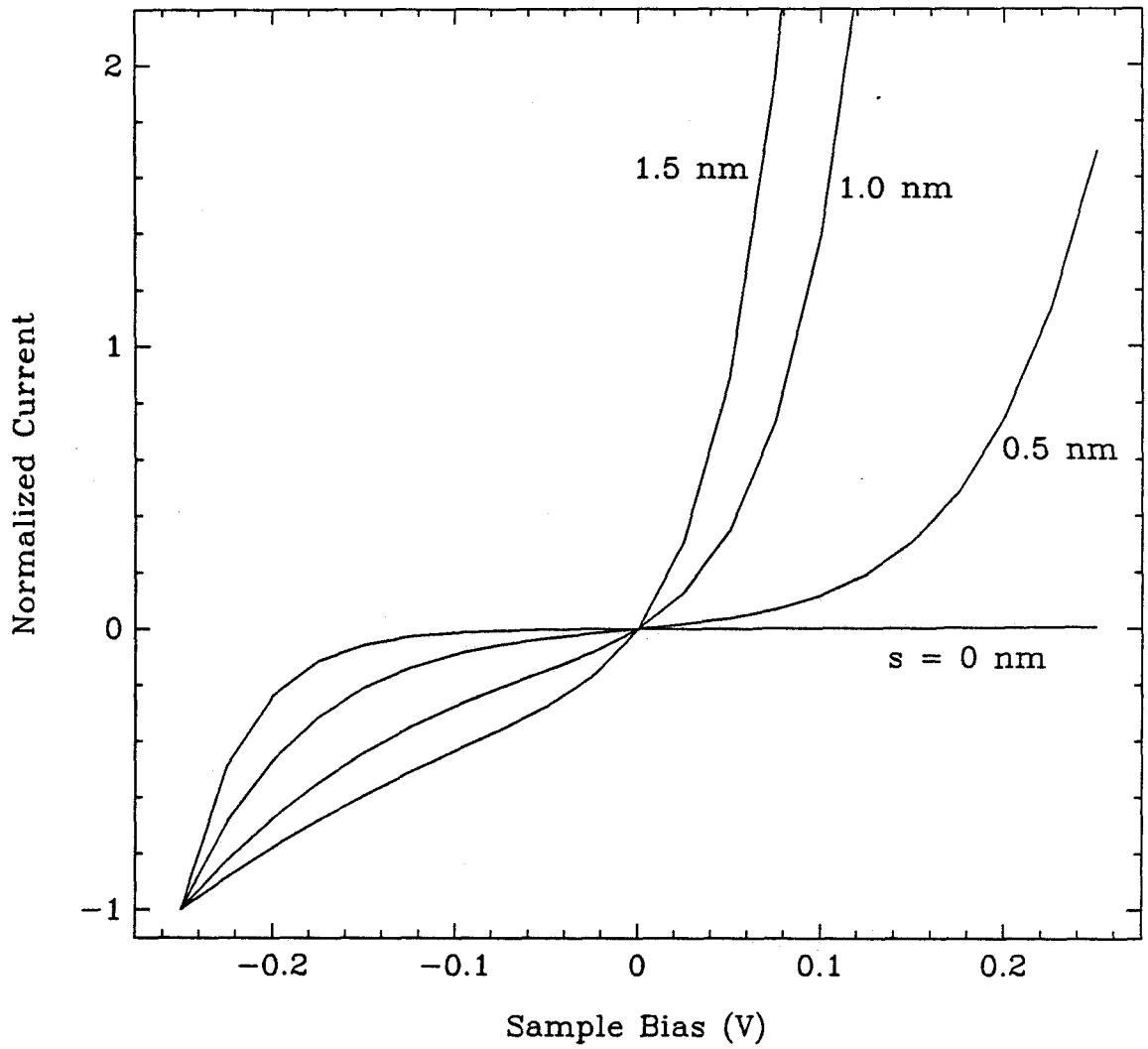
Normalized Current
2
1
0
−1
−0.2
−0.1
0
0.1
0.2
Sample Bias (V)
1.5 nm
1.0 nm
0.5 nm
s = 0 nm

Chapter 5

TUNNELING SPECTROSCOPY OF MOLYBDENUM DISULFIDE

Introduction

Measurements of the current-voltage characteristics of tunneling junctions have had an important history in solid-state physics. The recently demonstrated capability of forming controllable vacuum-gap junctions between any two conductors using the scanning tunneling microscope has led to a number of interesting new results. Evidence of surface states and other electronic structure has been seen in the tunneling spectroscopy of the previously inaccessible, clean crystalline surfaces of metals,[1] semiconductors,[2–5] and graphite.[6] The ability to measure the spatial variation of the tunneling spectra with the resolution of the STM has proven especially fruitful.[3,7]

In applications of the STM technique to problems of chemical interest, very often one would like to be able to establish the atomic or molecular identity of the surface feature under study. One of the most effective ways to approach this problem is by examining the electronic structure over that feature. On the GaAs (110) surface, for example, the regions of the surface with the highest density of filled states are correlated with the location of the As atoms, and the regions with the highest density of empty states are located in the vicinity of the Ga atoms.[8] Differences in the electronic structure are also seen between sites of the same atomic type in different bonding environments. This is what is found, for example, on the now classic Si (111) 7×7 surface.[2,3]

Molybdenum disulfide is an interesting semiconductor for tunneling spectroscopy for a variety of reasons. MoS_2 is perhaps the best known of the transition-metal dichalcogenides. These compounds typically crystallize in a layered structure, with strong covalent bonding within the planes and only a van-der-Waals attraction between planes. The crystal structure is described in more detail in Chapter 3. This weak interplanar bonding gives rise to the excellent lubricative properties of MoS_2. The electronic

properties also show a high degree of anisotropy. For example, the electrical conductivity parallel to the surface planes is about 10^3 times higher than it is perpendicular to the planes.[9]

The most interesting property from the point of view of tunneling spectroscopy, however, is a consequence of the highly ideal nature of the cleavage surface and its lack of dangling bonds. This leads to an absence of band-gap surface states, making the unreconstructed basal surface of this two-dimensional semiconductor nearly ideal from the standpoint of metal-semiconductor contacts. Lince *et al.*[10] have evaporated a number of different metals on the MoS_2 basal plane and have found a nearly linear dependence of the shift in XPS peaks with the metal work functions, indicating an unpinned Fermi level. The absence of broken bonds at the surface, and the stable covalent bonding within the planes also make this surface chemically unreactive. This means that clean surfaces for study are conveniently and easily prepared, and are not quickly contaminated by the environment.

The topography of MoS_2 has been studied previously by scanning tunneling microscopy, and atomically resolved images have been obtained.[11–13] Different experimenters have reported different conditions for obtaining atomic-resolution images. This has usually been explained in terms of the known band gap and the bulk doping type, which lead to an absence of bulk states in a certain energy range. Some current-voltage spectroscopic results have also been reported by Sarid *et al.*[13] A plot of $d\ln I/d\ln V$ *versus* V in this work shows some indication of a band gap of about 0.75 eV. This is somewhat smaller than the previously measured value of 1.2 eV for the indirect band gap.[14] The optical band gap has been measured at about 1.9 eV.[15]

In contrast, what we find in this study is a highly complex behavior. Rectified I-V curves, some with current at positive sample bias and some with current at negative bias, are seen on the same sample. Symmetric-looking I-V curves are also found. This

variety of features may be explained in part by the expected inhomogeneities in our natural samples.

Experimental

The molybdenum disulfide used for this study was of natural origin and came from two different sources. Measurements of the electrical transport properties showed some variability from sample to sample within a given batch. Of the actual samples used for spectroscopy, one exhibited *p*-type doping, and two exhibited *n*-type doping as given by the sign of the thermopower voltage. Hall probe measurements confirmed the doping type and gave dopant densities and mobilities. These data are shown in Table 1.

The ultrahigh vacuum scanning tunneling microscope used for these studies was built at Caltech using a design similar to the "pocket" STM, with a piezoceramic louse for the coarse motion control, a three-element tripod piezoelectric XYZ scanner, and a stack of stainless steel plates separated by Viton elastomer spacers for vibration isolation. The vibration immunity was enhanced by an additional two stages of spring-suspension vibration isolation, which were also internal to the vacuum system. The vacuum system itself consists of two separate ion-pumped chambers, one for the STM and the other for sample preparation. These are separated from each other and from a vacuum load lock by gate valves. Samples are introduced through the load lock and transferred into the sample preparation chamber and on into the STM chamber by means of a long-stroke translator. Transfers from the long-stroke translator to the STM and to the sample-preparation manipulators is effected using bellows-sealed wobble sticks. The instrument is described in more detail in Chapter 2.

The samples were mounted on stainless steel stubs using indium solder and introduced into the vacuum system after cleavage. Some of the samples were cleaved in N_2 flow. Also, in some cases, the samples were heated to 450 °C after introduction to the

vacuum system to drive off surface contaminants. These procedures are known to give clean surfaces as measured by photoemission.[16] Similar procedures have been used to prepare surfaces for topographical studies and have resulted in clean areas where atomic resolution imaging could be performed.[11] Also, previous studies on MoS_2 surfaces using LEED and AES have shown that even simple insertion into ultrahigh vacuum of an air-cleaved surface of this highly unreactive material yields a relatively clean surface and an ordered LEED pattern.[17]

The current-voltage spectra were digitally acquired using an 80286-based microprocessor. The microprocessor controls the sample bias voltage and digitizes the current after amplification with a commercial electrometer. Normal tip-surface spacing is maintained by an analog feedback circuit consisting of an electrometer, logarithmic amplifier, gated integrator for feedback bandwidth control, and a high-voltage amplifier for driving the Z piezoceramic. The tunneling spectra are acquired by closing the integrator gate for ~ 50 ms, thus interrupting feedback. This has the effect of freezing the position of the tip in space. During this feedback-off time the voltage is ramped and the resulting current digitized. For the spectra presented here, typically 500 such individually acquired *I-V* scans were averaged. The individual scans in all cases had the same qualitative features as the averaged scans. For all of the *I-V* curves presented here, the STM tip used was an electrochemically etched gold wire.

Results and Discussion

p-type Sample

Figure 1 shows a series of *I-V* curves at different tip-sample separations for the *p*-type doped sample 1. This sample was cleaved in a nitrogen flow and immediately inserted into the sample load lock and pumped down. Large-scale topographic scans before or after the *I-V* scans showed a flat, smooth surface. For each of the curves

presented in Fig. 1, the tunneling-current feedback set point was 100 pA. However, similarly rectified *I-V* curves were also obtained at a feedback current of 1 nA. The feedback sample bias, V_{fb}, was systematically changed from curve to curve in order to vary the gap spacing. As described above, the *I-V* curves were acquired by interrupting the feedback and then recording the current while ramping the sample bias from V_{fb} to $-V_{fb}$. As V_{fb} is decreased for a given tunneling-current feedback set point, the tip is expected to move closer to the surface because of a lower gap resistance.

The most striking feature for all the curves presented in Fig. 1 is the strong, positive-bias rectification of the current. To understand this rectification, we must consider the current conduction mechanism for a metal-insulator-semiconductor (MIS) junction. Here we follow the lead of Bell and Kaiser *et al.*[18] who have observed a similar rectification in STM experiments on an Au/Si system. Figure 2 is diagram of electron potential energy *versus* normal displacement for an ideal, planar MIS junction with a *p*-type semiconductor separated from a metal by a vacuum gap with no external bias. For most common metal-(*p*-type) semiconductor combinations, ϕ_m, the work function of the metal, is smaller than the work function of the semiconductor, ϕ_s. In particular, ϕ_m for polycrystalline gold is 5.1 eV [Ref. 19], and ϕ_s for MoS_2 has been measured at 4.8 eV for *n*-type material and 5.2 eV for *p*-type material.[20] An even wider range of ϕ_s should be possible, given the large band gap. For an ideal MIS junction in which there is negligible surface-state density, the potential difference that is due to the difference in work functions, along with any externally applied bias, is distributed between a field in the vacuum gap and a diffusion potential in the semiconductor surface space-charge region.

Current conduction between the metal and semiconductor involves thermionic emission of holes over the surface diffusion-potential barrier, V_d, followed by tunneling through the vacuum barrier. (The potential energy of holes increases with increasing

negative energy on an electron energy diagram. For tunneling through the vacuum region, the carrier can be thought of as an electron.) Positive sample bias (forward bias) decreases the magnitude of the surface diffusion potential, leading to increased current over the barrier. The thermal activation barrier for holes in reverse bias is the offset of the metal Fermi level from the surface valence-band edge, V_b. In the light doping or small separation limit, most of the field is found in the semiconductor and therefore V_b is only weakly dependent on the bias. Hence, tunneling current for increasing negative bias remains low, and the overall current-voltage characteristics show positive rectification.

As the separation between the metal and the semiconductor is increased, proportionately more of the total potential difference is found in the vacuum region. Although this results in a smaller zero-bias value of V_d, and hence a greater population of carriers available for tunneling through the vacuum region, it also results in a more slowly decreasing V_d with increasing sample bias, and a relatively weaker onset of the current. For reverse bias, on the other hand, since V_b is related to the field in the vacuum region, the trend with increasing tip-sample separation is for V_b to become a more rapidly decreasing function of the applied bias. This will result in an increasing negative bias current. So we see that as the separation increases, both a decrease in forward bias current and an increase in reverse bias current are expected (scaled by the exponentially decreasing vacuum-tunneling probability). A more complete treatment of the separation dependence of the I-V characteristics for ideal MIS junctions is found in Chapter 4 for the analogous case of an n-type semiconductor in depletion.

This thermionic emission theory of MIS structures is then able to explain qualitatively the positive rectification seen in Fig. 1. Note that the curves taken with lower V_{fb}, and hence smaller tip-sample separations, show a higher absolute value of reverse bias current than those taken with higher V_{fb}. This would at first glance appear inconsistent with the predictions of the thermionic emission theory. This is not the case,

as the phenomenon is actually due to the exponential scaling of the current with separation. Careful examination reveals that the ratio of forward-to-reverse current at given magnitude of the sample bias is a monotonically decreasing function of separation.

Other mechanisms for current rectification in STM experiments on semiconductors have also been described by other investigators. Notably, the curvature of the tip can lead to rectification because of the enhancement of the field near the tip surface. This mechanism of current rectification is analogous to field emission from a sharp tip and is sample-independent, as was shown in a comparison of *n*-type and *p*-type Si (111) 2x1 samples.[21] The reason that the band-bending mechanism discussed above was not seen in these experiments is that the semiconductor surface in question has a large surface-state density that shields the bulk from any external field. The tip-curvature effect described gives rise to enhanced current for positive sample bias (electrons flowing from tip to sample), just as in our results of Fig. 1. However, for reasonable estimates of tip curvature, the predicted rectification is not very pronounced until higher sample biases are reached.

n-type Samples

In contrast to the tip-curvature rectification, the direction of easy current flow predicted by the thermionic emission model reverses when the semiconductor doping type is reversed. The necessary condition is that the semiconductor be in depletion, which in this case means that the work function of the metal must be greater than the work function of the semiconductor. This condition is satisfied in our Au/*n*-type MoS_2 system. The *I-V* curves on our *n*-type samples are therefore expected to show rectification also, but with the stronger current flow at negative sample bias. This is indeed seen in the *I-V* curves shown in Fig. 3, which were taken on sample 2 (*n*-type, 6×10^{17} cm^{-3}). In this case the sample was cleaved under N_2 flow and baked in vacuum at 450 °C to drive off any contaminants. This series was taken by feeding back to a current of –1 nA, with V_{fb}

once again varying from curve to curve so that the characteristics at different s could be examined. The trends in the rectification are completely analogous to those seen in Fig. 1 for the *p*-type sample.

On this same sample, however, positive rectified *I-V* curves are also sometimes seen. The curves shown in Fig. 4 were again taken at a 1 nA tunnel current, this time feeding back to positive sample bias, since that is the direction of easy current flow in this case, and the aim is to keep the tip from contacting the surface. The dependence of the current on the magnitude of V_{fb} for negative sample bias is qualitatively the same as seen for reverse bias in Figs. 1 and 3. In positive sample bias, the current turn-on appears to be somewhat weaker than in the previous examples.

The other, more lightly doped *n*-type sample, sample 3, showed almost exclusively positive rectified *I-V* curves over the regions we examined. An example of a series of scans is shown in Fig. 5. These data were taken at positive V_{fb}, with a current set point of 1 nA. Lowering the feedback current to 100 pA on this sample resulted in *I-V* curves that appeared almost symmetric, but still slightly reverse-rectified, as illustrated in Fig. 6. As discussed above, increasing the separation in an ideal MIS junction is expected to increase the relative current in reverse bias. For an *n*-type sample such as sample 3, this means that increasing the separation by lowering the current feedback set point should lead to relatively more current in positive sample bias. What we find in comparing Figs. 5 and 6 is in fact the opposite trend, which would instead be consistent with the thermionic emission description for a *p*-type sample.

Inhomogeneous Doping

This leads us to postulate that these mineralogical samples are inhomogeneously doped. Both *n*-type and *p*-type regions are hypothesized to co-exist within the same sample, with grain sizes as small as 1 μm. This is not a completely unexpected result for layered, transition-metal dichalcogenide materials. Such doping inhomogeneities have

been seen previously in small-spot photocurrent measurements of photoelectrochemical cells made from the related compound WSe_2, even using carefully prepared, apparently homogeneous and smooth, synthetic material.[22] Small-spot x-ray photoelectron spectroscopy has been performed on some of the samples from one of our sample batches. As the X rays were focused on different parts of the surface, a shift in the surface Fermi level relative to the band edges of about 0.2 eV was seen.[23] The shift in surface Fermi levels is understood to be caused by shifts in the bulk doping levels because of variations in dopant density or doping type. The small variation of 0.2 eV does not not imply a great enough difference in doping levels to explain the dramatic differences we see in tunneling spectroscopy; however, these photoemission results are averages over relatively large areas of the surface (10^4 μm^2) because of the minimum achievable spot size.

The best evidence we have that regions of both doping types co-exist on our particular samples is shown in Fig. 7. This is a series of *I-V* spectra taken over a period of about two hours on sample 3. The feedback current set-point in each case was 2 nA. The first curve in the series, Fig. 7(a), shows the expected negative bias rectification for this *n*-type sample. About ten minutes later, a symmetric *I-V* behavior was observed [Fig. 7(b)]. Then after an additional 15 minutes, the *I-V* character had reverted to its original negative bias rectification [Figs. 7(c)]. Finally, an hour later, the *I-V* curves began to display very clear reverse rectification [Fig. 7(d)]. The residual thermal drift in our STM is usually less than 0.5 nm/min, implying that the position of the tip in scan (d) was probably no more than 30 nm from its position in scan (c). Note that all the scans were taken with the same tip, in the same general area of the sample, and within a time frame that wouldn't allow for a significant difference in surface contamination. The most consistent explanation, it seems to us, is that regions of opposite sample doping type coexist over submicron length scales.

Conclusions

MoS_2 is a compound rich with interesting electronic features that can be probed in a unique way with the STM. The current-voltage spectroscopy of MoS_2 shows a highly varied and complex behavior. In some cases the *I-V* spectra are rectified in a way that is consistent with the expectations based on thermionic emission in non-degenerate MIS structures. In other cases, the rectification is the reverse of what this model predicts. Although reversal of rectification is expected for large tip-sample separations in the thermionic emission model, the hypothesis that seems to be the most consistent with the separation dependence which we observe and with the variations in the *I-V* characteristics from location to location on the surface, is that our mineralogical samples are inhomogeneously doped, with domains of opposite doping sign as small as 1 μm. Perhaps more interesting than the doping inhomogeneities on our particular samples is the demonstrated potential for using the STM as a more general probe of semiconductor doping on a submicron scale.

References

1. W. J. Kaiser, R. C. Jaklevic, *IBM J. Res. Develop.* **30**(4), 411–6 (1986); *idem*, *Surf. Sci.* **181**, 55–68 (1987).
2. R. S. Becker, J. A. Golovchenko, D. R. Hamann, B. S. Swartzentruber, *Phys. Rev. Lett.* **55**(19), 2032–4 (1985).
3. R. J. Hamers, R. M. Tromp, J. E. Demuth, *Phys. Rev. Lett.* **56**(18), 1972–5 (1986).
4. J. A. Stroscio, R. M. Feenstra, A. P. Fein, *Phys. Rev. Lett.* **57**(20), 2579–82 (1986); R. M. Feenstra, J. A. Stroscio, A. P. Fein, *Surf. Sci.* **181**, 295–306 (1987).
5. R. M. Feenstra, Joseph A. Stroscio, *J. Vac. Sci. Technol.* **B 5**(4), 923–9 (1987).
6. B. Reihl, J. K. Gimzewski, J. M. Nicholls, E. Tosatti, *Phys. Rev.* **B 33**(8), 5770–3 (1986); H. Fuchs, E. Tosatti, *Europhys. Lett.* **3**(6), 745–9 (1987).
7. J. A. Stroscio, R. M. Feenstra, A. P. Fein, *Phys. Rev. Lett.* **59**(16), 1668–71 (1987).
8. R. M. Feenstra, J. A. Stroscio, J. Tersoff, A. P. Fein, *Phys. Rev. Lett.* **58**(12), 1192–5 (1987).
9. R. T. Shuey, *Semiconducting Ore Minerals*, Elsevier, Amsterdam (1975), *pp.* 276–89.
10. J. R. Lince, D. J. Carré, P. D. Fleischauer, *Phys. Rev.* **B 36**(3), 1647–56 (1987).
11. M. Weimer, J. Kramar, C. Bai, J. D. Baldeschwieler, *Phys. Rev.* **B 37**(8), 4292–5 (1988); M. Wiemer, J. Kramar, C. Bai, J. D. Baldeschwieler, W. J. Kaiser, *J. Vac. Sci. Technol.* **A 6**(2), 336–7 (1988).
12. G. W. Stupian, M. S. Leung, *Appl. Phys. Lett.* **51**(19), 1560–2 (1987).
13. D. Sarid, T. D. Henson, N. R. Armstrong, L. S. Bell, *Appl. Phys. Lett.* **52**(26), 2252–4 (1988).
14. K. K. Kam, B. A. Parkinson, *J. Phys. Chem.* **86**, 463–7 (1982).

15. B. L. Evans, in *Optical and Electrical Properties*, Vol. 4 of *Physics and Chemistry of Materials with Layered Structures*, ed. P. A. Lee, Riedel, Dordrecht (1976) *pp.* 1–144; R. Coehoorn, C. Haas, R. A. de Groot, *Phys. Rev.* **B 35**(12), 6203–6 (1987).

16. J. C. McMenamin, W. E. Spicer, *Phys. Rev.* **B 16**(12), 5474–87 (1977).

17. R. H. Williams, A. J. McEvoy, *J. Phys.* **D 4**, 456–64 (1971); M. Salmeron, G. A. Somorjai, A. Wold, R. Chianelli, K. S. Liang, *Chem. Phys. Lett.* **90**(2), 105–7 (1982).

18. L. D. Bell, W. J. Kaiser, M. H. Hecht, F. J. Grunthaner, *Appl. Phys. Lett.* **52**(4), 278–80 (1988); W. J. Kaiser, L. D. Bell, M. H. Hecht, F. J. Grunthaner, *J. Vac. Sci. Technol.* **A 6**(2), 519–23 (1988).

19. H. B. Michaelson, *J. Appl. Phys.* **48**, 4729 (1977).

20. I. T. McGovern, R. H. Williams, C. H. B. Mee, *Surf. Sci.* **46**, 427–40 (1974).

21. R. M. Feenstra, J. A. Stroscio, A. P. Fein, *Surf. Sci.* **181**, 295–306 (1987).

22. S. Menezes, L. F. Schneemeyer, H. J. Lewerenz, *Appl. Phys. Lett.* **38**(11), 949–51 (1981).

23. Data provided by J. R. Lince, The Aerospace Corp., El Segundo, CA.

TABLE 1

Carrier type, doping density, resistivity, and mobility as determined by Hall coefficient measurements for the MoS_2 samples used in these experiments.

Sample	carrier type	carrier density N_d (cm^{-3})	resistivity ρ (Ω-cm)	mobility μ ($cm^2V^{-1}s^{-1}$)
1	*p*	2×10^{16}	21.2	15
2	*n*	6×10^{17}	0.473	24
3	*n*	8×10^{16}	2.91	28

Figure 1

Current-voltage spectra for sample 1 (*p*-type) showing positive bias rectification for a range of separations defined by the feedback conditions. The *I-V* curves were acquired by interrupting the feedback control system for a few milliseconds. During the feedback-off time, the sample bias was slewed, and the resulting current was digitized. The tunneling-current, feedback set point was 100 pA for each curve and the feedback sample bias voltages were 0.1, 0.2, 0.35, 0.5, 0.8, and 1.0 V for scans **(a)** – **(f)**, respectively. A range of sample spacings was examined by changing the feedback voltage applied to the sample.

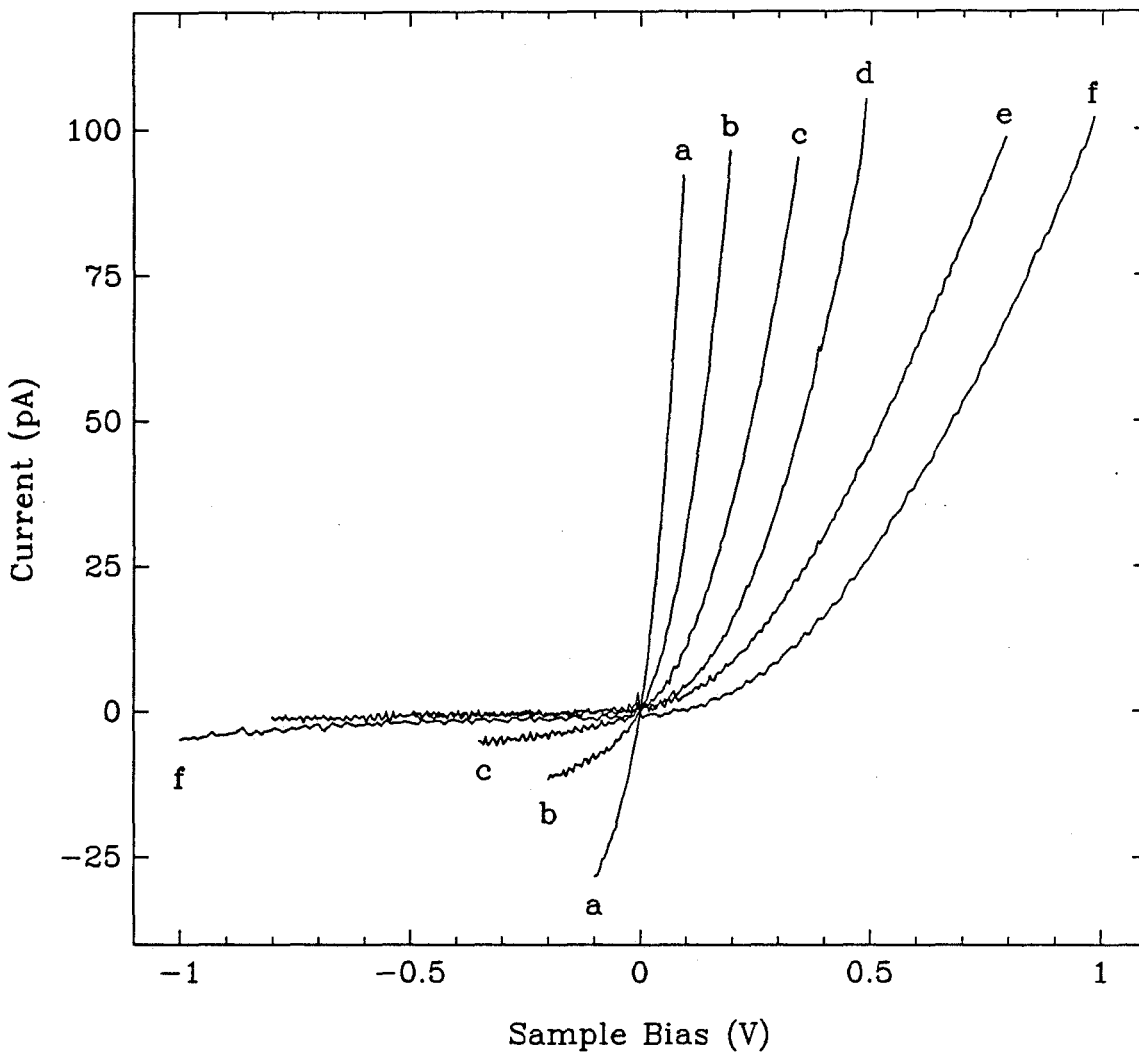
100
75
50
25
0
−25
Current (pA)
−1
−0.5
0
0.5
1
Sample Bias (V)
a
b
c
d
e
f
f
c
b
a

Figure 2

Electron potential energy diagram for an ideal, planar, *p*-type semiconductor MIS structure. The work function of the metal, ϕ_m, is smaller than the work function of the semiconductor, ϕ_s, leading to a depletion of the majority carriers (holes) in the semiconductor and a surface diffusion-potential of magnitude V_d.

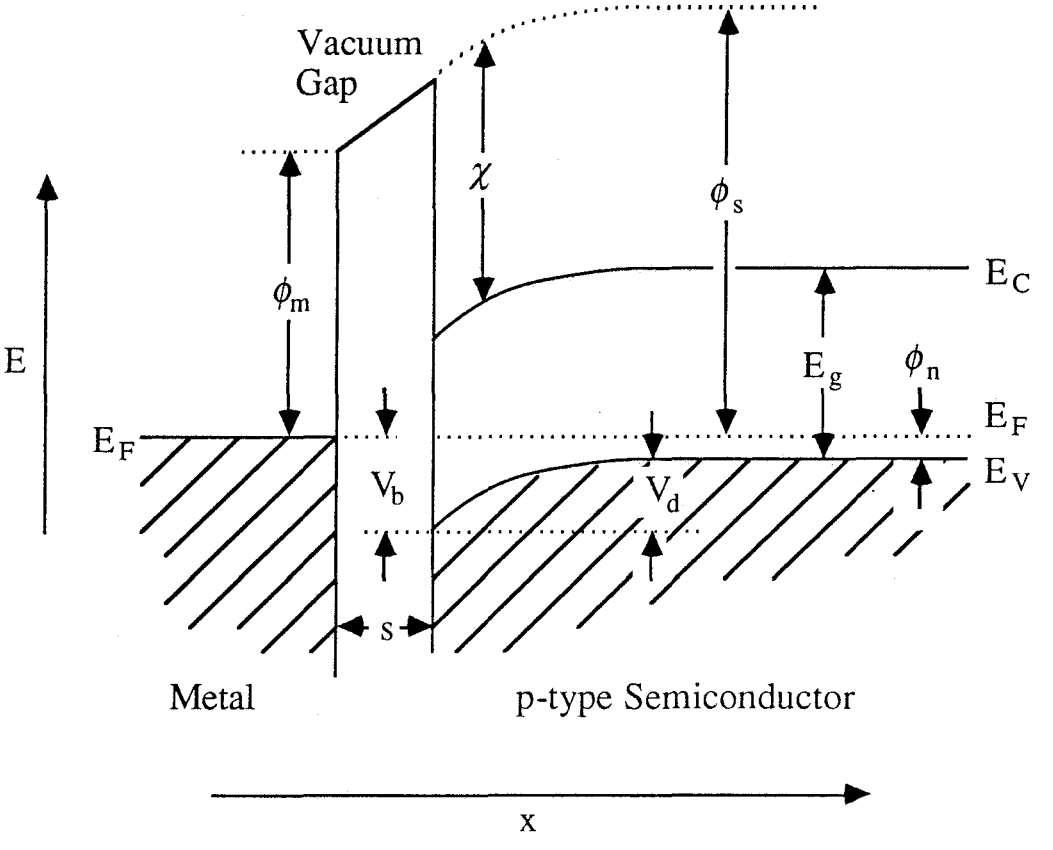
Vacuum
Gap
χ
ϕ_s
ϕ_m
E_C
E
E_g
ϕ_n
E_F
E_F
E_V
V_b
V_d
s
Metal
p-type Semiconductor
x

Figure 3

Current-voltage curves for a range of tip-sample separations over an *n*-type semiconductor surface (sample 2) showing negative sample bias rectification. The curves are acquired in the same way as the curves in Fig. 1, in this case feeding back to −1 nA using sample bias voltages of −0.3, −0.5, −0.75, and −1.0 V for curves **(a)** through **(d)**, respectively.

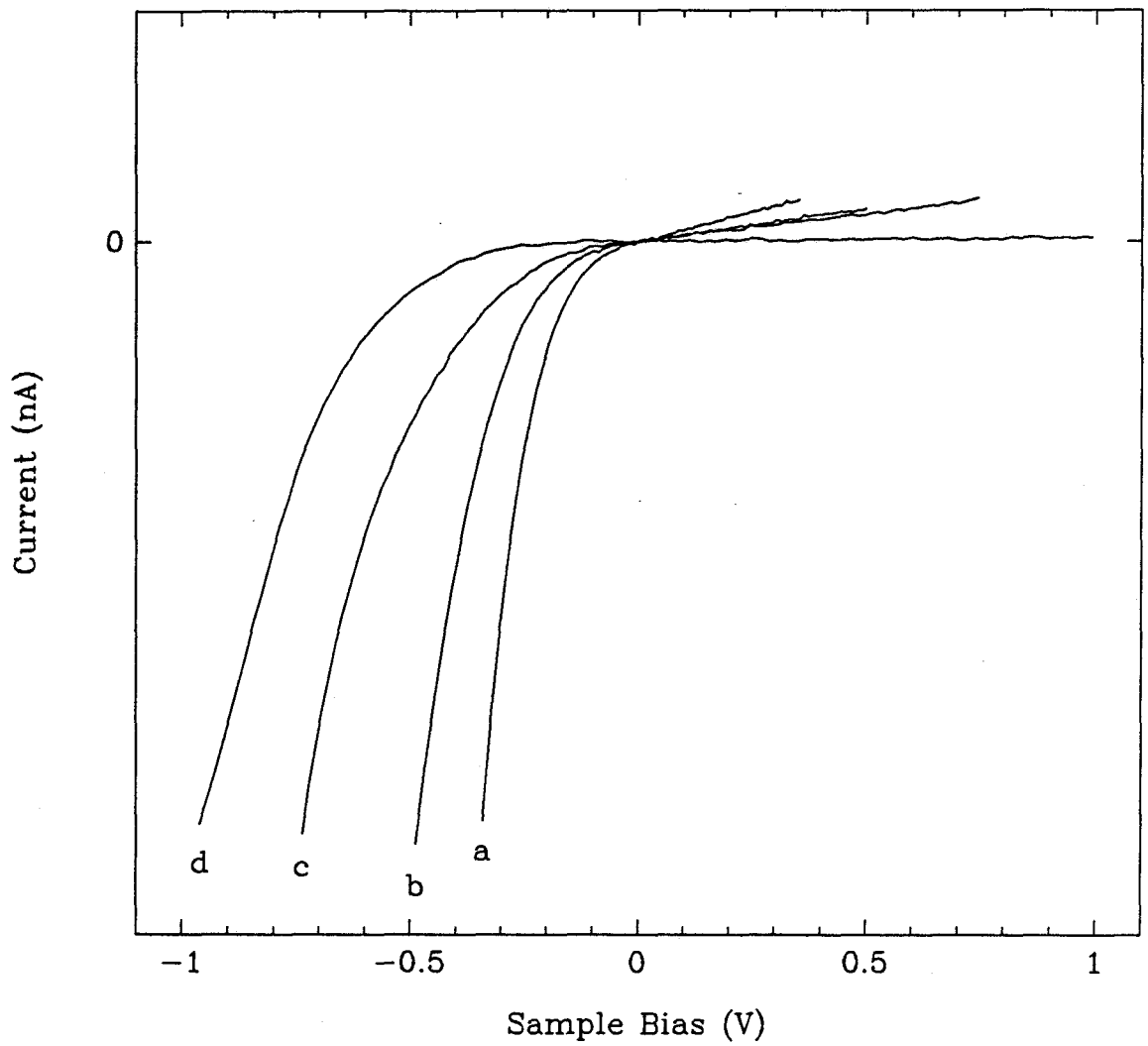
0
Current (nA)
d
c
b
a
−1
−0.5
0
0.5
1
Sample Bias (V)

Figure 4

Positive-rectified current-voltage curves on the same sample used in Fig. 3 (n-type, 6×10^{17} cm^{-3}). The tunneling-current, feedback set point for these curves is 1 nA, and the feedback sample bias voltage is 0.2, 0.4, 0.6, 0.8, and 1.0 V for curves **(a)** through **(e)**, respectively.

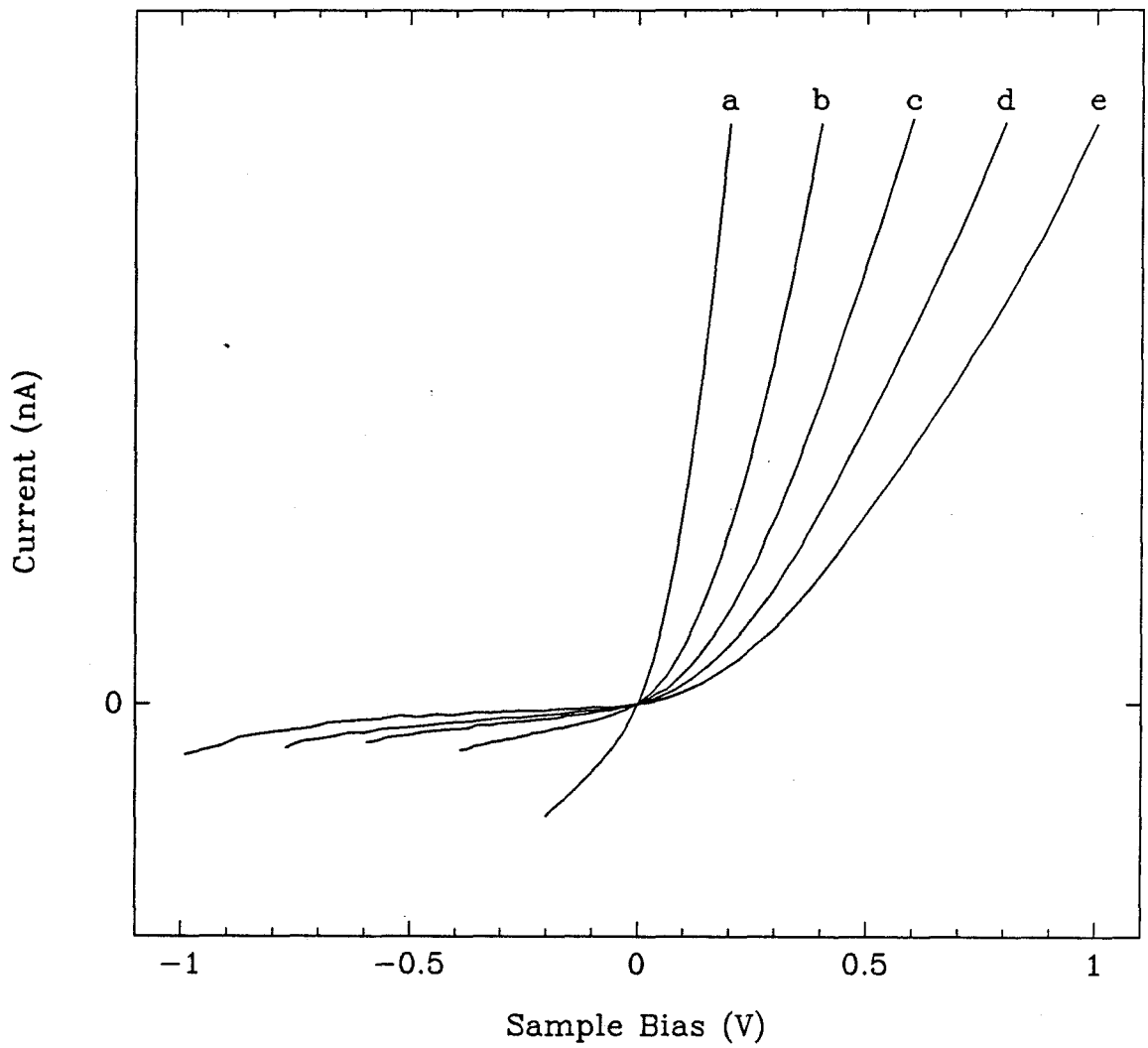
a
b
c
d
e
Current (nA)
0
−1
−0.5
0
0.5
1
Sample Bias (V)

Figure 5

Current-voltage curves obtained for sample 3 (*n*-type, 8×10^{16} cm^{-3}), showing positive sample bias rectification. Feedback conditions of 1 nA with sample bias voltages of 0.1, 0.2, 0.3, 0.4, and 0.5 V were used for curves (a) through (e), respectively.

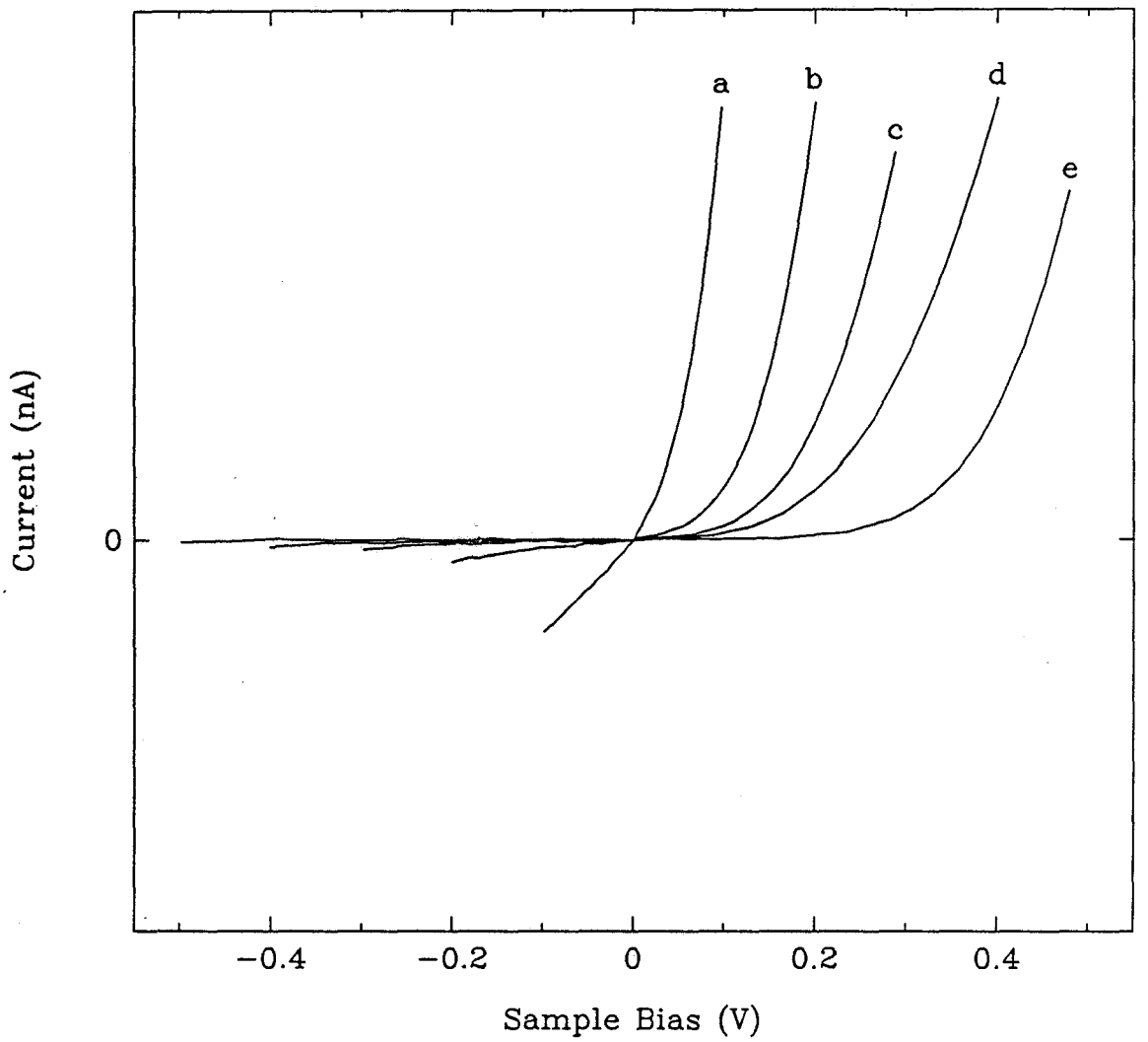
a
b
c
d
e
Current (nA)
0
−0.4
−0.2
0
0.2
0.4
Sample Bias (V)

Figure 6

Current-voltage curves for the same sample and feedback bias voltages as Fig. 6. The tunneling-current, feedback set point in this case is reduced to 100 pA. Qualitatively less rectified *I-V* characteristics are observed.

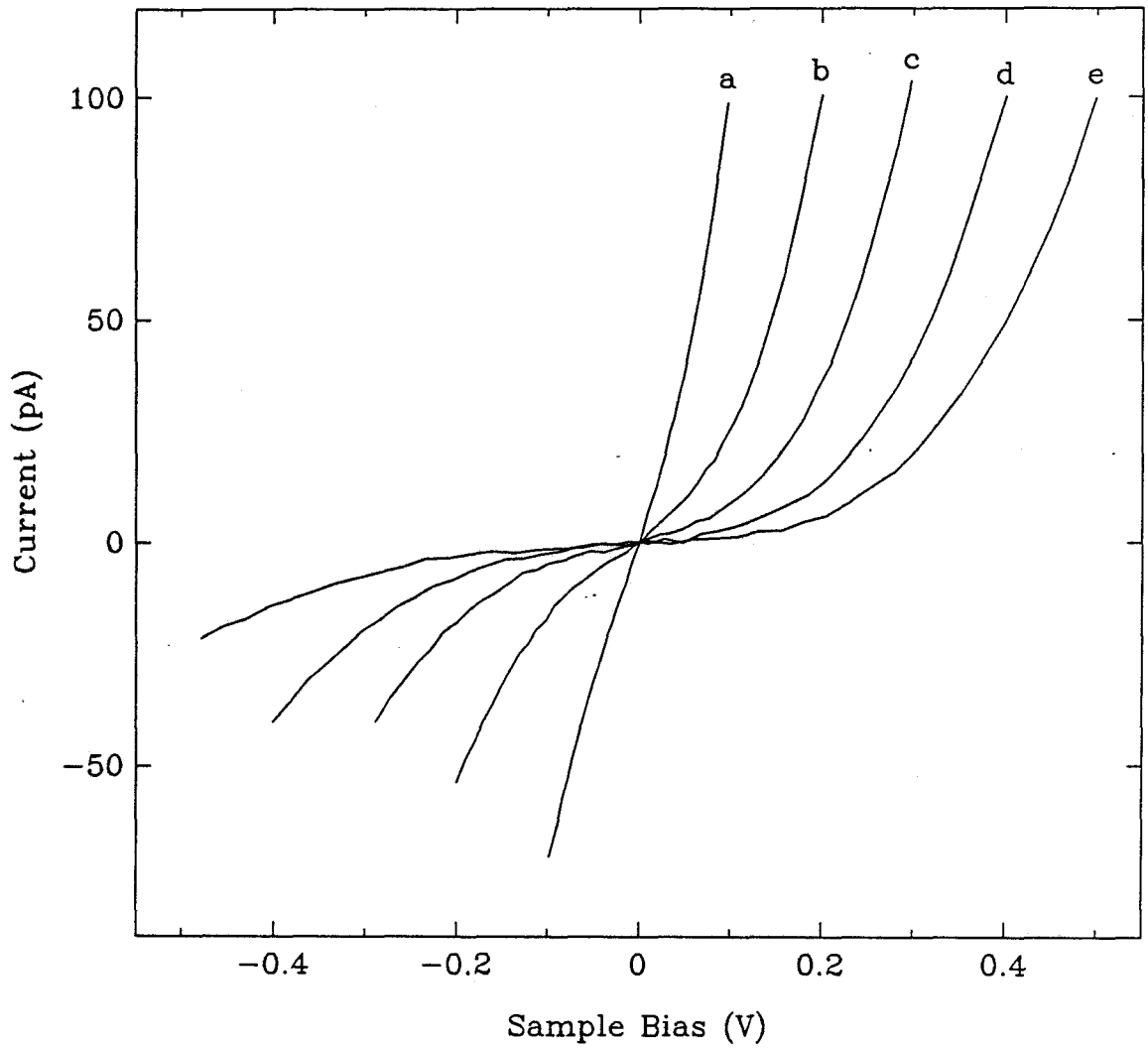
a
b
c
d
e
100
50
0
−50
Current (pA)
−0.4
−0.2
0
0.2
0.4
Sample Bias (V)

Figure 7

A series of current-voltage curves taken on sample 3 within a period of less than two hours. The curves were acquired in the usual way with a tunneling-current, feedback set point of 2 nA (absolute value) throughout. For the *I-V* presented in **(a)**, a feedback sample bias, V_{fb}, of 0.5 V was used. This is opposite the direction of easy current flow, so the magnitude of the negative bias current is large. Curve **(b)** was acquired about 15 minutes later using $V_{fb} = -0.5$ V. The character of the curve has changed from negative bias rectification to symmetric. In curve **(c)**, taken fifteen minutes later using the identical parameters to (b), the *I-V* has reverted to negative bias rectification. Finally, in curve **(d)**, taken an hour after (c), the *I-V* curve has begun to show strong, positive-bias rectification, so a V_{fb} of 0.5 V was again used.

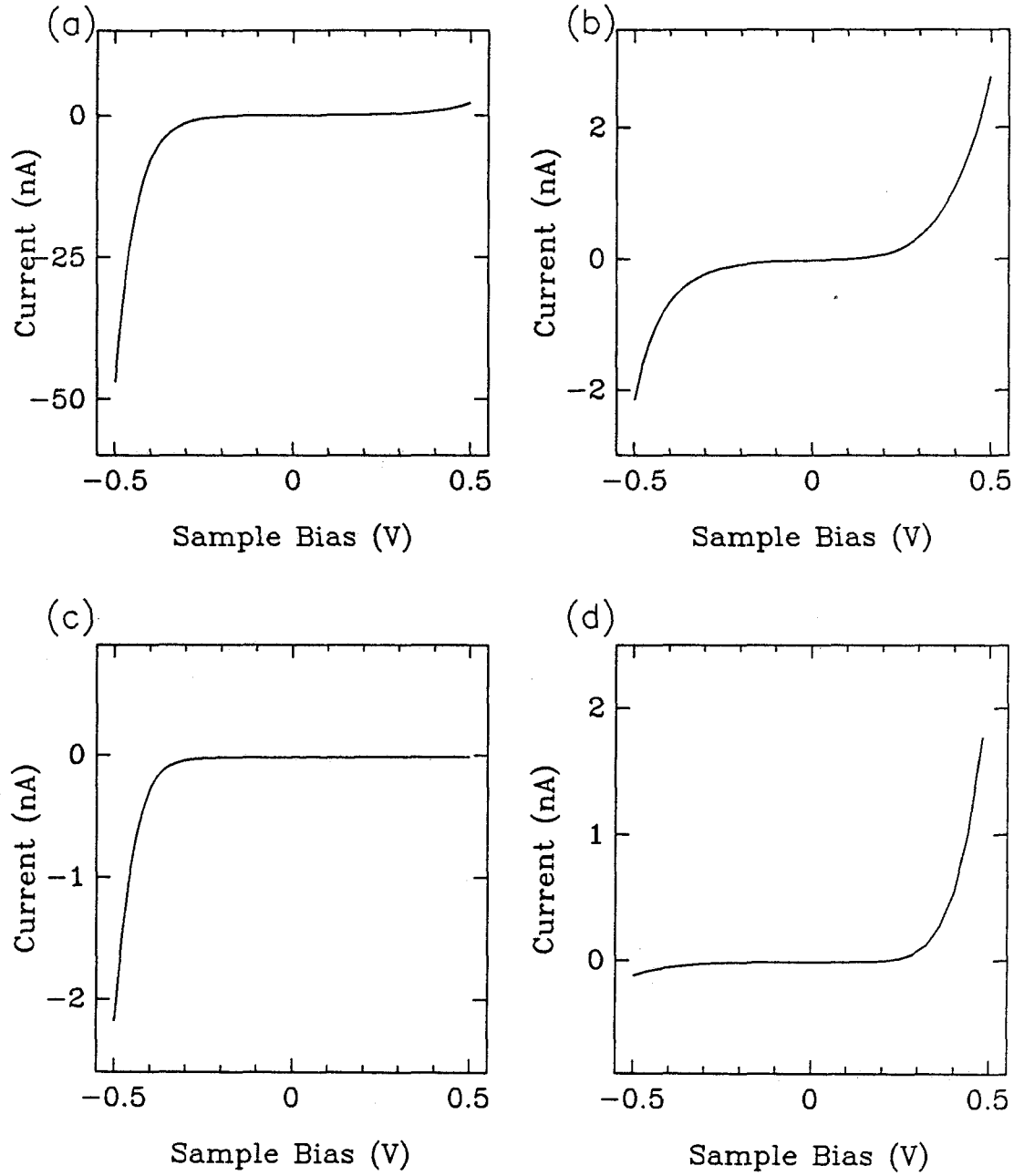
(a)
0
−25
−50
Current (nA)
−0.5
0
0.5
Sample Bias (V)
(b)
2
0
−2
Current (nA)
−0.5
0
0.5
Sample Bias (V)
(c)
0
−1
−2
Current (nA)
−0.5
0
0.5
Sample Bias (V)
(d)
2
1
0
Current (nA)
−0.5
0
0.5
Sample Bias (V)